Stall and Spin Recovery Using Optimal Trajectory Planning

by

MLD Babl

Thesis presented in partial fulfilment of the requirements for the degree of Master of Science in Electronic Engineering in the Faculty of Electronic and Electrical Engineering at Stellenbosch University.

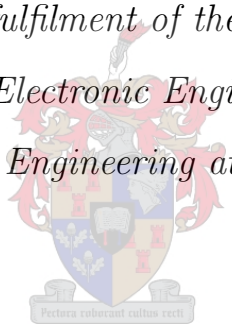

Department of Electrical & Electronic Engineering,
University of Stellenbosch,
Private Bag X1, 7602 Matieland, South Africa

Supervisor: Dr JAA Engelbrecht

March 2021

Declaration

UNIVERSITEIT•STELLENBOSCH•UNIVERSITY
jou kennisvennoot • your knowledge partner

1. Plagiaat is die oorneem en gebruik van die idees, materiaal en ander intellektuele eiendom van ander persone asof dit jou eie werk is.
   Plagiarism is the use of ideas, material and other intellectual property of another's work and to present is as my own.

2. Ek erken dat die pleeg van plagiaat 'n strafbare oortreding is aangesien dit 'n vorm van diefstal is.
   I agree that plagiarism is a punishable offence because it constitutes theft.

3. Ek verstaan ook dat direkte vertalings plagiaat is.
   I also understand that direct translations are plagiarism.

4. Dienooreenkomstig is alle aanhalings en bydraes vanuit enige bron (ingesluit die internet) volledig verwys (erken). Ek erken dat die woordelikse aanhaal van teks sonder aanhalingstekens (selfs al word die bron volledig erken) plagiaat is.
   Accordingly all quotations and contributions from any source whatsoever (including the internet) have been cited fully. I understand that the reproduction of text without quotation marks (even when the source is cited) is plagiarism.

5. Ek verklaar dat die werk in hierdie skryfstuk vervat my eie oorspronklike werk is en dat ek dit nie vantevore in die geheel of gedeeltelik ingehandig het vir bepunting in hierdie module/werkstuk of 'n ander module/werkstuk nie.
   I declare that the work contained in this assignment is my original work and that I have not previously (in its entirety or in part) submitted it for grading in this module/assignment or another module/assignment.

MLD Babl Initials and Surname		***March 2021*** Date

Abstract

Aircraft pilots and autopilots would greatly benefit from a system that assists in recovering an aircraft after a severe flight upset such as a spin or stall. This system needs to perform the aerodynamic recovery that recovers the aircraft to its normal flight envelope. Once the aerodynamic recovery is completed the pilot or existing flight control system should perform the attitude, flight path angle, and airspeed recovery. Therefore, a stall and spin recovery system for aircraft using optimal trajectory planning is designed, implemented, and verified. A deep stall is a condition where an aircraft is trapped in a nose-high stall condition. While in a deep stall the aircraft's elevator control surface cannot produce enough nose-down pitching moment to recover the aircraft from the stall. Spin is a condition where an aircraft naturally starts to rotate about the vertical axis after having stalled and follows a downward tight spiral trajectory.

The NASA Generic Transport Model (GTM) is used as the basis for the design and verification of the system. The aerodynamic model of the NASA GTM simulation model is modified to exhibit deep stall and spin behaviour. Simulations are performed to show that the modified aircraft model can be pushed into deep stall and spin, and cannot be recovered using elevator actions only. The deep stall and spin recovery task is formulated as an optimal control problem and solved using an A* and an RRT search algorithms. These algorithms find the optimal sequence of control actions and the resulting optimal state trajectory to escape from the deep stall or spin.

The deep stall and spin recoveries are verified in simulation using the NASA GTM aircraft model. Simulation results show that the recovery sequences generated by the algorithms successfully perform the aerodynamic recovery. The deep stall recovery sequence first commands the rudder to yaw the horizontal tailplane out of the aircraft's own wake to regain elevator effectiveness, and then commands the elevator to pitch the nose of the aircraft down and recover from the stall. The spin recovery sequence first commands the rudder to reduce the rolling and yawing angular rates and then commands the elevator to pitch the nose of the aircraft down.

A trajectory regulator, in the form of a linear quadratic regulator(LQR), and a control switch are implemented. The trajectory regulator provides robustness against external disturbances and model uncertainty. The control switch determines when the aircraft enters a stall or spin condition and also when the aerodynamic envelope is recovered. The control switch transfers the control authority of the aircraft from the deep stall or spin recovery system to the existing flight control or the pilot once the recovery is complete.

General deep stall and spin recovery strategies were identified from the calculated recovery sequences. During a deep stall or spin recovery, it is possible to command the appropriate general recovery sequence and thereby nullify the calculation time required to plan the recovery sequence. When commanding the general recovery sequence the trajectory regulator regulates the state trajectories of the aircraft to track the planned general recovery state trajectories. The developed recovery system is successful in performing the aerodynamic recovery for the NASA GTM from both deep stall and spin conditions.

Samevatting

Hierdie tesis beskryf die ontwerp van 'n outomatiese deep stall en spin herstel stelsel vir groot transport vliegtuie wat van optimale baanbeplanning gerbuik maak. Deep stall is 'n toestand waar 'n vliegtuig vasgevang is in 'n neus-hoë stall toestand en die elevator beheeroppervlak kan nie genoeg neus-neer-trap-oomblik skep om die vliegtuig uit die stall te herstel nie. Spin is 'n toestand waar 'n vliegtuig natuurlik begin draai om 'n vertikale as en daan afwaarts in 'n stywe spiraalbaan val. Die NASA Generic Transport Model (GTM) word gebruik as basis vir die ontwerp en verifikasie van die stelsel.

Die aërodinamiese model van die NASA GTM-simulasiemodel word aangepas om deep stall en spin gedrag te toon. Simulasies word uitgevoer om aantetoon dat die gemodifiseerde vliegtuigmodel kan deep stall en spin modelleer. In simulasie word dit getoon dat dit nie moontlik is om van deep stall en spin te herstel met die gebruik van net die elevator beheeroppervalk nie.

Die taak vir die herstel van die deep stall en spin word geformuleer as 'n optimale beheerprobleem en opgelos met behulp van 'n A^* soek algoritme om die optimale volgorde van beheeraksies en die gevolglike optimale toestandstrajek te vind om uit die deep stall of spin te ontsnap. Die A^* -algoritme voer die beplanning uit met hulp van 'n vereenvoudigde drie-grade-van-vryheid (3DOF) vliegtuigmodel wat slegs die vinnige rotasie-dinamika van 'n deep stall modelleer. Die A^* -algoritme en die RRT algoritme voer die beplanning vir spin herstel uit met hulp van 'n Volledige vliegtuigmodel van ses grade-van-vryheid (6DOF) wat die vinnige rotasie- en transnasionale dinamika van spin modelleer.

Die outomatiese herstel van die deep stall en spin word dan in simulasie geverifieer met hulp van die volledige ses-grade-van-vryheid (6DOF) NASA GTM-vliegtuigmodel. Die simulasie-uitslae toon dat die stelsel die vliegtuig suksesvol van deep stall en spin kan herstel. Vir deep stall gebruik die optimale opeenvolging van beheeraksies eers die rudder beheeroppervlak om die horisontale stert vlakte uit die waak van die vliegtuig se hoofvlerke te skuif en dus hestel dit die effektiewetiet van die elevator beheeroppervalk. Die elevator beheeroppervlak word dan gebruik om die neus afwaarts te beweeg en dus van die stall te herstel.

Om die robuustheid van hierdie deep stall en spin herstelsreekse te verbeter, word 'n optimale baanreguleerder ontwikkel om die herstel volgorde aantepas in die teenwoordigheid van versteurings. Die baanreguleerder gebruik lineêre kwadratiese beheer gekoppel met 'n skakel funksie wat bepaal wanneer die beheer van die vliegtuig terug na die normale vlugbeheer geplaas moet word. Vir demonstrasie is die normale vlugbeheer 'n proporsionele hoeksnelheids demper.

Met die ontleding van die deep stall en spin herstel beheerreekse wat deur die algoritme vir baanbeplanning gegenereer is, is algemene herstelstrategieë van deep stall, links, en regs spin geïdentifiseer. Die algemene herstelstrategieë, gekombineer met die optimale baanreguleerder, sorg vir 'n betroubare deep stall en spin herstelstelsel.

Dedication

This work is dedicated in loving memory to my grandfather, Dietrich Maurer, who always amazed me with the stories of his life and his career as an engineer.

Acknowledgements

I would like to thank the following people and organizations for their continual support and contributions towards this thesis:

- My supervisor, Dr Japie Engelbrecht, for listening to all my ideas and strategically guiding me to the best outcome and for reading through my thesis and giving thorough feedback.
- My loving fiancée, Miss Sarah Jane Armstrong, for listening to me when things did not work and celebrating with me when they did. Thank you for also reminding me that there is more to life than just the thesis work and to have a healthy and balanced lifestyle.
- My parents, Anka and Stefan Babl, for their being the amazing Mami and Vati that they are and always encouraging me, and supporting me in all the challenges in life.
- My postgraduate comrades, Johan Ublink, Ruan Viljoen, Henry Kotzee, Francois Slabber, Daniel Jansen, Reg Grobler, and Armand Scholtz for being such fun, getting scones, exploring new methods and just being there to talk to during the good and not so good times.
- Dr Willem Jordaan for asking the difficult questions and being actively involved in the Electronic Systems Laboratory and making it such a fun place to be at.
- My friends, Jude de Villiers, Laubscher van Der Merve, Wilko Mohr and Omri Jacobzs, for being true friends and good fun.
- Dr Corné van Daalen, for his extensive knowledge regarding trajectory planning and for the good conversations we have had during Control Systems 344.
- The NASA Langley Research Center for developing the General Transport Model simulation and making it available for research.
- My sponsor, ARMSCOR for providing the funding for my postgraduate research.
- God for his steadfast love, strength and support.

Publications

Chapter 3 and 4 of the work included in this thesis was presented at the International Federation of Automatic Control (IFAC) World Congress 2020 hosted in Berlin under the title "Automatic Deep Stall Recovery using Optimal Trajectory Planning" and was co-authored by MLD Babl and JAA Engelbrecht. Subsequently this work is published in the journal *Proceedings of the 21st IFAC World Congress*.

Contents

Nomenclature

Abbreviations and Acronyms

AoA	Angle of Attack
6DOF	Six Degrees of freedom
EOM	Equations of motion
GTM	Generic Transport Model
NASA	National Aeronautics and Space Administration
LQR	Linear quadratic regulator
RRT	Rapidly-expanding random tree
ADMIRE	The Aero-Data Model In a Research Environment
HARV	High-Alpha Research Vehicle
SUPRA	Simulation of Upset Recovery in Avaition
HHIRM	Hypothetical High Incidence Research Model

Constants

g	Gravitational Acceleration	$9.81 m^2/s$

Symbols

α	Angle of attack
β	Sideslip angle
$\bar{v}$	Air speed magnitude
$\boldsymbol{x}$	System state vector
$\dot{\boldsymbol{x}}$	Derivative of system state vector
$\boldsymbol{u}$	Control input vector
$\frac{\delta f}{\delta x}$	Partial derivative of function, f, with respect to x
S	Wing surface area
$\bar{c}$	Mean aerodynamic chord
b	Wing span

m	Aircraft mass
$\boldsymbol{I_B}$	Moment of inertia matrix of the aircraft body
ρ	Air density
$\bar{q}$	Dynamic pressure
T	Thrust
t_0	Initial Time
t_f	Final Time
t_n	Time at time step n
n	Time step interval
$\boldsymbol{F_B}$	Force vector in the body axis
$\boldsymbol{M_B}$	Moment vector in the body axis
$\boldsymbol{e}$	Euler angles vector
$\delta_A, \delta_E, \delta_R$	Aileron, rudder and elevator control surface deflections. A positive deflection is defined by it producing a negative moment.
X, Y, Z	Coordinates of the force vector in the body-axis (axial, lateral, and normal force)
P, Q, R	Coordinates of the angular velocity vector in the body-axis (roll, pitch, and yaw rates)
U, V, W	Coordinates of the linear velocity vector in the body-axis (axial, lateral, and normal velocity)
L, M, N	Coordinates of the moment vector in the body-axis (roll, pitch, and yaw moment)
N, E, D	Coordinates of position vector in inertial-axes (north, east and down position)
V_N, V_E, V_D	North, east and down velocity components in inertial-axis
Φ, Θ, Ψ	Euler 3-2-1 attitude parameters of the body-axis system with respect to inertial-axis system (roll, pitch, and yaw angle)
I_{xx}, I_{yy}, I_{zz}	Principle moment of inertia of aircraft's body x-axis, y-axis and z-axis
C_X, C_Y, C_Z	Aerodynamic force coefficients of the aircraft's body x-axis, y-axis and z-axis
C_l, C_m, C_n	Aerodynamic moment coefficients of the aircraft's body x-axis, y-axis and z-axis (pitching, rolling and yawing moment)

List of Tables

List of Figures

Chapter 1

Introduction

Despite the fact that flight envelope protection functions are implemented on modern commercial aircraft, situations still arise where the aircraft exits the flight envelope due to environmental factors, pilot error, or component failures. Envelope protection functions are only designed to prevent the aircraft from exiting the flight envelope, and not to recover the aircraft to its flight envelope after a departure. Currently the envelope recovery procedure must be performed manually by the pilot. A need therefore exists for flight envelope recovery functions that assist the pilot or autopilot in recovering the aircraft to its normal flight envelope after a severe upset[9].

1.1 Background

This thesis focuses on the problem of recovering the aerodynamic envelope of an aircraft that is in deep stall and spin flight upset condition. A deep stall is a condition where an aircraft is trapped in a nose-high stall condition. While the aircraft is in a deep stall the elevator control surface cannot produce enough nose-down pitching moment to recover the aircraft from the stall [4]. A deep stall is most often exhibited by aircraft that have a high horizontal tailplane, such as T-tail transport aircraft and jet fighter aircraft with high horizontal tails. At very high angles of attack the horizontal tailplane is immersed in the combined wake of the stalled wings, engines and fuselage. This causes a nonlinear variation of pitching moment as a function of angle of attack (AoA) and resulting in two ranges of stable trim points. The normal trim point is at a low AoA ($\alpha = +-5$) whereas a deep stall trim point is at a high AoA ($\alpha = +20$). In deep stall, the effectiveness of the elevator is also significantly decreased due to the low-energy wake impinging on the horizontal tailplane. This results in the elevator control surface to generate insufficient nose-down pitching moment to recover the aircraft from the deep stall trim point.

A spin is a condition where an aircraft rotates about a vertical axis. In a spin the inner-wing of the aircraft stalled but the outer-wing still generates some degree of lift. This causes an aggravated rolling, yawing and pitching motion towards the stalled wing which forces the aircraft into a downward spiral path. While an aircraft is in a spin, it is very disorientating for a pilot. Special spin recovery training is required to increase the chance of manual recovery[10].

The appropriate deep stall and spin recovery procedure is dependent on the specific aircraft configuration [20]. One possible strategy to escape from deep stall is to yaw the horizontal tailplane out of the wake using the rudder and thereby regain elevator effectiveness. This is followed by using the elevator to recover from the stall. Another

possible strategy, called the "pitch rocking" method, is to pitch the aircraft up and down at a specific resonant frequency. This is done to build up the amplitude of the pitch angle oscillations until the AoA escapes the deep stall.

Spin recovery focuses on reducing both the AoA and high angular rates. Manual spin recovery procedures recommend the following order of control inputs: Reduce power to idle, position ailerons to neutral, apply full opposite rudder against rotation, apply positive, brisk and straight forward elevator, neutralise the rudder after spin rotation stops and finally apply back elevator pressure to return to level flight[1].

1.2 Research Goal

The purpose of this research project is to design, implement, and verify a stall and spin recovery system for an aircraft. The recovery system should use optimal trajectory planning and feedback control to perform the aerodynamic envelope recovery. A trajectory planning algorithm must be used to determine the optimal control sequence and the resulting optimal state trajectory to escape from the spin and recover from the deep stall. The performance of the recovery must be verified in simulation using the modified NASA GTM passenger aircraft model or the ADMIRE fighter aircraft model.

1.3 Proposed Solution

The following solution addressed the problem of recovering the aerodynamic envelope of an aircraft that is either in a deep stall or a spin flight upset condition; a deep stall and spin recovery system. This recovery system should find the correct recovery sequence for the specific aircraft using models of the flight dynamics of that aircraft. The recovery cannot be performed by only linear feedback controllers because the aircraft dynamics are highly nonlinear while the aircraft is in deep stall or spin. The deep stall and spin recovery tasks were formulated as constrained optimal path planning problems. These tasks were solved by using either an A^* or an rapidly-exploring randomly tree (RRT) search algorithm. These algorithms should find the optimal sequence of control actions and the resulting optimal state trajectory to recover the aircraft from the deep stall or spin. To ensure that the recovery procedure is robust against external disturbances and model uncertainty a trajectory regulator and control switch were implemented. The deep stall and spin recovery systems were verified in simulation using the NASA GTM simulation as a testing aircraft.

1.4 System Overview

This section provides an overview of the stall and spin recovery system and how it would be integrate into the existing flight control system of an aircraft. A complete flight envelope recovery is performed in two stages: an aerodynamic envelope recovery and an attitude, flight path angle, and airspeed recovery. The aerodynamic envelope is recovered by returning the AoA, sideslip angle, and angular rates of the aircraft to their normal operating ranges.

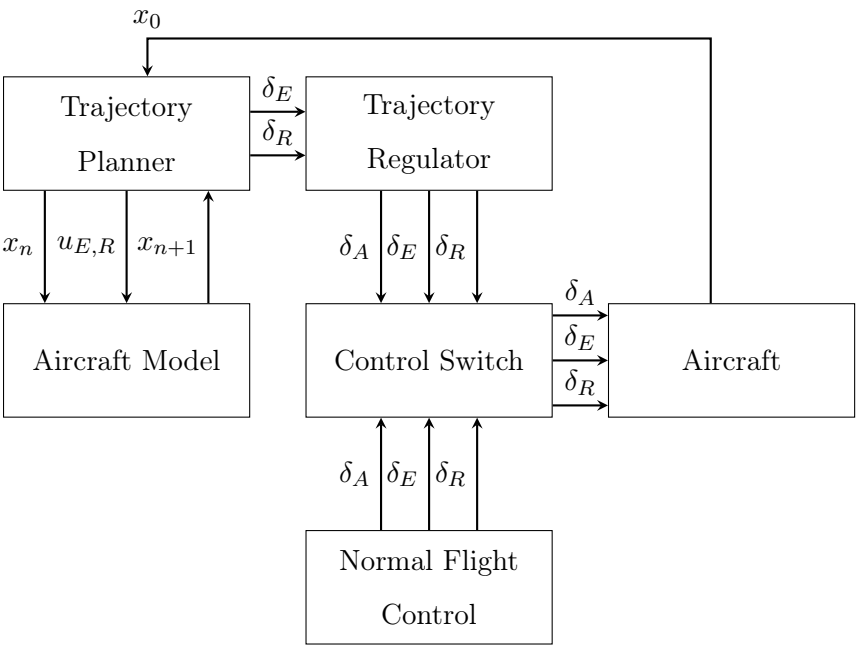

Figure 1.1: The basic structure of the recovery system.

The architecture of the stall and spin recovery system, as well as its interface to the existing flight control system, is shown in Figure 1.1. The deep stall or spin recovery control system consists of a trajectory planner, the aircraft model used for planning, and trajectory regulator. If the aircraft is flying normally then the control actions of the existing flight control is passed through the control switch to the aircraft's control surfaces. Once a deep stall or spin condition is detected, the recovery system will be activated. The control switch will then pass the control actions from the recovery system to the aircraft's control surfaces, instead of the control actions from the normal flight control system. The recovery system will identify whether it is a deep stall condition or a spin condition, and will activate the appropriate recovery procedure for the flight upset condition. Two recovery system design approaches are proposed. The first approach requires the recovery system to calculate the recovery sequence for each individual deep stall or spin flight upset. The second approach allows the recovery system to use general deep stall and spin recovery strategies which were identified from observing the results of the first approach.

In the first approach, an online trajectory planner captures the current state of the aircraft which is obtained from the aircraft's onboard sensors and state estimator. The planner then uses a wide-envelope model of the aircraft's dynamics to plan an optimal recovery trajectory and the associated control actions. The recovery trajectory and control actions need to return the aircraft from its current flight upset state to a recovered state within the aircraft's normal flight envelope. The specific aircraft's aerodynamic and structural limits have the be adhered to throughout the aerodynamic envelope recovery. The recovery task is formulated as an optimal control problem with the objective to perform the recovery as quickly as possible with the minimum amount of altitude loss. The sooner the first-stage aerodynamic envelope recovery can be completed, the sooner the second-stage attitude, flight path angle, and airspeed recovery can be initiated. The optimal control problem is solved using either an A^* grid-based search algorithm or an RRT sampling-based search algorithm. The deep stall recovery trajectory is planned using a three-degrees-of-freedom (3DoF) wide-envelope model of the aircraft dynamics. The spin recovery trajectory is planned using a six-degrees-of-freedom (6DoF) wide-envelope model of the aircraft dynamics.

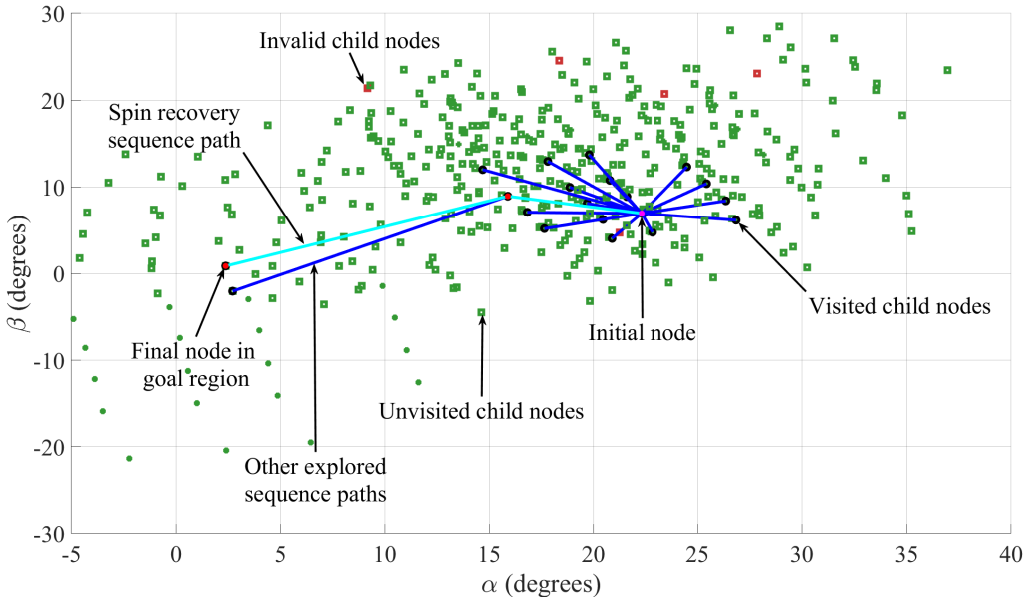

Figure 1.2: Trajectory planning for aircraft spin recovery.

For the second approach an appropriate recovery sequence from previously identified general recovery strategies is selected, instead of calculating one as done in the first approach. These general recovery strategies have been determined by observing a number of successful recovery sequences generated by the first approach. The second approach has the advantage that it does not incur the calculation time required in determining a valid recovery sequence. The second approach therefore can initiate the recovery actions immediately and therefore reduce the altitude loss which the aircraft experiences during a deep stall or spin recovery.

The valid recovery sequence or recovery strategy is passed to a trajectory regulator. The trajectory regulator applies the recovery control action sequences to the actual aircraft and regulates the state trajectory of the aircraft. The trajectory regulator ensures that the aircraft's states track the planned recovery trajectory. The regulator thereby compensates for parameter uncertainty and external disturbances.

During the execution of the recovery sequence the control switch monitors the state of the aircraft. Once the aerodynamic envelope has been recovered, the control switch transfers control of the aircraft to the second-stage recovery system. The second-stage recovery system is expected to damp the angular rates and perform the attitude, flight path angle, and airspeed recovery. The second-stage recovery system is the normal flight control system and its protection functions. Since the second-stage recovery system is beyond the scope of this project, a simple proportional rate damper controller is used to represent the second-state recovery system.

Once the aerodynamic envelope has been recovered, the control surfaces will again produce forces and moments that behave linearly. Therefore the normal flight control laws and protection laws become available to perform the attitude (pitch angle and bank angle), flight path angle and airspeed recovery. The deep stall and spin recovery system presented in this thesis aims to perform the first stage of the recovery, namely the aerodynamic envelope recovery. The second-stage of the recovery will be performed by a basic proportional angular rate damper for demonstration purposes only. The design of a full second-stage recovery system that performs the attitude, flight path angle, and airspeed recovery is beyond the scope of this research. However, an example of such a system can be found in the PhD thesis of Engelbrecht (2016) [9].

1.5 Project Execution

This thesis was approached and completed as follows. A literature study was performed on the aerodynamic modelling of stall and spin behaviour, manual and automatic stall and spin recovery techniques, and optimal trajectory planning and execution. The NASA GTM wide-envelope passenger aircraft simulation model was sourced to serve as the basis model for this research. It was attempted to model deep stall and spin behaviour without modifying the NASA GTM but this was unsuccessful. The NASA GTM aerodynamic model was modified to exhibit deep stall and spin dynamics. Simulations were performed to demonstrate that the modified aircraft model can be forced into a deep stall or a stable spin. For deep stall it was shown that the aircraft cannot be recovered using elevator actions only and for spin it was shown that the aircraft capable of sustaining a stable spin.

To address the problem of deep stall recovery it was formulated as an optimal control problem. An $A*$ search algorithm was applied to solve the optimal control problem. The algorithm successfully determined the optimal sequence of control actions and the resulting optimal state trajectory to recover the aircraft from deep stall. It was also possible to use a reduced-order aircraft model for the planning of the recovery sequence. Only the fast-rotational dynamics had to be modelled for the planning of the deep stall recovery. The deep stall recovery was verified in simulation using the full 6DoF wide-envelope aircraft model.

For the spin recovery problem it too was formulated as an optimal control problem, and $A*$ as well as a rapidly exploring random tree (RRT) search algorithm were applied to solve the optimal control problem. The optimal sequence of control actions and the resulting optimal state trajectory to recover the aircraft from spin were determined by the algorithms. For spin recovery, performing the planning using the simplified 3DoF aircraft model proved unsuccessful. The trajectory planning had to be performed using the full 6DoF aircraft model that models both the fast rotational and the slower translational dynamics.

The spin recovery system was verified in simulation using the full 6DoF wide-envelope aircraft model. The sequence of control actions determined by the trajectory planner was applied in an open-loop fashion to the full 6DoF simulation model. The simulation results show that the planned sequence of actions successfully recovers the aircraft from spin.

Techniques were investigated to determine how to execute the planned stall and spin recovery state trajectories. Both an open-loop as well as a closed-loop approach were proposed but the latter was chosen as it includes feedback control. The feedback control of the closed-loop approach provided disturbance rejection and robustness to model uncertainty. Model Predictive Control (MPC) was implemented in the form of a Linear Quadratic Regulator (LQR) to execute the planned trajectory. An algorithm was written to linearise the nonlinear NASA GTM model at each point along the planned recovery trajectory. A cost function, the discrete matrix Riccati equations, and linearised system matrices were set up to iteratively calculate the gain of the LQR. The state covariance and input covariance weights in the cost function were tuned to improve controller performance in the presence of turbulence and sensor noise.

A control switch was implemented to transfer flight control of the aircraft to the second-state recovery system of the aircraft once the aircraft has completed the aerodynamic envelope recovery. The switching criteria were verified using Monte Carlo simulations to ensure that the second-state recovery system stabilises the aircraft after the deep stall or spin recovery. Basic proportional rate damping control was implemented to represent the second-stage recovery system. The LQR and the control switch were implemented and were verified in simulation. The trajectory planning algorithms combined with the trajectory regulator produce the complete deep stall and spin recovery system.

Monte Carlo simulations were developed to test the performance and robustness of the

deep stall and spin recovery systems against varying initial conditions, turbulence levels, wind speed and direction, sensor noise, and model uncertainty. The state requirements for a successful recovery were documented and implemented as a testing function to determine if a deep stall or spin recovery simulation instance resulted in a successful recovery. Batch Monte Carlo simulations were run using the deep stall and spin recovery trajectory planner and regulator and the results were recorded. The results were analysed and general deep stall and spin recovery strategies were identified. The general deep stall and spin recovery strategies were implemented in place of the trajectory planner. This formed the basis of the second recovery system approach. Further Monte Carlo simulations were run to verify the second approach and the results were recorded and analysed.

1.6 Primary Contributions

This thesis presents a novel approach to stall and spin recovery. The recovery system uses optimal trajectory planning to determine the recovery control actions and the corresponding recovery state trajectories to recover the aircraft from a stall or spin state. The recovery system makes use of feedback control to reduce the effect that external disturbances and model uncertainty has on the stall or spin recovery.

1.7 Research Scope and Limitations

This research project aims only to perform flight envelope recovery. Recovery from over-speed, under-speed, attitude, flight heading and altitude upset is effectively done by already well developed algorithms such as found in [9]. A general transport aircraft model was used in this research and therefore the findings are not expected to be the same for other aircraft types. This research project also only focused on deep stall and spin flight upsets and does not account for flight upsets where structural damage has occurred to the aircraft which alters the flight dynamics of the aircraft.

The following limitations in this research were identified. The developed control systems are only verified in simulation and not on an actual aircraft due to safety concerns. To account for disturbance which an actual aircraft would experience the following was added to the simulation of the aircraft: A wide range of varied states were used to initialise the simulation such as airspeed which is varied from $70 ft/s$ to $330 ft/s$. Different external disturbances such as wind gusts and turbulence were modelled as described in the military specifications document MIL-F-8785C [7]. This research only uses one aerodynamic model, the NASA GTM, for verification. A number of different aerodynamic models of the NASA GTM were generated by altering key aerodynamic parameters to compensate for the use of only one aircraft model.

1.8 Thesis Outline

- Chapter 1 introduced the thesis and gave background knowledge about the research project. The research goals were specified, the proposed solution was briefly explained and a system overview of the the proposed system implementation was presented. A summary of how the research of this thesis was performed is given, the primary contributions of this research were stated and the scope and limitations of the project was outlined.

- Chapter 2 explores the available deep stall and spin dynamics research as well as previous proposed recovery strategies as a literature review. Trajectory planning methods and applications are also discussed along with a brief look into the different aircraft models used to model the dynamics of flight.
- Chapter 3 introduces the NASA GTM and discusses its development. The general fixed-wing aircraft model is presented and an overview of the NASA GTM simulation is given. Modifications to the NASA GTM aerodynamics to model both deep stall and spin were explained and verified in simulation.
- Chapter 4 addresses the deep stall recovery problem by firstly formulating the optimal control problem, then implementing the A^* solution and finally verifying the recovery trajectories in simulation.
- Chapter 5 uses a similar approach to address the problem of spin recovery. The optimal control problem is formulated and both the A^* solution and RRT solution is implemented. Finally the recovery trajectories are verified in simulation.
- Chapter 6 aims to improve the robustness of the recovery system against external disturbances by adding a trajectory regulator. A control switch which determines when the flight control can be transferred back to the normal flight controller is also added.
- Chapter 7 focuses on verifying and testing the deep stall and spin recovery systems using a Monte Carlo method approach. The results are discussed and observations on the performance of the control systems are given.
- Chapter 8 concludes the thesis and provides a few further recommendations and a summary of the research performed.

Chapter 2

Literature Survey

This chapter presents a literature review of previous research that is relevant to the problem of automatic stall an spin recovery. First, the concepts of stall, deep stall, and spin are defined and explained, and the techniques used by pilots to perform manual stall and spin recovery are described. Next, an overview is provided of previous research on automatic stall and spin recovery. Trajectory planning techniques are also discussed, since our intention is to use optimal trajectory planning to perform deep stall and spin recovery. Finally, a survey is provided of available wide-envelope aircraft models that can be used to test the automatic stall and spin recovery system in simulation.

2.1 Stall and Spin Recovery

The aircraft Upset Prevention and Recovery Training Aid (AUPRA) [2] explains that "An aircraft upset is an undesired aircraft state characterised by unintentional divergence from parameters normally experienced during operations." Recovery from these undesired states can be performed by the aircraft's natural stability, automatic flight system response, or by pilot intervention. Stall, deep stall and spin are all different forms of flight upsets.

A stall is when an aircraft experiences a sudden loss of lift. This happens when the aircraft exceeds its critical angle of attack. The angle of attack (AoA) of an aircraft is the angle at which the surrounding airflow intersects the aircraft's main wings. The smooth flow of air across the main wing detaches and becomes turbulent when the aircraft exceeds its critical AoA. This drastically reduces the effectiveness of the main wing's ability to generate the required lifting force to counteract the gravitational force on the aircraft. An aircraft can also stall if it has insufficient airflow across the main wings due to a low airspeed. Once stalled, the aircraft starts to lose altitude and without a form of recovery intervention the aircraft will crash.

If no stall recovery is performed, the aircraft will enter the post-stall flight regime. In this regime the aircraft has a high AoA and could experience the following aircraft motions; departure, post-stall gyration, spin, and deep stall. Departure is the transition period from a stall and into a post-stall gyration, spin, or deep stall. Departure is characterised by large and sudden unintended aircraft motions such as nose-slice and pitch up. Nose-slice is a lateral yaw divergence and pitch-up is a sudden increase in the angle of attack.

The Federal Aviation Administration describes in their Airplane Flying Handbook (2017) [10] that following a departure the aircraft will experience post stall gyrations which are uncontrolled motions about the aircraft axes, such as roll, pitch and yaw motions. Uncontrolled pitch-up and pitch-down motions could cause the aircraft to experience

brief periods of low angles of attack but due to the inertia of the aircraft, the aircraft is not stable. From this transient period the aircraft will either naturally recover to the safe wings-level flight state or enter a deep stall or spin state. In all three states; wings-level flight, deep stall and spin, the aircraft is intrinsically stable. If the aircraft is disturbed from its stable state it will return to its stable state. It therefore requires a large amount of control energy to transition the aircraft from one stable state to another, for example from a state of deep stall to a safe wings-level flight state.

To develop a recovery method which transitions the aircraft from a state of spin or deep stall, we first need to understand what a spin or a deep stall state is. A deep stall, also known as a super-stall, is a type of stall which affects certain types of aircraft designs. Deep stalls occur after an aircraft has entered a normal stall and its AoA increases far beyond the normal stall angle of attack. Due to this high angle of attack, the wakes of the stalled main wing, nacelle-pylon and the fuselage blanket and buffet the horizontal tail plane. Aircraft such as jet fighter aircraft with high horizontal tails and T-tail transport aircraft have difficulty in recovering from a deep stall. The control surfaces on the shadowed horizontal tail planes such as the elevator become ineffective. The elevator is used to generate a downwards pitching moment which is needed to pitch the nose of the aircraft down in order to recover from the stall. With reduced effectiveness the elevator is not capable of recovering the aircraft from a deep stall.

A proposed recovery method by Engelbrecht (2016) [9] is to generate a yawing moment using the rudder and thereby generate a side slip deflection. With a side slip deflection the tail of the aircraft should emerge from the wake of the turbulent air. The elevator should regain effectiveness and be able to produce sufficient downwards pitching moment to recover the aircraft from the deep stall. Another possible strategy, called the "pitch rocking" method, is to pitch the aircraft up and down at a specific resonant frequency, to build up the amplitude of the pitch angle oscillations until the AoA escapes the deep stall.

To model deep stall in a simulation it was noted by Engelbrecht (2016) [9] that the dynamics of deep stall are predominantly described by the rotational states of an aircraft such as the angular rates, roll, pitch, and yaw, as well as AoA and side slip angle. This could therefore enable the modelling of deep stall to be done in a reduced-order model which only model the rotational states of an aircraft.

In a spin the aircraft rotates about a vertical axis with the inner-wing being in a stalled state while the outer-wing still generates lift. This causes a more aggravated rolling, yawing and pitching motion which forces the aircraft into a downward spiral path. This rotation, also known as auto-rotation comes about due to difference in the AoA experienced by each wing of the aircraft. The outer wing which has a lower AoA and thereby generates more lift and less drag. The inner wing which is stalled experiences a higher AoA which produces less relative lift and more drag. This difference in lift and drag further exacerbates the spin. An aircraft may enter a spin if the pilot causes the aircraft to enter a cross-control stall while performing a skidding uncoordinated turn.

An aircraft spin has four consecutive phases: spin entry, incipient spin, developed spin, and spin recovery. Spin entry is the phase in which the aircraft stalls asymmetrically or in a yawed state and then proceeds to rotate about its vertical axis as described above. Incipient spin is the transient transition between spin entry and a developed spin and is characterised by a sudden increase in angular rates and angle of attack. Incipient spin lasts between two to three rotations before settling into a steady-state spin also known as a developed spin. In a developed spin the aircraft's angular rotation rate, airspeed and vertical speed stabilize. The flight path of the aircraft is vertical or near vertical downwards. The Airplane Flying Handbook by the Federal Aviation Administration (2017) [10] states that each aircraft manufacturer provides a specific spin recovery procedure for each aircraft which pilots must study before flying the aircraft. In general spin recovery follows this

procedure: reduce power to idle, position ailerons to neutral, apply full opposite rudder against the rotation, apply positive and straight forward elevator, neutralize the rudder after the spin rotation stops, apply back elevator pressure to return to wings-level flight. Spin recovery is successful if the rotation stops and the AoA of the wings are reduced below the stall angle of attack.

An optimal recovery from either stall, deep stall or spin is a recovery which has the best performance according to specific criteria. At first it would seem that reducing the loss in altitude would be the main performance measure for a recovery. A recovery procedure would then be optimised to minimise the altitude loss. But the lowest lost altitude recovery would not be of any help if it takes too long to calculate. Therefore an optimal recovery is one which is calculated within a reasonably short amount of time and reduces the amount of altitude lost during the recovery.

Altitude recovery is a well developed field and optimal altitude recovery methods have already been developed. These methods require that the aircraft must be within its normal flight envelope. As explained by Crespo (2012) [5] the normal flight envelope of an aircraft is a flight regime which is specified by limits on certain states of the aircraft such as the AoA can only range between one to six degrees.

2.2 Automatic Stall and Spin Recovery Research

Only with recent adaptation of automatic flight for aircraft has the field of automatic stall and spin recovery research started to become more prominent. Stall and spin recovery is a highly complex problem as the aerodynamics in stall and spin are non-linear and different for each aircraft. Yet even with these hurdles a number of methods to perform automatic stall and spin recovery have been developed.

Engelbrecht (2016) [9] proposed two flight envelope recovery approaches. He focused on large transport aircraft and initially studied a passive method to recover the aerodynamic envelope using the natural stability of the aircraft. Once the envelope has been recovered, the conventional flight control laws combined with their flight envelope protection functions would take over and perform attitude, speed and altitude recovery. His research shows that it is a valid approach to automatic stall and spin recovery if the aircraft is naturally stable across a large range of attitude states. Recoveries using this method take much longer as it depends on the natural damping characteristics of the aircraft. This method cannot be used for deep stall recovery as the deep stall state is also naturally stable.

Engelbrecht (2016) [9] also presented an active method to recover the aerodynamic envelope which makes use of time scale separation between the aircraft's fast rigid body rotational dynamics and it's slower point mass translational dynamics. He developed a Lyapunov inner-loop controller to recover the angular rates and the aerodynamic envelope. An outer-loop control based on optimal control theory is used to recover the attitude, flight path angle, and airspeed.To simulate and test these two methods of automatic stall and spin recovery Engelbrecht used the General Transport Model (GTM) simulation model, which was developed by NASA Langley.

Goman (1993) [14] proposed two different approaches to spin recovery. The positional recovery method aims to mimic the procedure which pilots would manually use to recover from a spin. The pitch rocking method is proposed as an alternative recovery method when situations arise where there is insufficient nose-down pitching control power and a low level of control power in roll and yaw at high angle of attack. These situations include flat spin and deep stall regimes and are difficult to recover from using the positional recovery method. This method requires the aircraft to be pitched up and down at a certain frequency as to build up enough rocking oscillation energy to escape the flat spin or deep stall. Both

methods were tested in simulation using the Krit Scientific Package and later validated in test flights and shown to work effectively.

Lee (2004) [19] approaches automatic spin recovery as a nonlinear optimal control problem. The method aims to control the momentum vectors of the aircraft and thereby reduce the kinetic energy of the aircraft while in a spin. This method was simulated using a full nonlinear aerodynamic model and compared to actual spin recovery data. Two different types of spin where simulated and the method is capable of recovering the aircraft from both spin types and is closely comparable to actual spin recovery data. For the implementation of such a method it can be performed by either the provision of an advisory to the pilot as to what control input sequence is required, or the method may be implemented as an automatic controller that will produce these controls.

Wang (2010) [29] proposed a fuzzy recovery controller to perform deep stall recovery. It is based on the Particle Swarm Optimization method and makes use of the dynamic recovery method, also known as the pitching oscillation or pitch rocking method, which was described by M. Goman in the previous paper[14]. The method was applied in simulation and proved to be an effective way of performing deep stall and spin recovery.

Yildiz (2018) [31] developed a similar method for spin and stall recovery to that of Engelbrecht (2016) [9]. In their paper they presented a recovery approach which is based on Fedral Aviation Administration's (FAA) guidelines for upset recovery. They used a 6 DOF nonlinear F-16 model to demonstrate their method which makes use of a finite state machine. The state machine first normalizes angular rates, then determines the aerodynamic state in which the aircraft is and then applies the recovery procedure as specified by the FAA.

Raghavendra (2005) [27] employed the method of nonlinear dynamic inversion for spin recovery. It is ideally suited for solving the problem of recovering an aircraft from spin to a level-trim-flight condition. The controller is designed to recover the aircraft from a spin condition to three different AoA states (high, moderate and low). Bifurcation Analysis was used to identify if developed control strategy does not put aircraft at risk of being pulled back into a different stable spin state. To verify the controller they made use of the high-angle-of-attack research vehicle (HARV).

Sinha (2010) [28] presented an automatic spin recovery method that makes use of a variable-structure-technique-based controller which is more robust in the presence of model uncertainties and external disturbances. The controller computes the control commands which should transfer aircraft from an oscillatory spin state to a wings level flight trim state and applies this to the aircraft to perform spin recovery. This paper also used the high-angle-of-attack research vehicle to verify the controller.

Garcia (2015) [13] used a general method of aircraft recovery. They developed a dynamic optimization algorithm which calculates updated control commands with an adaptive horizon length to recover the aircraft. They make use of an artificial neural network to constantly updates the aircraft model which the controller uses in calculating the optimal recovery trajectory.

2.3 Trajectory Planning

A trajectory is a description of a system's states as a function of time. Trajectory planning means determining the state trajectory and the associated control signal to steer a system from an initial state to a desired final state. An aircraft's trajectory is commonly described by the following state time-series: AoA, side slip angle, roll, pitch, and yaw rate, roll, pitch, and yaw angle, altitude, and airspeed. Stall and spin recovery therefore implies determining the trajectory which will recover the aircraft to the desired state which is wings-level flight.

2.3.1 Current Methods

Trajectory planning is a well developed field of research which has many applications. Notable trajectory planning algorithms which are used in industry include Dijkstra's algorithm, A*, Rapidly-expanding random tree (RRT) and Probabilistic Road Map (PRM). Each algorithm has their own variants which improve upon their performance in one way or another. All path planning algorithms focus on finding a valid path between the current state and the desired state. Secondary objectives are to find the best path or to find a path as fast as possible. Most of the algorithms try to find a balance between the two competing objectives and can be adjusted to favour one objective over the other.

As explained by LaValle (2006) [18], Dijkstra's algorithm is an algorithm which finds the shortest path between two nodes in a given graph of nodes. It is also guaranteed to find a path if a path exists between the two nodes. Dijkstra's algorithm searches in all directions which causes it to be one of the slowest algorithms in finding a valid path. The A* algorithm improves upon Dijkstra's algorithm by directing its search. It is also guaranteed to find the shortest path. The RRT algorithm on the other hand is not guaranteed to find the shortest path first but it will find a path and then improve that path as it keeps searching and will find the shortest path in the limit as time approaches infinity. RRT is capable of efficiently searching spaces which consist of a high number of dimensions and which are non-convex. PRM takes random samples from the search space, tests if they are valid and collision-free, and then tries to connect the samples to each other by using a local planner such as Dijkstra's algorithm.

2.3.2 Relevant Applications

Pharpatara (2015) [26] applies a number of trajectory planning algorithms in his doctoral thesis "Trajectory planning for aerial vehicles with constraints". He notes that trajectory planning for aircraft is very difficult and challenging as the dynamics are complex, nonlinear and nonholonomic. The RRT search algorithm is applied as the path planning algorithm. Both the dynamics of the aircraft and the constraints of the environment are taken into consideration while the algorithm searches for a feasible path. Performance of the algorithm is improved by expanding the RRT algorithm to use a heuristic function which makes it RRT* and allowing it to use an artificial potential field of the state space. This artificial potential field is calculated before applying the RRT* algorithm. The RRT* also makes use of a more simplified vehicle dynamics model to further improve performance.

2.4 Wide Envelope Aircraft Models

Earlier in the chapter we discussed the work done by different authors regarding stall and spin recovery. We noted the different aircraft models which they used and will discuss two of them here in more detail. To perform research in the area of stall and spin recovery we require an aircraft flight model which is capable of modelling the aerodynamics of the aircraft over a wide range of AoA, sideslip angle, and angular rate. These models are known as wide envelope aircraft models and the notable models include NASA GTM, ADMIRE, HARV, SUPRA and HHIRM. A choice between the NASA GTM and ADMIRE models where given for this research and therefore only these two will be discussed.

2.4.1 Generic Transport Model

To safely perform experimental flight tests outside the normal flight envelope NASA developed the Generic Transport Model (GTM) research vehicle. The GTM is a 5.5% dynam-

ically scaled unmanned aerial vehicle (UAV) of a large transport aircraft. Wide-envelope aerodynamic models were developed for the GTM based on wind tunnel tests over an extensive range of angles of attack, sideslip angles, angular rates, and control surface deflections [6, 12, 22, 23]. By using these aerodynamic models a full nonlinear simulation model of the GTM was developed and made available by NASA for passenger aircraft upset recovery research [15]. The GTM is well adopted by both academics and industry for research on upset recovery for large transport aircraft and the dynamics of aircraft in nonlinear flight regions. Similar to most large transport aircraft the GTM allows for control of its dynamics using the engine thrust, and aileron, elevator and rudder control surface deflections.

2.4.2 Aero-Data Model in a Research Environment

The Swedish Defence Materiel Administration contracted the Aeronautical Research Institute of Sweden to develop a simulation model of a rigid small single seater fighter aircraft. As explained by Forssell (2005) [11] the Generic Aerodata Model (GAM) which was developed by Saab AB and the Swedish Royal Institute of Technology was used as a basis for the simulation. A nonlinear, six degree of freedom simulation model of a rigid small fighter aircraft with delta-canard configuration was developed and is now known as the Aero-Data Model in a Research Environment (ADMIRE). ADMIRE is maintained by FOI, Sweden as a publicly available research vehicle.

2.5 Literature Review Conclusions

The following conclusions that are applicable to this research were drawn from the literature review:

- Deep stall recovery is largely based on the fast rotational dynamics and not on the slower translational dynamics. A reduced order model which only models the three rotational degrees of freedom of an aircraft can be used to model deep stall dynamics.
- In a spin condition there is a strong coupling between the rotational and the translational dynamics of the aircraft. The full six-degrees-of-freedom aircraft model is therefore required to model the spin dynamics.
- The dynamics of large transport aircraft engines are slow compared to the fast rotational dynamics of large transport aircraft. Stall and spin recoveries are performed within a time span which is too short for the engines of the aircraft to be used for the recovery. Most manual stall and spin recovery techniques require the aircraft's thrust to be set to neutral.
- Most stall and spin recovery methods require the ailerons to be set to neutral. This is due to the uncertainty of the control dynamics of the aileron control surfaces while the aircraft is in a stall or a spin.
- Automatic stall and spin recovery has received much more research attention in the field of military aircraft than in the field of large transport aircraft.
- A* path planning algorithm is a widely used algorithm and performs better in all cases compared to Djikstra's algorithm.
- RRT algorithm is capable of efficiently finding valid paths in search spaces which consist of a large number of dimensions.

- The flight envelope of an aircraft is the domain of flight conditions in which the aircraft can safely be operated without exceeding its aerodynamic and structural dynamics. If an aircraft finds itself to be within this domain its dynamics is largely linear.
- Flight control laws for flight within the flight envelope of an aircraft are well established in industry and academia. This is due to the linear flight dynamics of aircraft within the flight envelope.
- All stall and spin recovery techniques found in the literature prioritise recovering the aerodynamic envelope of the aircraft as fast as possible over minimising the altitude loss during the recovery.

2.6 Research Decisions

Based on the literature review the following research decisions were made:

- The NASA GTM simulation model will be used as the basis for this research on automatic deep stall and spin recovery due to being well accepted in the field of flight upset recovery research.
- The elevator and rudder control surfaces will be used to perform the control actions for both stall and spin recovery as these are the prescribed control surfaces to be used in manual stall and spin recovery procedures.
- The engine thrust and aileron control surface will be kept neutral during the stall and spin recovery as is prescribed by manual stall and spin recovery procedures.
- Automatic deep stall recovery will be addressed instead of stall recovery as stall recovery is a well developed field of research in large transport aircraft.
- The GTM model does not exhibit deep stall dynamics and will therefore have to be modified to model deep stall dynamics.
- A* and RRT will be implemented and compared as the trajectory planning algorithms.
- It will be assumed that the existing flight control laws are capable of completing the recovery of airspeed, altitude and orientation once the aircraft enters the domain of its normal flight envelope. Therefore this research will solely focus on recovering the aircraft from a state of deep stall or spin to a state which is within the domain of its normal aerodynamic envelope. This envelope is characterised by acceptable ranges of AoA, sideslip angle, and angular rates.
- To perform optimal stall and spin recovery the path planning algorithms will first aim to minimise the duration of the recovery and then secondly reduce the loss of altitude during the recovery.
- The stall and spin recovery system assumes that the flight upset condition will be detected and identified by an independent module. The recovery system will then activate the appropriate recovery procedure based on whether deep stall or spin is identified as the upset condition. The upset detection and identification function is however beyond the scope of this research.

Chapter 3

NASA GTM Aircraft Model

This chapter describes the modified NASA GTM wide-envelope aircraft model that was used as the basis for the design and verification of the deep stall and spin recovery system. The NASA Generic Transport Model (GTM) is a 5.5% dynamically scaled unmanned aerial vehicle (UAV) of a large transport aircraft that was developed by NASA for experimental flight tests outside the normal flight envelope. Wide-envelope aerodynamic models were developed for the GTM based on wind tunnel tests over an extensive range of angles of attack, sideslip angles, angular rates, and control surface deflections. A full nonlinear simulation model of the GTM was created and made available by NASA for passenger aircraft upset recovery research[9]. For this project, the aerodynamic model of the NASA GTM was modified to exhibit deep stall and spin behaviour.

The material in this chapter is presented as follows: First, some background about the development and validation of the NASA GTM is given. Next the general flight dynamics model for a fixed-wing aircraft is established. The axis systems and notation are defined, and the standard 6DoF equations of motion and general forces and moments model for an aircraft are briefly presented. The implementation of the wide-envelope aerodynamic model for the NASA GTM is discussed in more detail. This is followed by a high-level description of how the NASA GTM mathematical model is implemented as a Simulink model. This Simulink model will from now on be referred to as NASA GTM simulation.

Next the modifications to the NASA GTM aerodynamic model to enable deep stall and spin behaviour are then described. Finally, the modified NASA GTM simulation is run to show that the modified aircraft model can be pushed into deep stall or spin, and cannot be easily recovered using intuitive control surface commands.

3.1 Development of the NASA GTM

NASA developed the Generic Transport Model (GTM) unmanned aerial vehicle (UAV) to perform experimental flight tests out sided the normal flight envelope. The NASA GTM is a 5.5% dynamically scaled model UAV of a large transport aircraft as shown in Figure 3.1. The NASA GTM was developed as part of the NASA Aviation Safety Program's Integrated Resilient Aircraft Control Project. This project focused on researching the flight dynamics and control of large transport aircraft in upset conditions. The NASA GTM forms part of the Airborne Sub-scale Transport Aircraft Research (AirSTAR) test-bed at NASA Langley Research Centre (LaRC). Its role was to reduce the risks involved in the study of critical flight conditions outside the normal flight envelope. Experiments which required full-scale manned aircraft flight tests could now be performed using the NASA GTM. [16]

Figure 3.1: The NASA Generic Transport Model (image supplied with the NASA GTM simulation)

The NASA GTM is remotely piloted using an L-band telemetry link. It is powered by two turbine engines and has swept wings. The NASA GTM has the following control surfaces: The elevator is used for pitch angle and rate control, the rudder is used for yaw angle and rate control, the ailerons are used for roll angle and rate control. The stabilizer is used to assist in trimming the aircraft for level-flight and is change continuously throughout the flight as the centre of gravity of the aircraft shifts due to fuel be being used. The flaps are used to increase the lift that a wing produces at low air speeds and thereby reduces the aircraft's stall speed and is used during take-off and landing and then retracted during normal flight. [6]

While the NASA GTM is flown the following sensors were used to gather these measurements: Three-axis linear acceleration, three-axis angular rate, estimated attitude angles, and GPS velocity and position measurements are provided by the inertial measurement system. AoA, sideslip angle, dynamic pressure and static pressure are measured by anemometric sensors. Engine speed is measured and reported by the engine control unit. Air density and altitude are determined using static pressure and temperature. Airspeed is calculated using dynamic pressure.

To develop the wide-envelope aerodynamic model of the NASA GTM a model with the same mould line specifications was built and used in the wind tunnel tests. Data gathered in the wind tunnel tests was then used to develop the aerodynamic model. A combination of different wind tunnel tests were performed. Static wind tunnel test measured the contribution of AoA, sideslip angle and control surface deflections on the aerodynamic forces and moments. Dynamic wind tunnel tests such as rotary balance and forced oscillation testing were performed and the data captured by these tests were blended using the Hybrid-Kalviste method to determine the total contribution of the aircraft's angular rates on the aerodynamic model. [22]

3.2 Flight Dynamics Model for a Fixed-Wing Aircraft

This section will first introduce the general six degrees-of-freedom (6DoF) equations of motion and general forces and moments model for an aircraft. The general flight dynamics model for a fixed-wing aircraft is well-established in literature and is repeated here for the convenience of the reader. The primary source for the fixed-wing aircraft model presented in this section is the Advanced Automation 833 lecture notes compiled by Peddle and Engelbrecht [8]. Finally a description of the NASA GTM wide-envelope aerodynamic model implementation into the 6DoF mathematical model is presented.

3.2.1 Axis Systems

This section introduces the axis systems and notation commonly used in aircraft dynamics modelling.

Inertial Axis System

To apply Newton's equations of motion, an inertial axis system is needed. The standard North-East-Down (NED) axis system shown in Figure 3.2 adequately approximates an inertial axis system over the relatively short distances that the aircraft travels during a recovery. This axis system assumes that the earth is flat and non-rotating. The positive x_I-axis points in the north direction, the positive y_I-axis points in the east direction, and the positive z_I-axis points in the down direction towards the centre of the earth. The origin of the (NED) axis system is any arbitrary point that is fixed relative to the surface of the Earth.

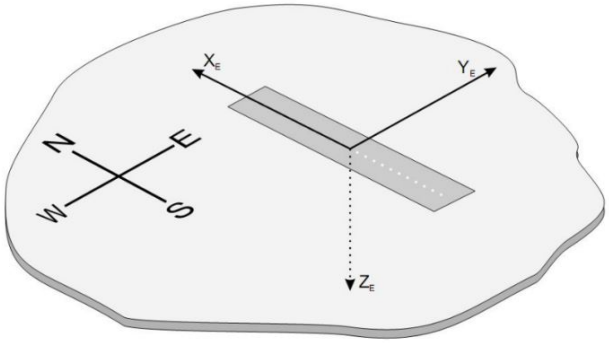

Figure 3.2: North-East-Down Axis System (Image from the Advanced Automation 833 lecture notes. [8])

Body Axis System

The body axis system, shown in Figure 3.4, is used to represent the aircraft's position and orientation relative to the inertial axis system. The body axis system is fixed to the aircraft and travels with the aircraft. The equations of motion of the aircraft are most conveniently described in terms of forces, moments, and angular rates coordinated in the body axis system. The origin of this axes system is the aircraft's centre of gravity. The positive x_b-axis points out the nose of the aircraft, the positive y_b-axis points out the right wing of the aircraft, and the positive z_b-axis is perpendicular to the x_b,y_b-plane and points downward relative to the cockpit.

Wind Axis System

The wind axis system is used to model the aerodynamic forces and moments acting on the aircraft. The wind axes system also has its origin at the aircraft's centre of gravity. The positive x_w) axis points in the direction of the aircraft's velocity vector, the positive z_w) axis lies in the aircraft's plane of symmetry and points in the down direction, and the positive y_w) axis is perpendicular to the x_w,z_b-plane and points in the direction of the starboard wing.

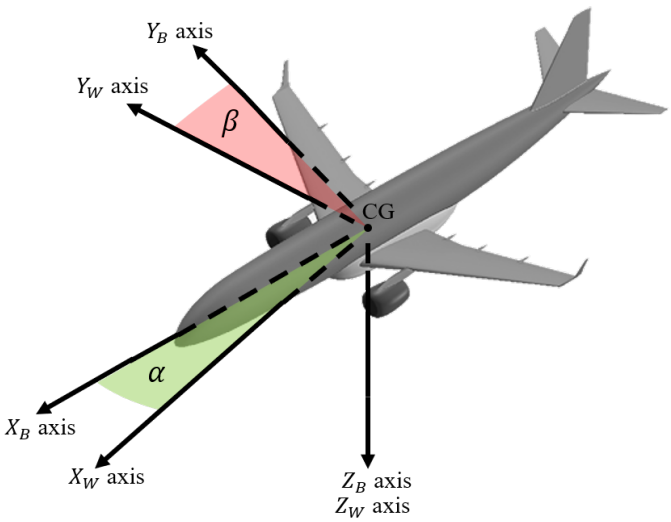

Figure 3.3: Wind Axis System and Rotation to Body Axis

3.2.2 Notation

The standard notation for the aircraft forces and moments, linear and angular velocities, and control surface deflections, are shown in Figure 3.4 and are defined below.

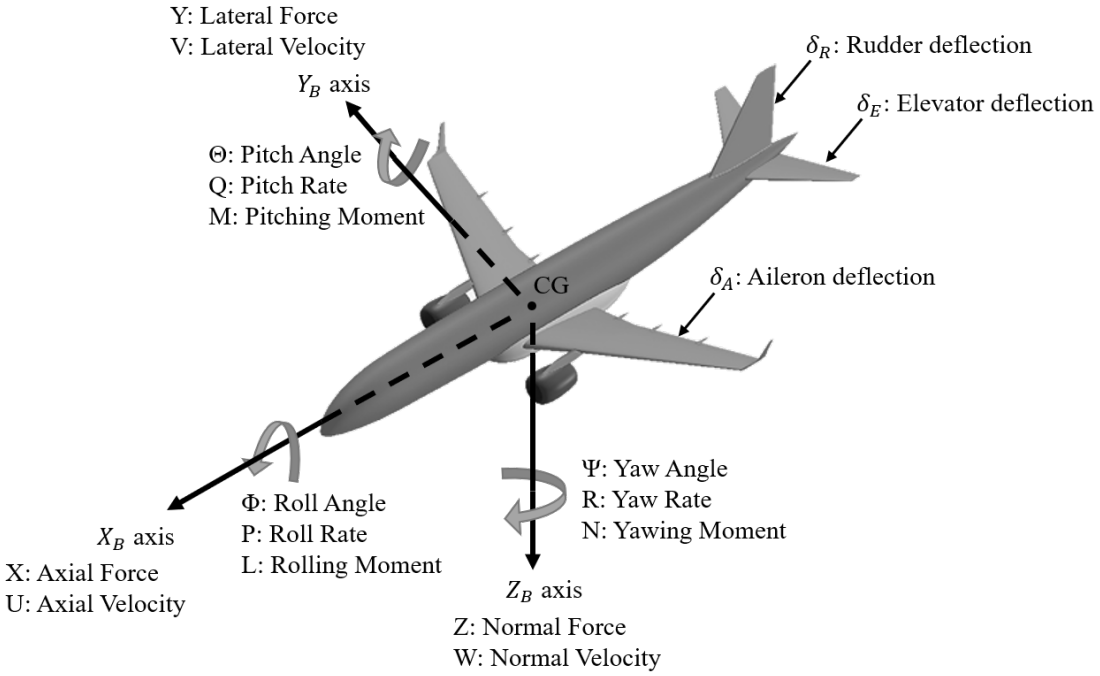

Figure 3.4: Aircraft body axis system and variables. (Reproduced from the Advanced Automation 833 lecture notes. [8])

- Coordinates of the force vector in body axes: X (axial), Y (lateral), Z (normal) force.
- Coordinates of the moment vector in body axes: L (roll), M (pitch), N (yaw) moment.
- Coordinates of the linear velocity vector in the body axes: U (axial), V (lateral), W

(normal) velocity.

- Coordinates of the angular velocity vector in the body axes: P (roll), Q (pitch), R (yaw) rate.

- Control surface deflection: δ_A (Aileron), δ_E (Elevator), δ_R (Rudder) with a positive deflection defined as one that produces a negative moment.

3.2.3 Attitude Representation

First the orientation of the body axis to the inertial axis system is described and then the orientation of the wind axis system to the body axis is explained.

Euler angles are used to describe the orientation of the body axis system to the inertial axis system. The Euler angles parameterise the attitude of the aircraft as a sequence of three axis rotations. The order of the rotations is important and a number of different Euler angle sequences exist. The Euler 3-2-1 sequence is used and works as follows; first both axis systems are aligned, second the body axes are rotated positively about the z_b axis by the heading angle ψ, third the body axes are positively rotated about the y_b axis by the pitch angle θ, and finally the body axes are rotated positively about the x_b axis by the roll angle ϕ. It is important to note that using this sequence has a singularity at $\Theta = +-90$ deg pitch angle.

The orientation of the wind axis system relative to the body axis system is represented by two angles, namely the AoA (α) and the sideslip angle (β). First both axis systems are aligned, second the wind axis is positively rotated about the y_w axis by the AoA, and finally the wind axes are positively rotated about the z_w axis by the sideslip angle.

3.2.4 Kinematics

Kinematics is a field in classical mechanics that describes the motion of points, bodies, and systems of bodies. It considers the initial conditions such as position, velocity, and acceleration of points within the system and by using geometry it can determine the position, velocity and acceleration of any unknown parts of the system. Kinematics does not deal with how forces act on bodies as this lies in the field of Kinetics which will be discussed in the next section.

For the position vector its coordinates are defined as N, E, D in the inertial axis system. Attitude parameters of the body axis system with respect to the inertial axis system are defined as ϕ, θ, ψ. The relationship between the aircraft position and velocity in the inertial axis system is given by:

$$\begin{bmatrix} \dot{N} \\ \dot{E} \\ \dot{D} \end{bmatrix} = \begin{bmatrix} V_N \\ V_E \\ V_D \end{bmatrix} \tag{3.1}$$

where V_N, V_E, and V_D are the velocity coordinates in the inertial axis system. The body axes velocity coordinates (U, V, W) are related to the inertial axes velocity coordinates (V_N, V_E, V_D) through the inverse Direction Cosine Matrix (DCM) as follows:

$$\begin{bmatrix} \dot{N} \\ \dot{E} \\ \dot{D} \end{bmatrix} = \begin{bmatrix} C_\Psi C_\Theta & C_\Psi S_\Theta S_\Phi - S_\Psi C_\Phi & C_\Psi S_\Theta C_\Phi + S_\Psi S_\Phi \\ S_\Psi C_\Theta & S_\Psi S_\Theta S_\Phi + C_\Psi C_\Phi & S_\Psi S_\Theta C_\Phi - C_\Psi S_\Phi \\ -S_\Theta & C_\Theta S_\Phi & C_\Theta C_\Phi \end{bmatrix} \begin{bmatrix} U_b \\ V_b \\ W_b \end{bmatrix} \tag{3.2}$$

with $C_{()} = \cos()$ and $S_{()} = \sin()$. The body axes angular rates of the aircraft are related

to the rate of change of the Euler angles through the following transformation:

$$\begin{bmatrix} \dot{\Phi} \\ \dot{\Theta} \\ \dot{\Psi} \end{bmatrix} = \begin{bmatrix} 1 & sin(\Phi)tan(\Theta) & cos(\Phi)tan(\Theta) \\ 0 & cos(\Phi) & -sin(\Phi) \\ 0 & sin(\Phi)sec(\Theta) & cos(\Phi)sec(\Theta) \end{bmatrix} \begin{bmatrix} P_b \\ Q_b \\ R_b \end{bmatrix} \tag{3.3}$$

3.2.5 Kinetics

The kinetic equations relate the linear and angular velocity of the aircraft to the forces and moments applied to the aircraft. For a rigid aircraft the following equations of motion based in an inertial frame of reference can be derived from Newton's second law of motion. m is the mass of the aircraft and I_B is the moment of inertia of the aircraft in body axes:

$$I_B = \begin{bmatrix} I_{xx} & I_{xy} & I_{xz} \\ I_{xy} & I_{yy} & I_{yz} \\ I_{xz} & I_{yz} & I_{zz} \end{bmatrix} \tag{3.4}$$

Due to the symmetry of an aircraft about the X_BZ_B-plane, the products of inertia about I_{xy} and I_{yz} are small and assumed to be zero. The linear and angular velocity of the aircraft are related to the forces and moments acting on the aircraft through the following 6DoF equations of motion in vector form:

$$\mathbf{F}_B = \frac{d}{dt}(m\mathbf{V}_B) + \omega_B \times (m\mathbf{V}_B) \tag{3.5}$$

$$\mathbf{M}_B = \frac{d}{dt}(\mathbf{I}_B\omega_B) + \omega_B \times (\mathbf{I}_B\omega_B), \tag{3.6}$$

which are the general 6DoF vector equations of motion and can also be represented in scalar form:

$$X = m(\dot{U} + WQ - VR) \tag{3.7}$$
$$Y = m(\dot{V} + UR - WP) \tag{3.8}$$
$$Z = m(\dot{W} + VP - UQ) \tag{3.9}$$
$$L = \dot{P}I_x - \dot{R}I_{xz} + QR(I_z - I_y) - PQI_{xz} \tag{3.10}$$
$$M = \dot{Q}I_y + PR(I_x - I_z) + (P^2 - R^2)I_{xz} \tag{3.11}$$
$$N = \dot{R}I_z - \dot{P}I_{xz} + PQ(I_y - I_x) + QRI_{xz} \tag{3.12}$$

Figure 3.4 shows how the kinetic equations and kinematic equations interlink. The dynamics of a system are driven by inputs such as forces and moments. The kinetic equations of 3.7 and 3.10 relate these forces and moments to rates of change of the linear and angular velocity respectively. The kinematic equations of 3.2 and 3.3 in turn relate the linear and angular velocity to rates of change in attitude and position. These equations of motion are not aircraft specific, except for the assumptions made, and can be applied to any rigid body.

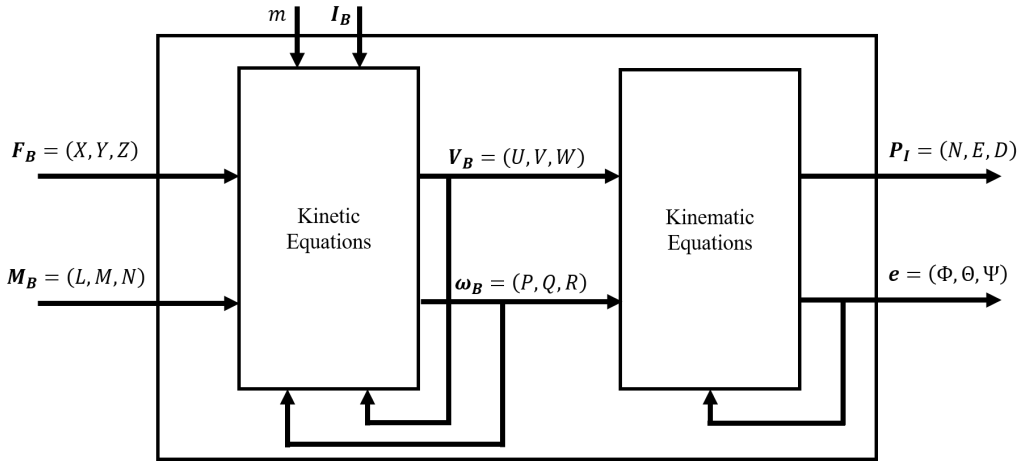

Figure 3.5: Block diagram of the aircraft's 6DoF EOM model. Reproduced from AA833 course notes[8].

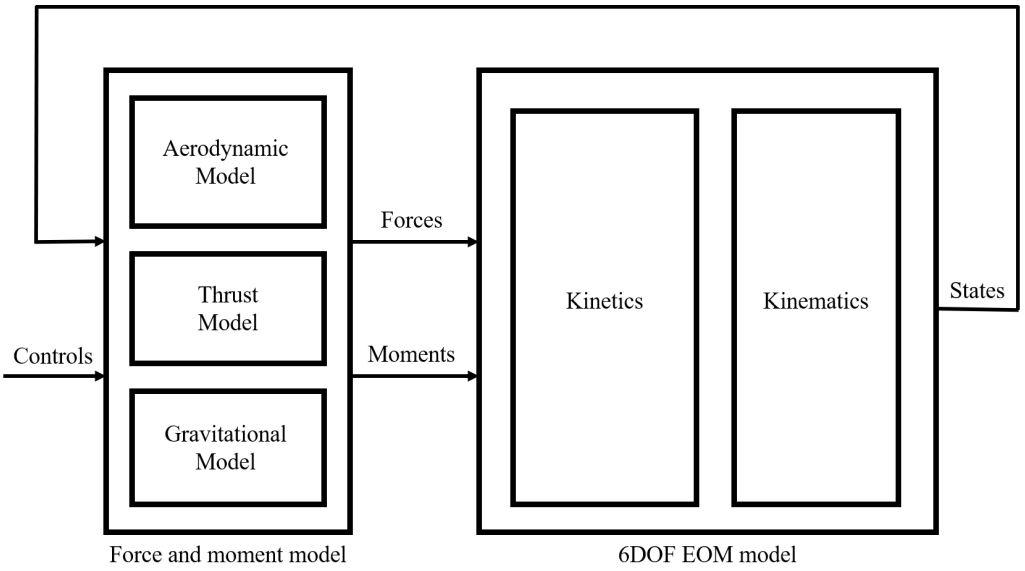

Figure 3.6: Block diagram of aircraft flight dynamics model. Reproduced from AA833 course notes[8].

3.2.6 Forces and Moments

Forces and moments which act on an aircraft can be categorised in three groups namely, aerodynamic, gravitational and thrust.

Aerodynamic

The aerodynamic forces and moments are the most complex to model and introduce most of the uncertainty into the aircraft model. The aerodynamic forces and moments are proportional to the air density and the square of the velocity of the aircraft, as quantified by the dynamic pressure ($\bar{q}$):

$$\bar{q} = \frac{1}{2}\rho \overline{V}^2, \tag{3.13}$$

where ρ is the air density and $\overline{V}$ is the airspeed. The aerodynamic forces and moments coordinated in the body axis system are expressed by the following equations:

$$X^A = \bar{q}SC_X \tag{3.14}$$
$$Y^A = \bar{q}SC_Y \tag{3.15}$$
$$Z^A = \bar{q}SC_Z \tag{3.16}$$
$$L^A = \bar{q}SbC_l \tag{3.17}$$
$$M^A = \bar{q}S\bar{c}C_m \tag{3.18}$$
$$N^A = \bar{q}SbC_n \tag{3.19}$$

where S is the wing area, b is the wing span, $\bar{c}$ is the mean aerodynamic chord and $C_{()}$ are the non-dimensional aerodynamic force and moment coefficients. In general, the non-dimensional force and moment coefficients are nonlinear functions of the airspeed, angle of attack, sideslip angle, angular rates, and control surface deflections, as follows:

$$C_X = F_{CX}(\overline{V}, \alpha, \beta, P, Q, R, \delta_A, \delta_E, \delta_R) \tag{3.20}$$
$$C_Y = F_{CY}(\overline{V}, \alpha, \beta, P, Q, R, \delta_A, \delta_E, \delta_R) \tag{3.21}$$
$$C_Z = F_{CZ}(\overline{V}, \alpha, \beta, P, Q, R, \delta_A, \delta_E, \delta_R) \tag{3.22}$$
$$C_l = F_{Cl}(\overline{V}, \alpha, \beta, P, Q, R, \delta_A, \delta_E, \delta_R) \tag{3.23}$$
$$C_m = F_{Cm}(\overline{V}, \alpha, \beta, P, Q, R, \delta_A, \delta_E, \delta_R) \tag{3.24}$$
$$C_n = F_{Cn}(\overline{V}, \alpha, \beta, P, Q, R, \delta_A, \delta_E, \delta_R) \tag{3.25}$$

Gravity

In the inertial axis system the gravitational force is modelled as a force which is equivalent to the aircraft's mass and pointed in the down direction.

$$\boldsymbol{F}_{\boldsymbol{I}}^{\boldsymbol{G}} = \begin{bmatrix} 0 \\ 0 \\ mg \end{bmatrix} \tag{3.26}$$

Using the DCM this force is transformed to the body axis system as shown below,

$$\begin{bmatrix} X^G \\ Y^G \\ Z^G \end{bmatrix} = \begin{bmatrix} C_\Psi C_\Theta & S_\Psi C_\Theta & -S_\Theta \\ C_\Psi S_\Theta S_\Phi - S_\Psi C_\Phi & S_\Psi S_\Theta S_\Phi + C_\Psi C_\Phi & C_\Theta S_\Phi \\ C_\Psi S_\Theta C_\Phi + S_\Psi S_\Phi & S_\Psi S_\Theta C_\Phi - C_\Psi S_\Phi & C_\Theta C_\Phi \end{bmatrix} \begin{bmatrix} 0 \\ 0 \\ mg \end{bmatrix} \tag{3.27}$$

which simplifies to,

$$\begin{bmatrix} X^G \\ Y^G \\ Z^G \end{bmatrix} = \begin{bmatrix} -\sin\Theta \\ \cos\Theta \sin\Phi \\ \cos\Theta \cos\Phi \end{bmatrix} mg \tag{3.28}$$

The origin of the body axis system has been placed at the centre of gravity of the aircraft. Therefore there will be no moments due to gravity acting on the aircraft.

$$\begin{bmatrix} L^G \\ M^G \\ N^G \end{bmatrix} = \begin{bmatrix} 0 \\ 0 \\ 0 \end{bmatrix} mg \tag{3.29}$$

Thrust

The thrust force is assumed to be directed parallel to the positive x-axis of the body axis.

$$X^T = T \tag{3.30}$$

and zero in the other directions,

$$Y^T = Z^T = 0; \tag{3.31}$$

It will be assumed that the thrust force lies along the x-axis and that there is a no moment arm and therefore no moment is generated. Moments due to thrust are therefore assumed to be as follows:

$$\begin{bmatrix} L^T \\ M^T \\ N^T \end{bmatrix} = \begin{bmatrix} 0 \\ 0 \\ 0 \end{bmatrix} \tag{3.32}$$

Summary

The total force and moment acting on the aircraft is the sum of the aerodynamic, gravitational, and thrust forces and moments.

$$X = X^A + X^G + X^T \tag{3.33}$$
$$Y = Y^A + Y^G + Y^T \tag{3.34}$$
$$Z = Z^A + Z^G + Z^T \tag{3.35}$$
$$L = L^A + L^G + L^T \tag{3.36}$$
$$M = M^A + M^G + M^T \tag{3.37}$$
$$N = N^A + N^G + N^T \tag{3.38}$$

3.2.7 Control Surface Actuator Response

The response of the control surface to command is not instantaneous. The response of the control surface actuator also known as the control surface response can be modelled accurately using a first order transfer function as shown below:

$$\dot{\boldsymbol{U}} = \frac{1}{Ts+1}(\boldsymbol{U}_{comm} - \boldsymbol{U}), \tag{3.39}$$

where $\boldsymbol{U}$ is the vector of control surface deflection, $\boldsymbol{U}_{comm}$ is the vector of commanded surface deflection and t is the time constant.

3.3 NASA GTM Matlab Simulink Model

As part of the NASA Aviation Safety Program's Integrated Resilient Aircraft Control Project a simulation model of the NASA GTM was developed using the aerodynamic model which was determined using wind tunnel tests. This simulation model is used to perform simulation tests of flight control algorithms before they are cleared to be applied on the actual NASA GTM UAV. The NASA GTM simulation developed into one of the best general transport aircraft simulations and is provided to the public by NASA for research use. Figure 3.7 is a screenshot of the top level of the NASA GTM Simulink model.

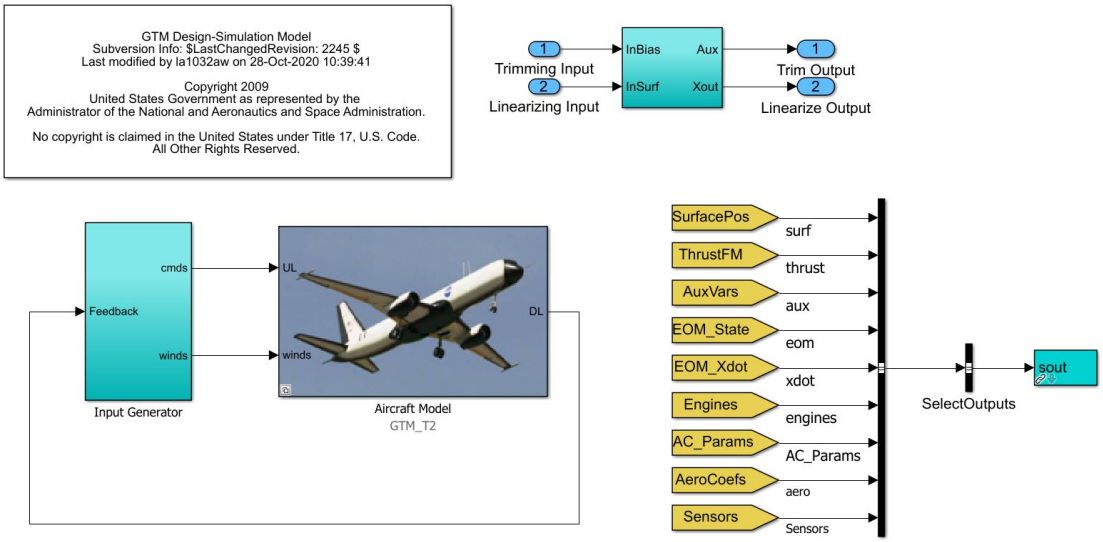

Figure 3.7: Simulink model of the NASA GTM.

The wide-envelope aircraft dynamics model which was described in a previous section is implemented in the Aircraft Model block. The Input Generator block is provided as a sandbox where custom flight control algorithms are to be implemented. The Aircraft Model block includes in depth models of the aircraft dynamics, the wide-envelope aerodynamics, the engines, the onboard sensors, and the control surface actuators. The onboard sensor model includes measurement noise and sensor bandwidth, and the control surface actuator model includes slew rate limits, saturation limits, and actuator dynamics.

In the NASA GTM models exist for the following actuators; ailerons, elevators, rudders, left and right engine throttles, spoilers, flaps, landing gear, nose wheel steering and brakes. The twin engines of the NASA GTM UAV are also modelled in detail and take into account the following, engine dynamics, engine alignment, throttle to engine RPM curve, engine RPM to thrust curve, and the effect of atmospheric density on engine thrust. The moment arm between the engine and the centre of gravity of the aircraft as well as the gyroscopic torques associated with the angular momentum of the engines are also calculated.

The NASA GTM model includes the following sensor models. Measurements of angle of attack, sideslip angle, dynamic pressure, true airspeed, and altitude are all provided by the air data sensors. Measurements of body angular rates, specific accelerations, attitude angles, aircraft position and inertial velocity are provided by the inertial navigation system and GPS. The aerodynamic forces and moments are modelled using non-linear aerodynamic coefficients which are implemented as multi-dimensional lookup tables.

The first set of lookup tables describe the contributions from static forces and moments as a function of AoA and sideslip angle. The second set of lookup tables describe the contribution of dynamic forces and moments as a function of AoA, sideslip angles, and body angular rates. The third set of lookup tables describe the contribution of control surface forces and moments as a function of AoA, sideslip angle, body angular rates, and deflections of the ailerons, stabiliser, elevator and rudder.

To read the coefficients from these lookup tables for a specific set of parameter values the following functions were developed by [21]: $C_{[\_],static}$) which looks up values from the first set of lookup tables, $C_{[\_],[\_]_{osc}}$) and $C_{[\_],[\_]_{ss}}$) which lookup values of the second set of lookup tables, and $C_{[\_],\delta}$) which looks up values of the third set of lookup tables. By summing the lookup values according to which body axis they contribute towards the following set of equations were generated by [21].

$$
\begin{aligned}
C_X =& C_{X,static}(\alpha,\beta) + \Delta C_{X,\delta}(\alpha,\beta,\delta_E,\delta_A,\delta_R) \\
&+ \Delta C_{X,\hat{q}_{osc}}(\alpha,\hat{q}_{osc}) + \Delta C_{X,\hat{\omega}_{ss}}(\alpha,\beta,\hat{\omega}_{ss})
\end{aligned} \tag{3.40}
$$

$$
\begin{aligned}
C_Y =& C_{Y,static}(\alpha,\beta) + \Delta C_{Y,\delta}(\alpha,\beta,\delta_A,\delta_R) \\
&+ \Delta C_{Y,\hat{p}_{osc}}(\alpha,\hat{p}_{osc}) + \Delta C_{Y,\hat{r}_{osc}}(\alpha,\hat{r}_{osc}) \\
&+ \Delta C_{Y,\hat{\omega}_{ss}}(\alpha,\beta,\hat{\omega}_{ss})
\end{aligned} \tag{3.41}
$$

$$
\begin{aligned}
C_Z =& C_{Z,static}(\alpha,\beta) + \Delta C_{Z,\delta}(\alpha,\beta,\delta_E,\delta_A,\delta_R) \\
&+ \Delta C_{Z,\hat{q}_{osc}}(\alpha,\hat{q}_{osc}) + \Delta C_{Z,\hat{\omega}_{ss}}(\alpha,\beta,\hat{\omega}_{ss})
\end{aligned} \tag{3.42}
$$

$$
\begin{aligned}
C_l =& C_{l,static}(\alpha,\beta) + \Delta C_{l,\delta}(\alpha,\beta,\delta_A,\delta_R) \\
&+ \Delta C_{l,\hat{p}_{osc}}(\alpha,\hat{p}_{osc}) + \Delta C_{l,\hat{r}_{osc}}(\alpha,\hat{r}_{osc}) \\
&+ \Delta C_{l,\hat{\omega}_{ss}}(\alpha,\beta,\hat{\omega}_{ss})
\end{aligned} \tag{3.43}
$$

$$
\begin{aligned}
C_m =& C_{m,static}(\alpha,\beta) + \Delta C_{m,\delta}(\alpha,\beta,\delta_E,\delta_A,\delta_R) \\
&+ \Delta C_{m,\hat{q}_{osc}}(\alpha,\hat{q}_{osc}) + \Delta C_{m,\hat{\omega}_{ss}}(\alpha,\beta,\hat{\omega}_{ss})
\end{aligned} \tag{3.44}
$$

$$
\begin{aligned}
C_n =& C_{n,static}(\alpha,\beta) + \Delta C_{n,\delta}(\alpha,\beta,\delta_A,\delta_R) \\
&+ \Delta C_{n,\hat{p}_{osc}}(\alpha,\hat{p}_{osc}) + \Delta C_{n,\hat{r}_{osc}}(\alpha,\hat{r}_{osc}) \\
&+ \Delta C_{n,\hat{\omega}_{ss}}(\alpha,\beta,\hat{\omega}_{ss})
\end{aligned} \tag{3.45}
$$

The first three equations calculate the sum of the aerodynamic coefficients in the X, Y, Z body axis directions. The last three equations calculate the sum of the aerodynamic coefficients in the l, m, n body axis moment rotations. These six equations directly link to the equations 3.21 to 3.26 as noted in the previous section Mathematical General Flight Dynamics Model of a Fixed-Wing Aircraft.

3.4 Modelling Deep Stall and Spin

The NASA GTM does not present any deep stall behaviour and has a very unstable spin state. As previously explained, deep stall is entered once the aircraft stalls and its AoA is large enough to submerge the tail plane in the wake of the stalled main wings. In this state the aircraft should settle at a high AoA and that any application of downwards elevator action should not be able to generate enough downwards pitching moment to recovery from the stall. At this high AoA the rolling and yawing moments must be small enough as to prevent the aircraft from rolling naturally out of the deep stall.

To model spin this rolling moment and yawing moment are required to reach the high angular rates experienced in a spin. The aircraft should also experience a high AoA during a spin as well as a constant sideslip angle. An attempt was made with the unmodified NASA GTM to either enter the aircraft into a deep stall or spin by negatively deflecting the elevator.

In first Figure 3.8 the AoA (α), sideslip angle (β), and control deflections are plotted against time. In the second Figure 3.8 the angular rates: roll (P), pitch (Q), and yaw (R) rates are plotted against time. The elevator is deflected to ($\delta_E = -30°$) at time ($t = 1s$) and held constant for 5 seconds after which it is returned to the trim deflection. This negative elevator deflection generates a positive pitching moment which increases the NASA GTM's pitch rate in the positive direction. This in turn increases the AoA of the aircraft up to ($\alpha = 30°$) and then settles at around ($\alpha = 25°$).

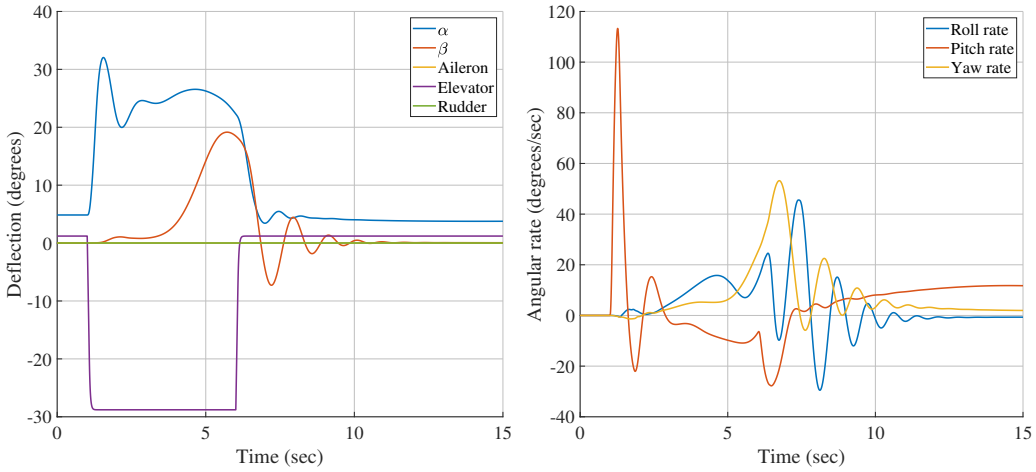

Figure 3.8: Negative elevator deflection applied to the unmodified NASA GTM.

When the elevator deflection is returned to trim condition the AoA also returns to the trim AoA of around ($\alpha = 4.6°$). The NASA GTM therefore did not enter into a deep stall. The angular rates of the NASA GTM increased with the elevator deflection but also returned to close to ($0°/s$) after the elevator is returned to trim deflection and therefore the NASA GTM also did not enter into a stable spin.

3.4.1 Deep Stall

To model deep stall dynamics with the NASA GTM it was decided to modify the following aerodynamic coefficients.

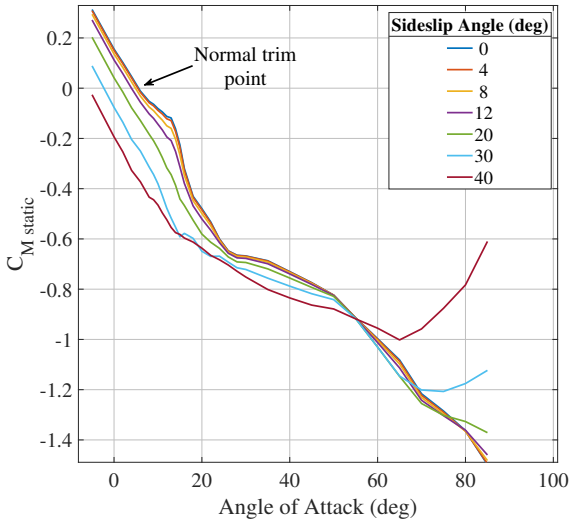

Figure 3.9: Static pitching moment curve of the unmodified NASA GTM

The unmodified static pitching moment lookup table as shown in Figure 3.9 is responsible for the pitching moment experience at different AoA and sideslip angles. In the unmodified lookup table the static pitching moment decreases as the AoA increases. A negative static pitching moment will pitch the nose of the aircraft down and thereby reduce the AoA. A positive pitching moment will pitch the nose of the aircraft up and thereby increase the AoA. When the static pitching moment is zero as can be seen when the AoA is around ($\alpha = 5°$) the aircraft will neither pitch up nor down and therefore be in a stable state.

This AoA is known as the trim AoA. In Figure 3.8 the elevator deflection increased the AoA of the aircraft. At this larger AoA the aircraft experiences a negative static pitching moment which then decreases the AoA of the aircraft back to the trim AoA. The NASA GTM does therefore not depict any deep stall dynamics in its unmodified state. To model deep stall it is required that the aircraft settles at a high AoA once it passes a critical AoA. To model this the following proposed modifications are applied. The aerodynamic model of the NASA GTM was modified to exhibit deep stall behaviour based on the information provided in the article "Study of Deep Stall Characteristics and Longitudinal Special Phenomena of T-Tail Aircraft" by Wang and Shi [29].

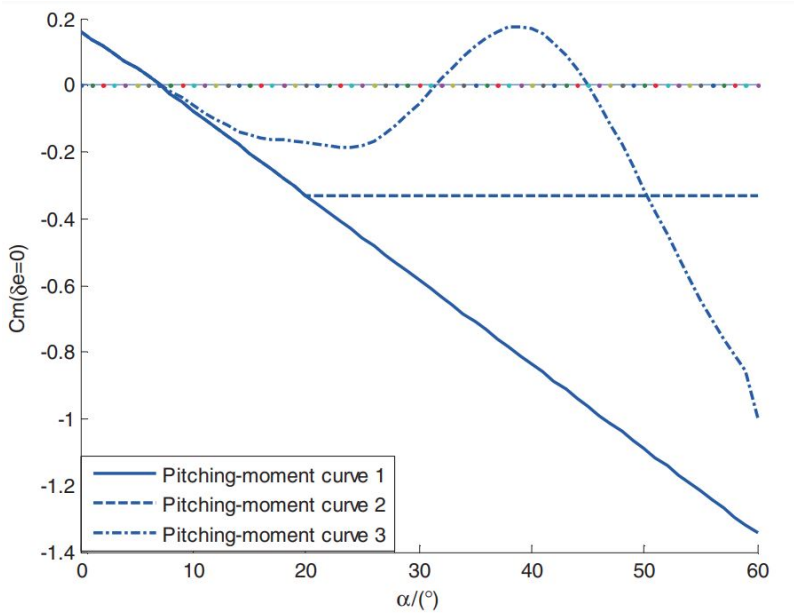

Figure 3.10: Pitching moment curve for three different aircraft configurations [30].

Wang and Shi explain that for aircraft which do not experience deep stall the pitching moment curve is always negative as the AoA increases. For aircraft which do experience deep stall this is not the case. As can be seen in Figure 3.10 the pitching moment curve for the third aircraft configuration does not remain negative as the AoA increase but increase and becomes positive at an AoA of ($\alpha = 32°$). As the AoA is increased further a maximum positive pitching moment is reached at an AoA of ($\alpha = 40°$) where after the pitching moment curve decreases and becomes negative at an AoA past ($\alpha = 47°$). The third pitching moment curve crosses the zero line at three different points.

The first point as explained previously is the normal aircraft trim point which in this Figure is at an AoA of about ($\alpha = 7°$). By increasing the AoA slightly the pitching moment curve becomes negative and this results in a negative pitching moment which decreases the AoA and returns the aircraft to the trim AoA. By decreasing the AoA slightly the pitching moment curve becomes positive which results in a positive pitching moment which increases the AoA and returns the aircraft to the trim AoA. This is therefore a stable equilibrium point as any deviation from it will result in an action which will restore the system to the equilibrium point. The second point is at an AoA of ($\alpha = 32°$). Following the same reasoning as before if the AoA is decreased from this point the pitching moment curve becomes negative which results in a negative pitching moment. This negative pitching moment decreases the AoA further and drives the system down to the trim AoA equilibrium point. By increasing the AoA from the second point the pitching moment curve becomes positive. This results in a positive pitching moment and drives the system to a higher

AoA. If the system is kept at the second point a zero pitching moment is applied to the system and the system remains at that AoA as it is in equilibrium. The second point is therefore an unstable equilibrium point.The third point is an AoA of ($\alpha = 47°$). This point is similar to the first in that it is a stable equilibrium point. Any small deviation from this AoA results in an action which returns the aircraft to this equilibrium point. If the aircraft is not capable of generating a large enough AoA deviation to reduce its AoA below the second point it will return the the third equilibrium point. This is known as the deep stall point.

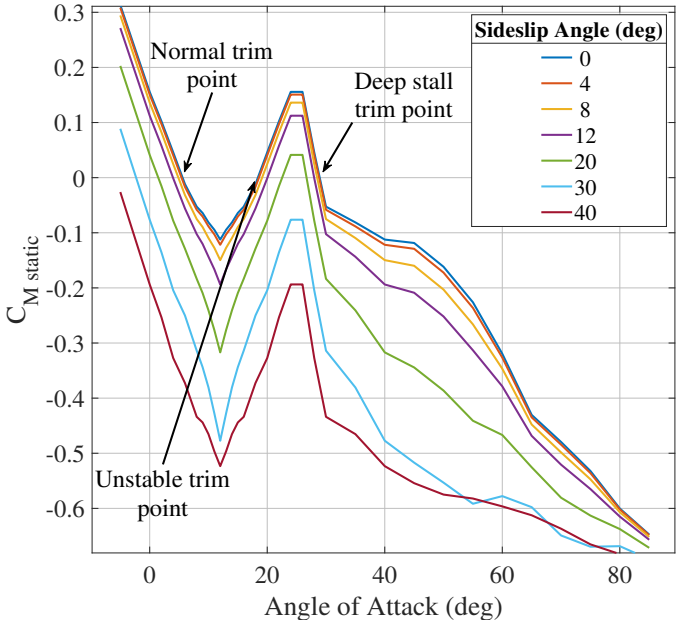

Figure 3.11: Static pitching moment curve of the modified NASA GTM

To model deep stall with the NASA GTM the static pitching moment coefficient $C_{m,\text{static}}(\alpha, \beta))$ was modified with respect to AoA and sideslip angle. The static pitching moment coefficient was modified as shown in Fig. 3.11 to have three equilibrium points at AoA of ($\alpha = [6°$, $20°$,$28°]$), where the static pitching moment curve is equal to ($C_{m,\text{static}}(\alpha, \beta = 0) = 0$) for the same elevator deflection.

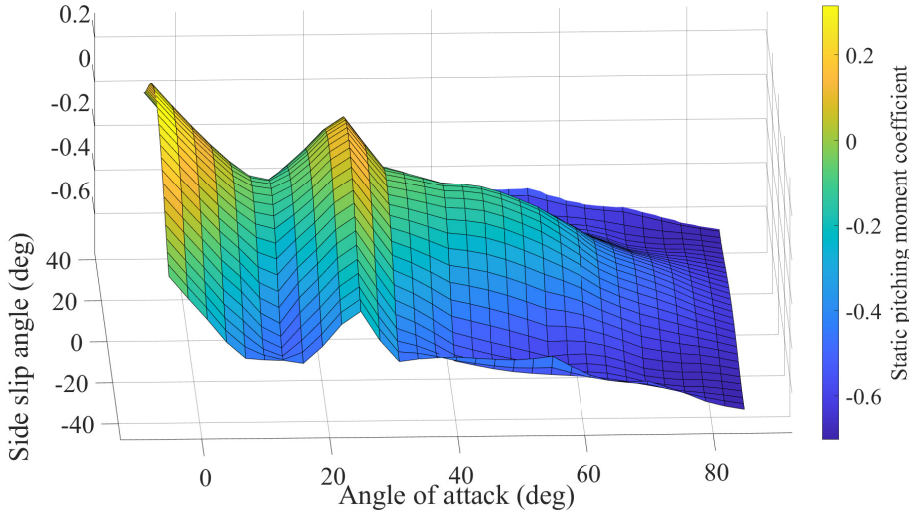

Figure 3.12: Static pitching moment curve of the modified NASA GTM

These changes are made to be inline with what was observed by Wang and Shi. In Figure 3.13 the modified NASA GTM is stalled using a negative elevator deflection.

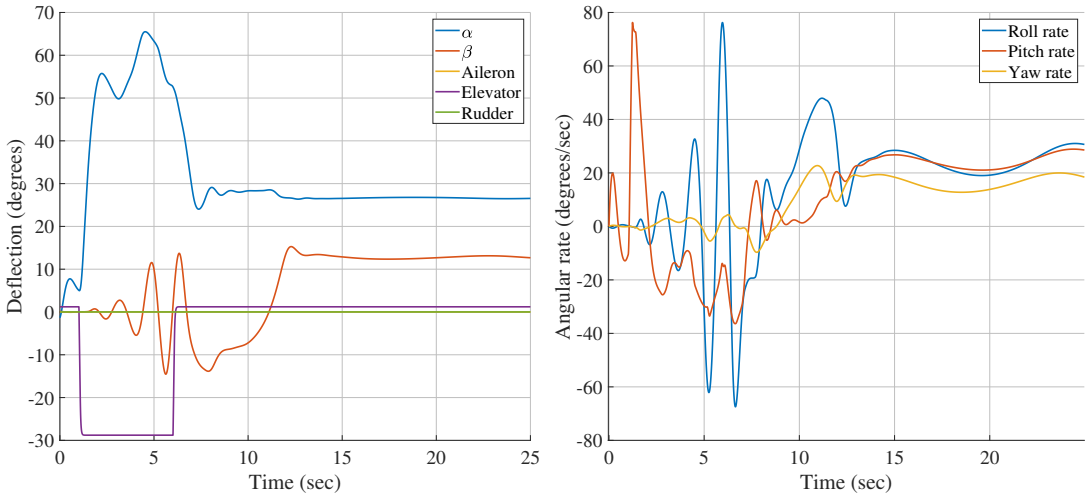

Figure 3.13: Negative elevator deflection applied to the modified NASA GTM.

In first Figure 3.8 the AoA (α), sideslip angle (β), and control deflections are plotted against time. In the second Figure 3.8 the angular rates: roll (P), pitch (Q), and yaw (R) rates are plotted against time. The elevator is deflected to ($\delta_E = -30°$) at time ($t = 1s$) and held constant for 5 seconds after which it is returned to the trim deflection. This negative elevator deflection generates a positive pitching moment which increases the NASA GTM's pitch rate in the positive direction. This in turn increases the AoA of the aircraft up to ($\alpha = 30°$) and then settles at around ($\alpha = 25°$). When the elevator deflection is returned to trim deflection the AoA does not return to the trim AoA but settles at the high AoA of ($\alpha = 27°$). This is inline with the modifications which were applied to the static pitching moment coefficient. However, this modification does not fully capture deep stall dynamics as the sideslip angle does not return to zero but settles at ($\beta = +12°$) and the angular rates settle at ($P, Q, E > 20°/s$). To counteract this rotational dynamics the following aerodynamic lookup tables were modified. The static yawing moment coefficient $C_{n,\text{static}}(\alpha, \beta)$) was modified with respect to AoA and sideslip angle. In Figure 3.14 the unmodified static yawing moment curves are presented.

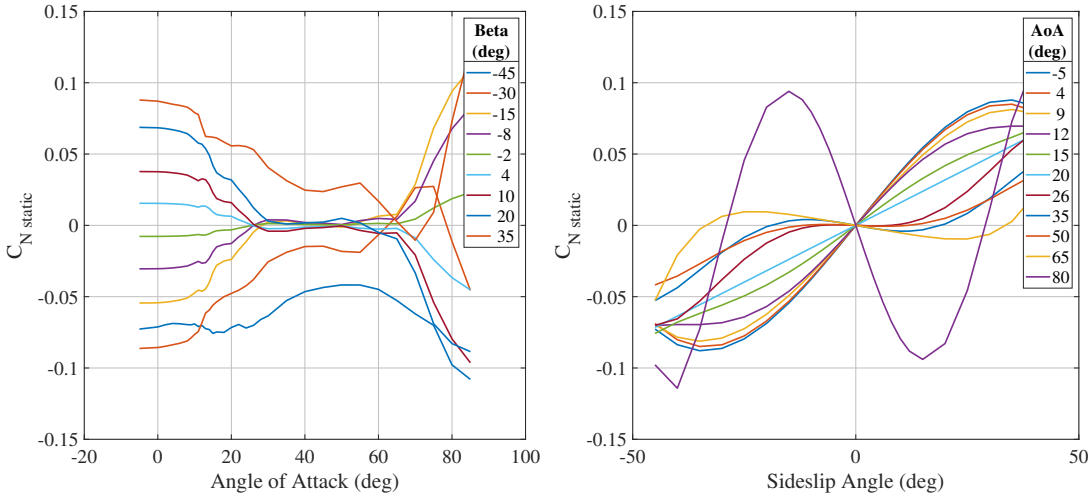

Figure 3.14: Static yawing moment curve of the unmodified NASA GTM

To reduce the destabilising yawing moment seen at higher AoA it was decided to set the yawing moment curve for all AoA to the yawing moment curve of the trim AoA. This change can be seen in the left hand figures of Figures 3.14 and Figures 3.15. It is assumed that at the trim AoA ($\alpha = 5°$) the aircraft has good stabilising properties and this would help stabilise the aircraft at high AoA ($\alpha > 10°$) as well.

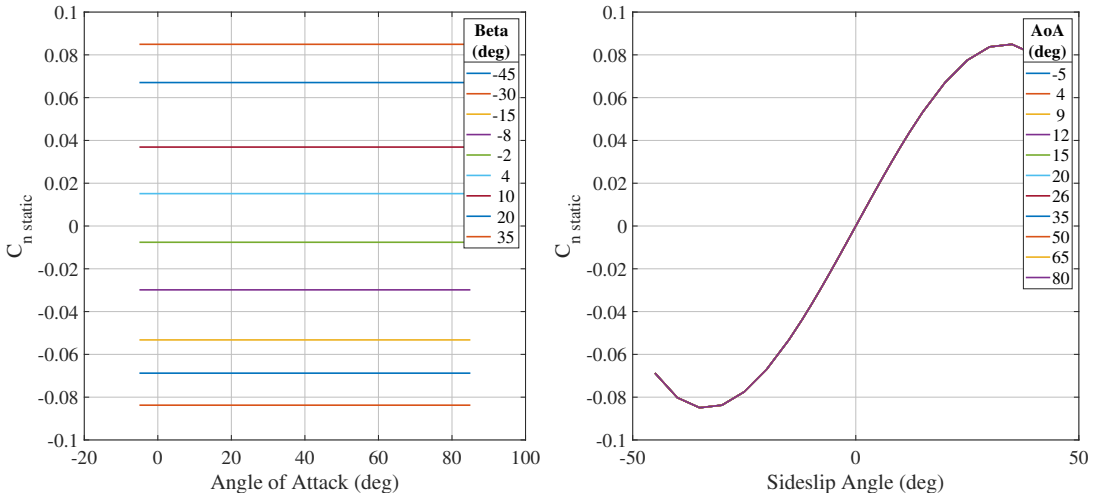

Figure 3.15: Static yawing moment curve of the modified NASA GTM

The static rolling moment coefficient $C_{l,\text{static}}(\alpha, \beta))$ was modified with respect to AoA and sideslip angle. In Figure 3.16 the unmodified static rolling moment curves are presented.

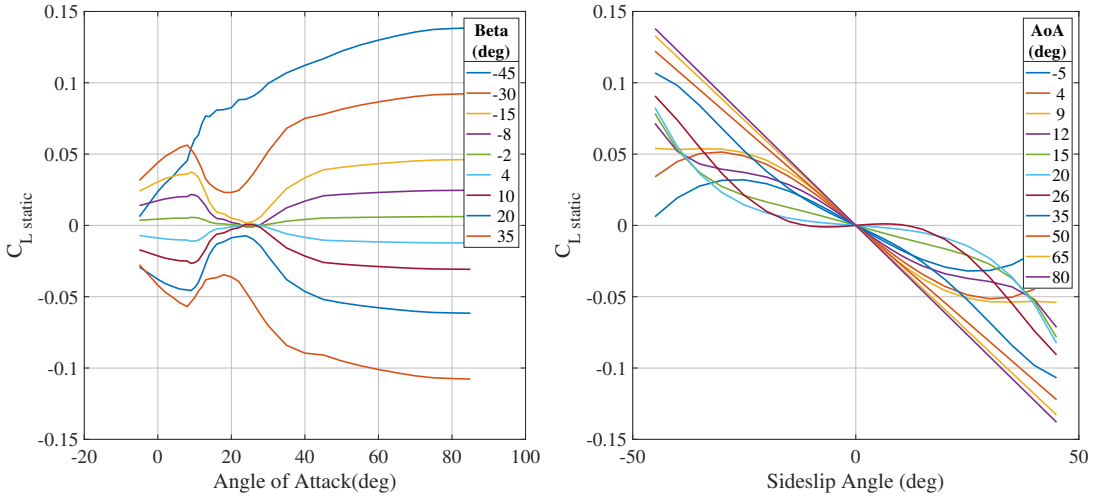

Figure 3.16: Static rolling moment curve of the unmodified NASA GTM

To also reduce the destabilising rolling moment at higher AoA the same approach is used as for the yawing moment coefficient curves. The rolling moment curve for all AoA is set to the rolling moment curve of the trim AoA.

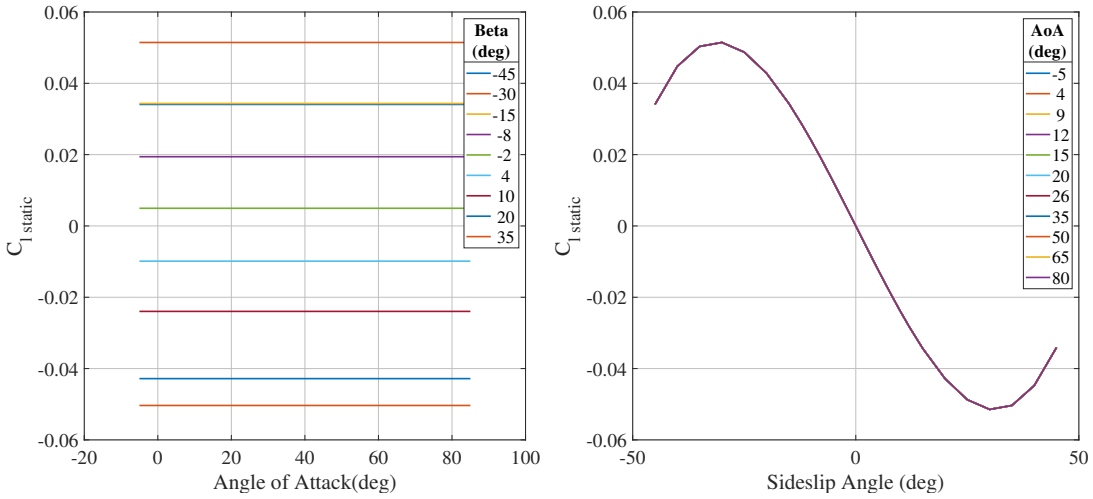

Figure 3.17: Static rolling moment curve of the modified NASA GTM

With these stabilising modifications in place another test was performed to observe if the yawing and rolling moment as well as the sideslip deflection has been reduced for the deep stall AoA.

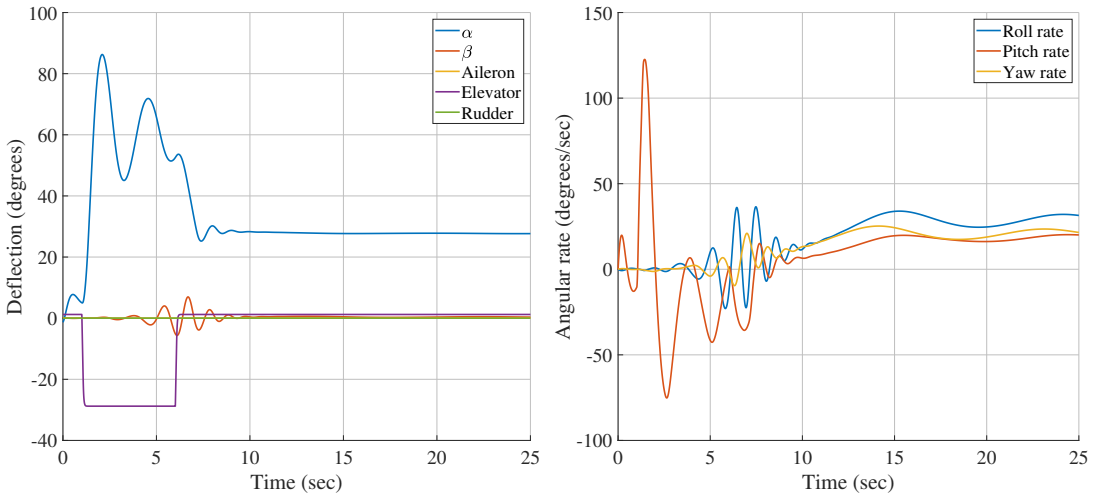

Figure 3.18: Negative elevator deflection applied to deep stall modified NASA GTM model.

In Figure 3.18 it is observed that the angular rates are not completely damped. The sideslip angle however is well damped and settles at a very low sideslip angle of ($\beta = 1°$). This is an improvement as compared to Figure 3.13 which saw a large sideslip deflection of ($\beta = 12°$) when in deep stall.

Elevator Control Authority

Once in deep stall it has been noted by [4] that the effectiveness of the elevator control surface to generate a downwards pitching moment is greatly reduced to the point that it is not possible to recover the aircraft with just a maximum constant positive elevator deflection. This is due to the tail control surfaces being submerged by the wake of stall air coming off the stalled main wings. The incremental pitching moment coefficient describes the effectiveness of the elevator control surface in generating a pitching moment. The modification to the NASA GTM allows it to be forced into deep stall using a negative

elevator deflection. In Figure 3.19 the NASA GTM is forced into deep stall and a positive elevator deflection is applied.

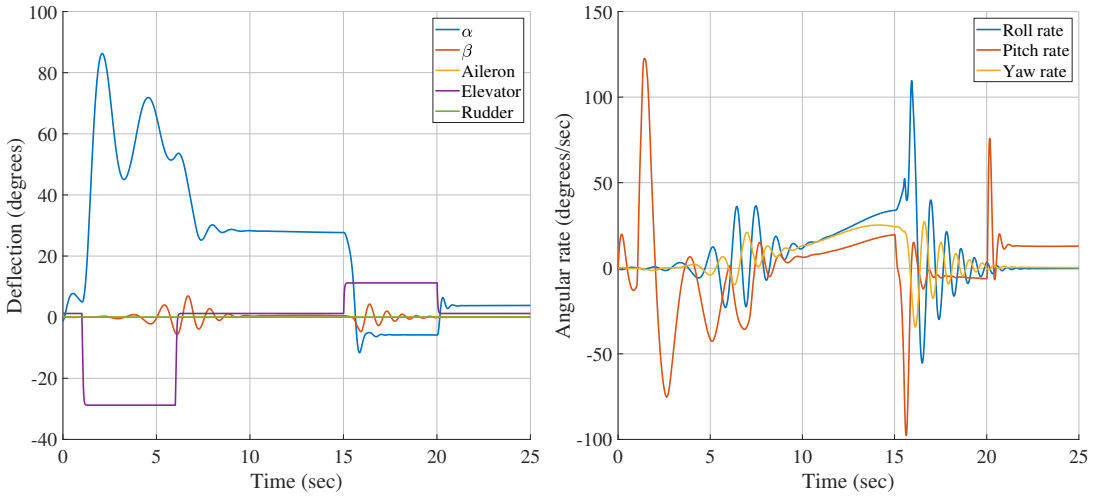

Figure 3.19: Positive elevator deflection applied while in deep stall.

This positive elevator deflection generates a downwards pitching moment and recovers the aircraft from the deep stall. This was therefore an incomplete modelling of deep stall and it was required to modify the incremental pitching moment coefficient. The incremental pitching moment coefficient with respect to elevator deflection was modified as shown in Fig. 3.20 so that the elevator loses pitching moment effectiveness at AoA ($11° < \alpha < 35°$) and sideslip angles ($-5° < \beta < 5°$). The modification to ($\Delta C_{m,\delta}(\alpha, \beta, \ldots, \delta_E)$) represents the aerodynamics which cause the elevator to lose effectiveness when it is in the aircraft's wake at high AoA and close to zero sideslip angle. The elevator regains effectiveness when the sideslip angle is deviated away from zero in either the positive or negative direction or when the AoA is deviated above or below the deep stall AoA ($\alpha = 28°$).

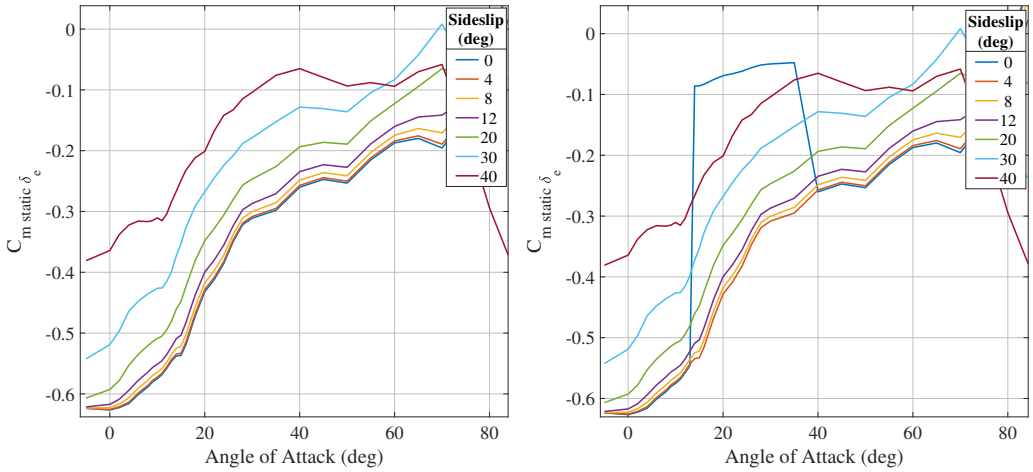

Figure 3.20: The unmodified and modified NASA GTM incremental pitching moment coefficient with respect to elevator.

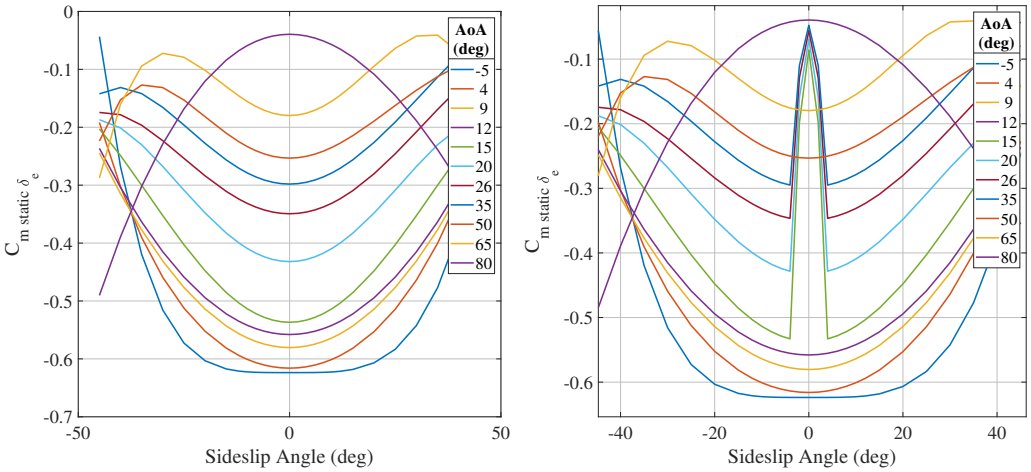

Figure 3.21: The unmodified and modified NASA GTM incremental pitching moment coefficient with respect to elevator.

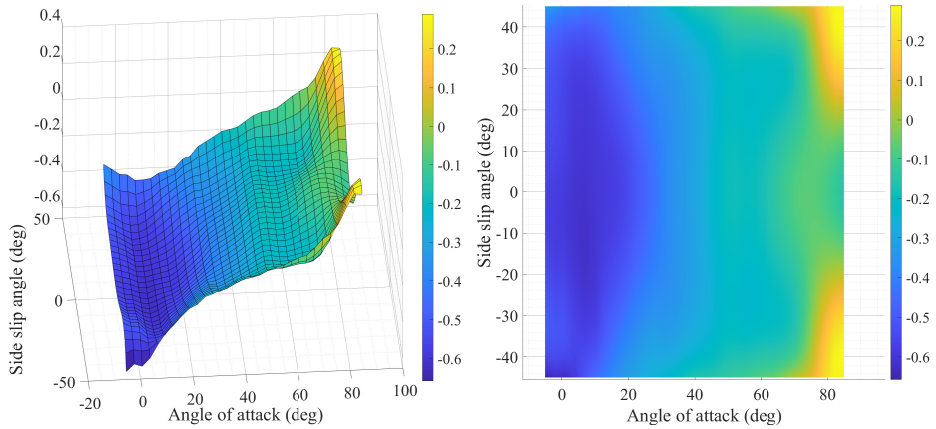

(a) Unmodified

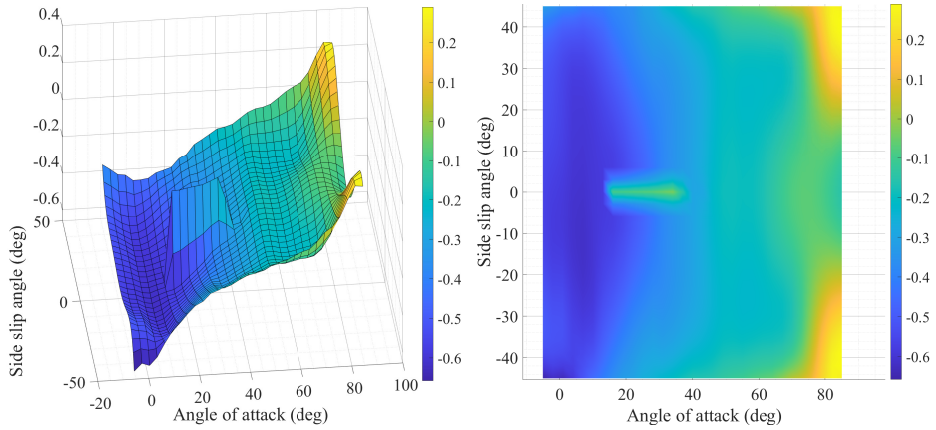

(b) Modified

Figure 3.22: 3D representation of the NASA GTM incremental pitching moment coefficient with respect to elevator.

The modification to the incremental pitching moment coefficient can be seen for sideslip angles around zero ($-5 < \beta < 5$) and for AoA ($11° < \alpha < 35°$). This area of AoA and

sideslip angle represents the wind axes rotation for which the wake of the main wings will wash over the elevator and rudder control surfaces. Due to the rudder also being submerged by the stalled air coming off the main wing it was decided to reduce the effectiveness of the rudder control surface in generating an incremental yawing moment at sideslip angles close to zero and at deep stall AoA. In Figure 3.23 the modification to the incremental yawing moment coefficient can be seen for sideslip angles around zero ($-5 < \beta < 5$) and for AoA ($11° < \alpha < 35°$).

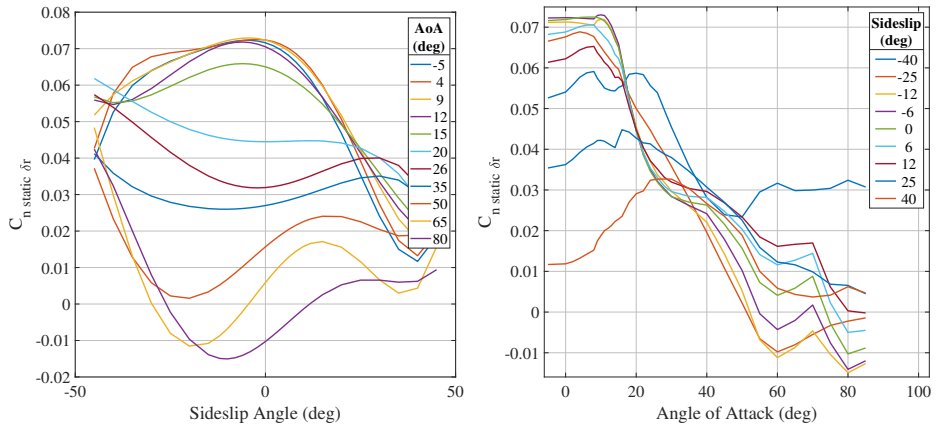

(a) Unmodified

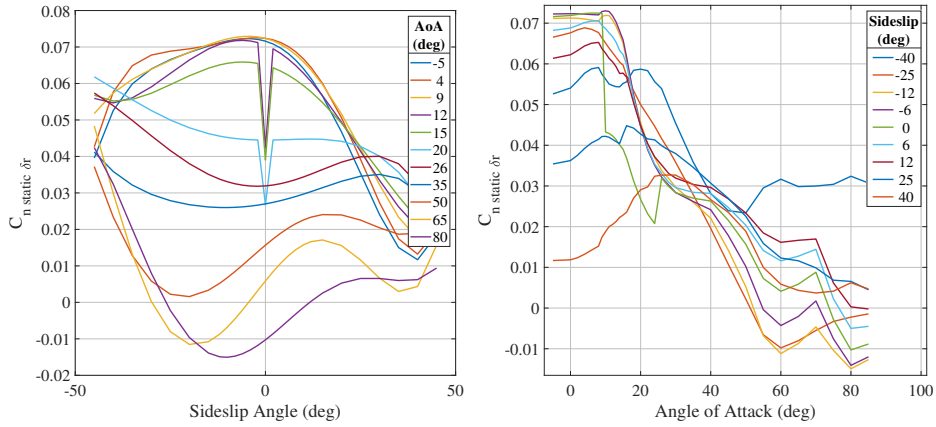

(b) Modified

Figure 3.23: The NASA GTM incremental yawing moment coefficient with respect to rudder, modified to lose effectiveness in the aircraft's wake.

A simulation was performed to show that the modified NASA GTM model can be pushed into deep stall, and cannot be recovered by elevator actions only. The simulation results are shown in Figure 3.24 and 3.25. The time histories of the AoA, sideslip angle, aileron, elevator, and rudder are shown in Figure 3.24. The aircraft starts the simulation in normal flight with an AoA of ($\alpha = 5°$) and all the control surfaces set to their trim deflections. At ($t = 1s$), a nose-up elevator deflection of ($\delta_E = 30°$) is commanded, and the aircraft is pushed into deep stall. The AoA increases from ($\alpha = 6°$) to ($\alpha = 55°$), while the sideslip angle remains near zero ($\beta = +- 0°$). At ($t = 6s$), the elevator is returned to its trim deflection, but the aircraft remains at a high AoA. A transient is observed in the AoA due to the flight path angle decreasing because of the loss of lift in deep stall.

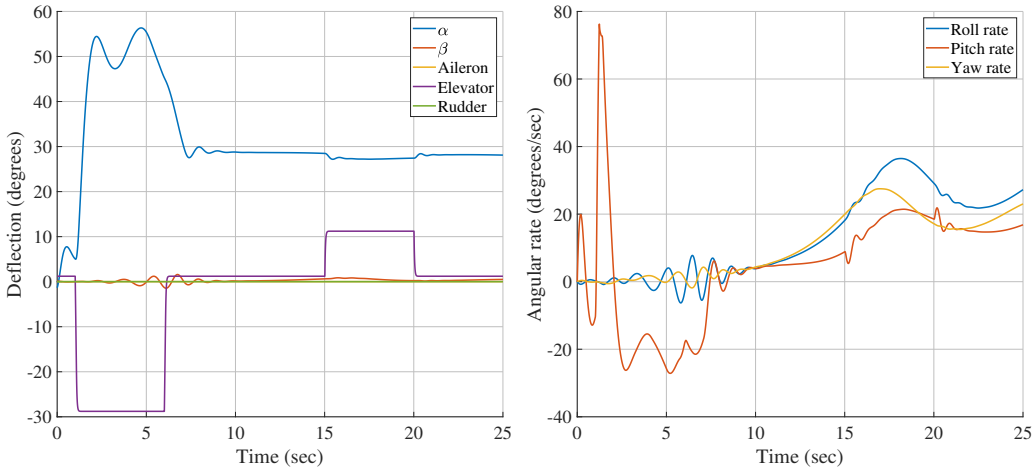

Figure 3.24: Positive elevator deflection applied while in deep stall with modified incremental pitching moment coefficient.

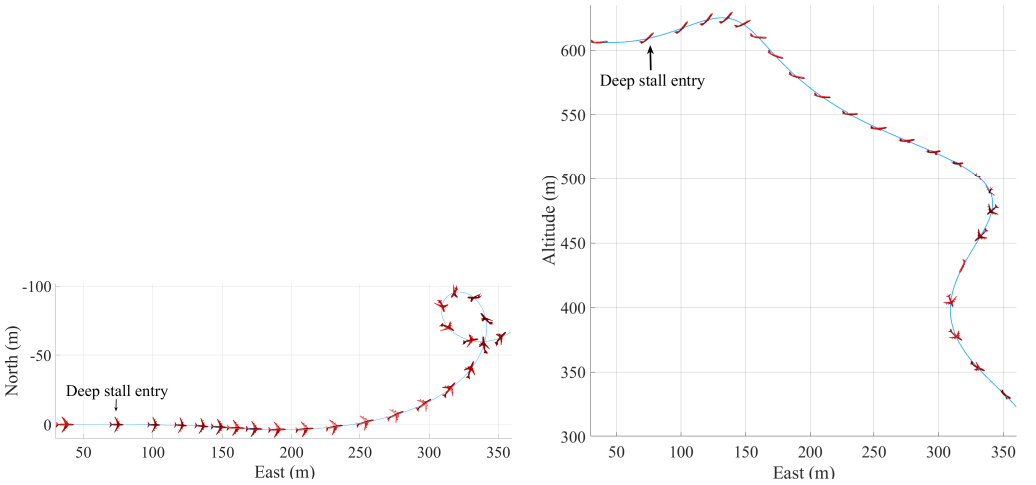

Figure 3.25: The aircraft's trajectory (top view and side view) for the simulated deep stall entry and attempted recovery using elevator only.

Eventually, the AoA settles at the stable deep stall AoA of ($\alpha = 28°$). After ($t = 10s$), an attempt is made to recover the aircraft from deep stall using elevator action only. A nose-down elevator deflection of ($\delta_E = +10°$) is commanded, but due to the loss of elevator effectiveness, the aircraft remains trapped in deep stall. Fig. 3.25 shows the aircraft's trajectory for the simulated deep stall entry and attempted recovery. The aircraft enters deep stall and then continues to enter a spiral motion while still being locked in at a high AoA of a deep stall. This concludes the modelling of deep stall using the NASA GTM. In the next section the unmodified NASA GTM will be modified to model spin behaviour.

3.4.2 Spin

In a spin the aircraft rotates about a vertical axis with the inner-wing being in a stalled state while the outer-wing still generates lift. An aircraft may enter a spin if the pilot causes the aircraft to enter a cross-control stall while performing a skidding uncoordinated turn. An aircraft spin has four consecutive phases: spin entry, incipient spin, developed spin, and spin recovery. In a developed spin the aircraft's angular rotation rate, airspeed and vertical speed can either stabilise or oscillate around a point. The flight path of the aircraft is vertical or near vertical downwards. To model spin is highly complex as the states of the aircraft in a spin are dynamic yet stable. The angular rates, AoA, sideslip angle and control surface deflections as well as aircraft airspeed are all strongly coupled while an aircraft is in a spin. Khrabrov, Sidoryuk, and Goman present in [17] (2013) their development of an aerodynamic model of a generic airliner configuration for a wide range of AoA, sideslip angles and angular rates. An investigation into the spin modes of the model revealed that by simultaneously deflecting the elevator control surface to the maximum negative deflection ($\delta_E = -30°$) as well as deflecting the rudder control surface to either its positive or negative deflection ($\delta_r = +/-30°$) resulted in the aerodynamic model of the airliner entering into a spin condition. Free-spin tests were performed in the TsAGI vertical wind tunnel and these experimental results are in agreement with the results from the developed aerodynamic model.

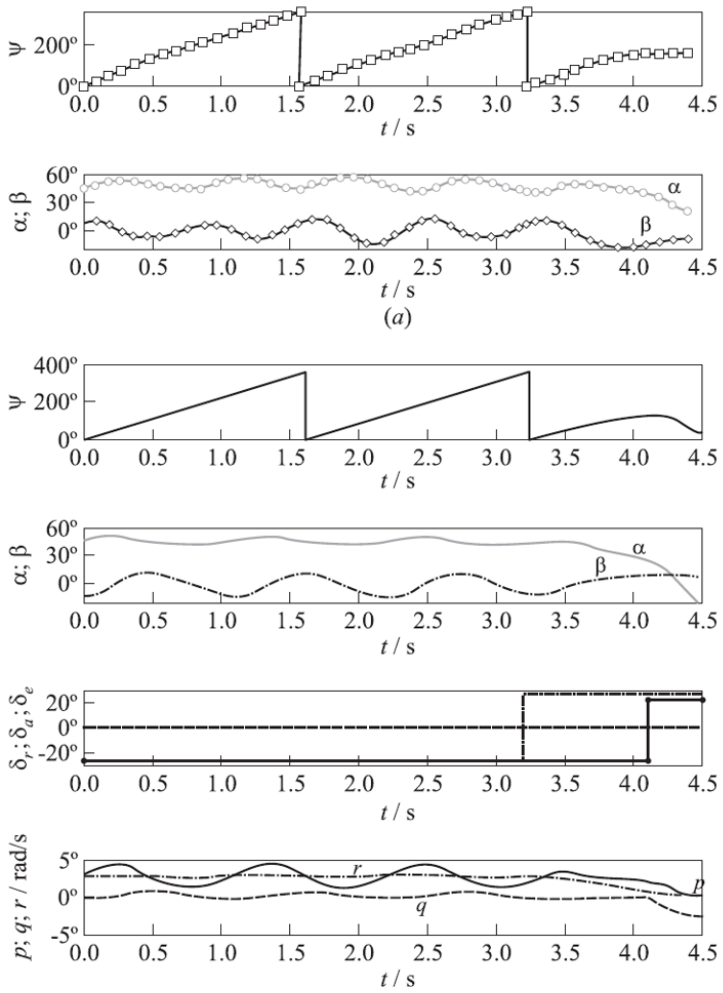

Figure 3.26: Figure 8 from [17]: Comparison of experimental (a) and computational (b) time histories for motion parameters in oscillatory spin and spin recovery control.

In Figure 3.26 the time histories of different motion parameters in an oscillatory spin are presented. This motion is excited in the airliner aerodynamic model by the negative elevator and rudder deflection as can be seen in the fifth graph. A large positive AoA around ($\alpha = 45°$) and an oscillatory sideslip angle with magnitude of ($15°$) and mean of ($0°$) is observed in the second and fourth graph. The computational and experimental results are very closely matched and shows that the computational model captures the dynamics of spin accurately. Bunge and Kroo present in [3] (2018) their development of and automatic spin recovery algorithm with focus on minimal altitude loss. An aerodynamic model which presents spin dynamics was also developed and used to verify the performance of the automatic spin recovery algorithm.

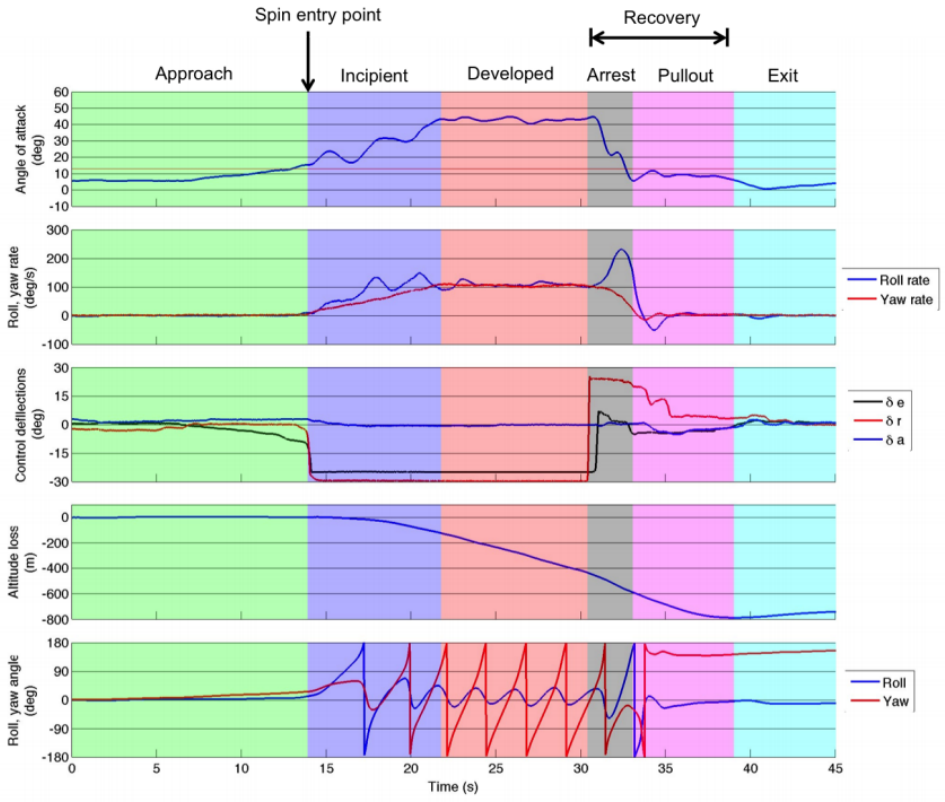

Figure 3.27: Phases of a typical spin by Bunge and Kroo in their paper 'Automatic Spin Recovery with Minimal Altitude Loss' (2018). [3]

In Figure 3.27 the AoA increases to around ($\alpha = 40°$) and roll and yaw rates increase to close to ($100°/s$). Similar elevator and rudder control actions were used to enter and sustain the spin as shown in Figure 3.26 by KhRabrov and Goman. To determine the spin behaviour of the NASA GTM the same control actions are applied in Figure 3.28. With the negative elevator deflection a positive pitching moment is generated and the AoA increases to a mean of ($+38°$). The AoA oscillates around this point with an amplitude of ($12°$). The sideslip angle oscillates around ($-5°$) with an amplitude of ($20°$). The roll rates increase on average to about ($+200°/s$) and oscillates with a magnitude of ($150°/s$). The pitch rate initially increases but then returns to ($0°$) with oscillations of ($40 - 50°/s$). The yaw rate is the most stable at around ($130°/s$) while oscillating with amplitude of ($40°/s$).

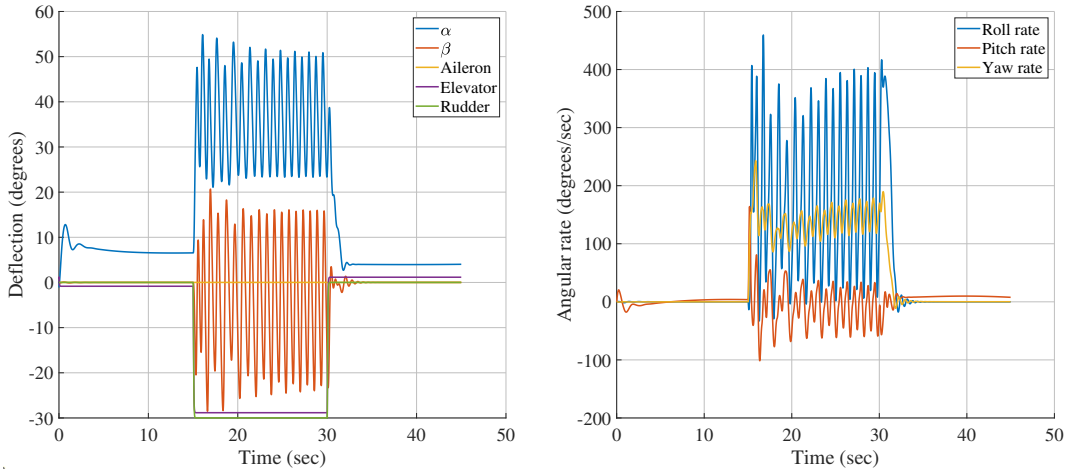

(a) (b)

Figure 3.28: Excitation of spin behaviour using ($\delta_E = -30°$) elevator and ($\delta_r = -30°$) rudder deflection on the unmodified NASA GTM.

These oscillations show that there is an strong form of coupling between the static angular rate coefficients and the dynamic actuator coefficients. In [17] the coefficients used to model spin are the; longitudinal, normal, and lateral velocity coefficients as well as the roll, pitch and yaw rate coefficients. From Section 3.2.6 which covers the 6DoF equations of motion it is noted that these are the full 6DoF coefficients which shows that the dynamics of spin are both translational and rotational. In the conference proceedings of [24] (2013) by Paranjape, Gill, Ananthkrishnan and Lowenberg preformed an analytical assessment of the spin susceptibility of the NASA GTM. A criterion was developed to predicted the spin susceptibility of an aircraft design and was matched with the predictions made using bifurcation analysis and traditional departure criteria. Stable oscillatory spins were achieved with the NASA GTM simulation by applying full negative elevator deflection and holding the rudder and aileron deflections close to zero.

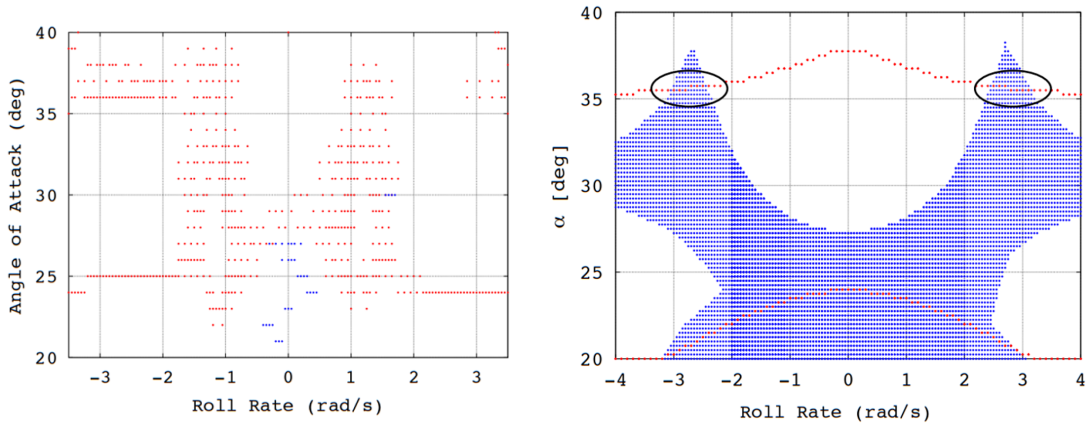

Figure 3.29: Plot showing the accessible region (blue) and the saddle node bifurcations (red) in the AOA (α) vs. Roll rate (p) parameter space. Black ellipses are used to identify accessible incipient spin solutions. (SNBs). (Figure 4 from [24])

Figure 3.29 shows the results of the analysis by [24]. The dynamic region which results

in an oscillatory spin is marked by the two ellipsoids one being a right spin and the other a left spin. The time histories of the parameters in Figure 3.28 represents the spin which would occur at the right most ellipsoid in Figure 3.29 b. Another spin region exists between ($20°<\alpha<25°$) and along the red line which marks a saddle node. This spin is achieved by only deflecting the elevator to ($\delta_E = -30°$) and holding the rudder at ($\delta_r = +5°$) deflection and is presented in Figure 3.30.

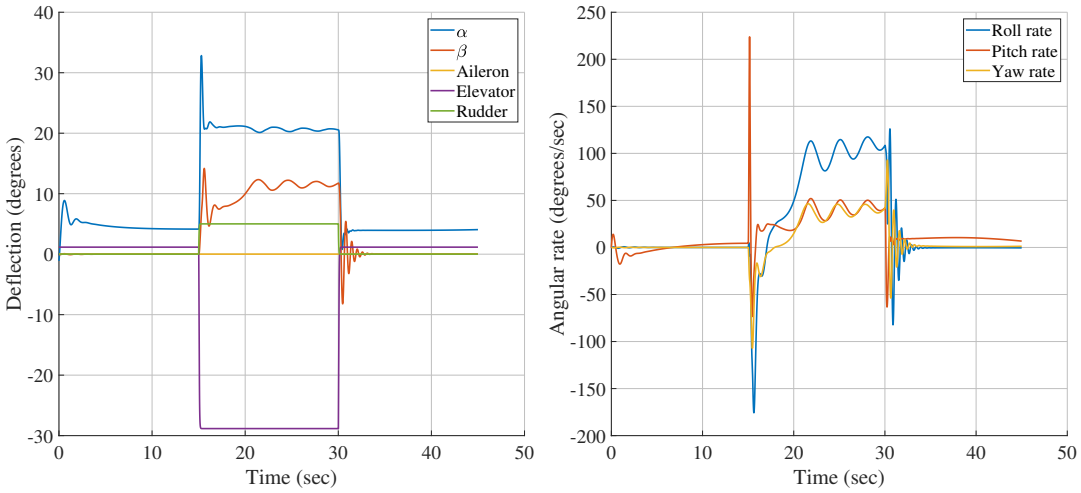

Figure 3.30: Excitation of spin behaviour using an elevator deflection of ($\delta_E = -30°$) and a rudder deflection of ($\delta_r = +5°$) applied to the unmodified NASA GTM.

In Figures 3.30 the NASA GTM is initialised in a wings level trim flight. A negative elevator deflection of ($\delta_E = -30°$) and a positive rudder deflection of ($\delta_r = +5°$) is applied to the NASA GTM simulation at time ($t = 15s$). The AoA then increases to ($\alpha = 21°$) and the sideslip angle increases to ($\beta = 12°$). A large positive spike in the pitch rate is observed as the elevator deflection is applied at time ($t = 15s$) and a negative spike follows as the aircraft settles at the high AoA ($\alpha = 20°$). The pitch rate gradually increases to ($q = 45°/s$) as the control surfaces are held constant. A negative spike is observed for the roll and yaw rate as the elevator and rudder deflections are applied and then increase to ($p = 100°/s$) and ($r = 45°/s$) respectively as the control surfaces are held constant. At time ($t = 30s$) the elevator and rudder control surface deflections are returned to ($\delta_E = 0°$) and ($\delta_r = 0°$). All the aircraft parameters return to their original trim values with a large amount of oscillation. The NASA GTM therefore does present spin dynamics as shown by [24] and reproduced in Figures 3.28 and 3.30. A high AoA ($\alpha = 38°$) spin can be achieved by applying full negative elevator deflection ($\delta_E = -30°$) and by applying either full negative or full positive rudder deflection ($\delta_r = +/-30°$). An AoA ($\alpha = 21°$) spin can be achieved by applying full negative elevator deflection ($\delta_E = -30°$) and by applying either a small negative or a small positive rudder deflection ($\delta_r = +/-5°$). However, when the elevator and rudder controls are returned to neutral then the NASA GTM recovers from the spin naturally and without any control input. This can be seen in Figures 3.30 and 3.28 at time ($t = 30s$) where the AoA, sideslip angle and roll, pitch and yaw rate return to normal flight states once the elevator and rudder control surfaces are returned to ($\delta_E = 0°$) and ($\delta_r = 0°$). The NASA GTM therefore does not present a self sustaining spin in its unmodified state.

3.4.3 NASA GTM Spin Modifications

For this project it would be of interest to have an aerodynamic model that presents a self sustaining spin. Depending on the aerodynamic model of an aircraft a sustained spin can have a range of different stable AoA states. It is therefore proposed to modify the static pitching moment coefficient table of the NASA GTM aerodynamic model using a similar approach to that of the deep stall trim state.

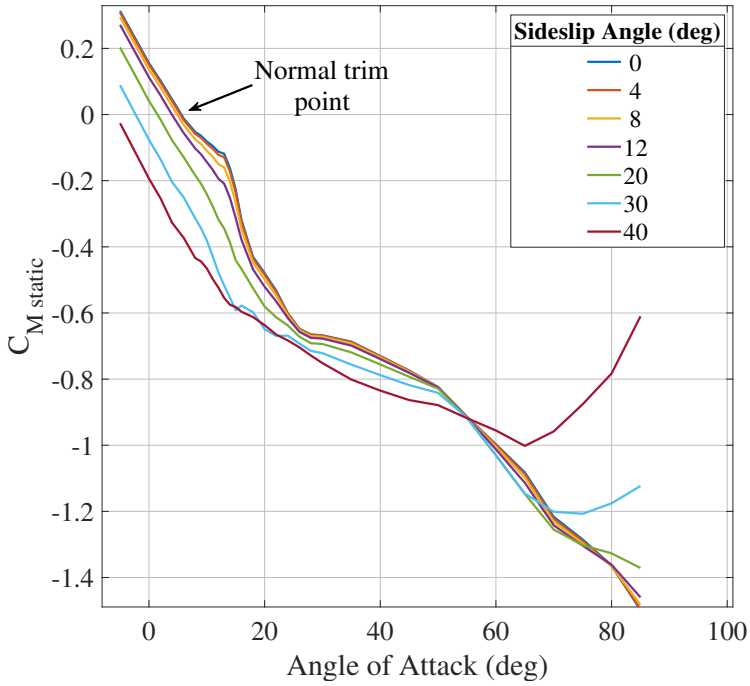

(a) Before modifications.

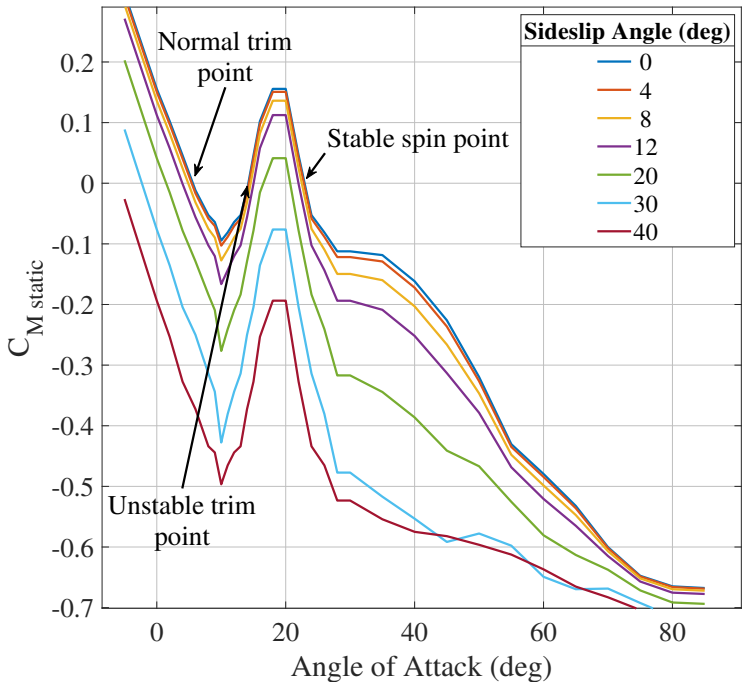

(b) After modifications.

Figure 3.31: Spin modifications to the NASA GTM Static Pitching Moment Coefficient.

The static pitching moment coefficient as seen in Figure 3.31b has three equilibrium points, the normal wings level flight trim point at ($\alpha = 5°$), an unstable trim point at ($\alpha = 13°$) and the stable spin point at ($\alpha = 21°$) for sideslip angles between ($-20° < \beta < 20°$). In Section 3.4 it is explained as to how changing the pitching moment coefficient as show above will result in a stable high AoA state. Furthermore the static rolling and yawing moment coefficients are modified to increase the roll and yaw moment forces experienced at high AoA and low sideslip angles.

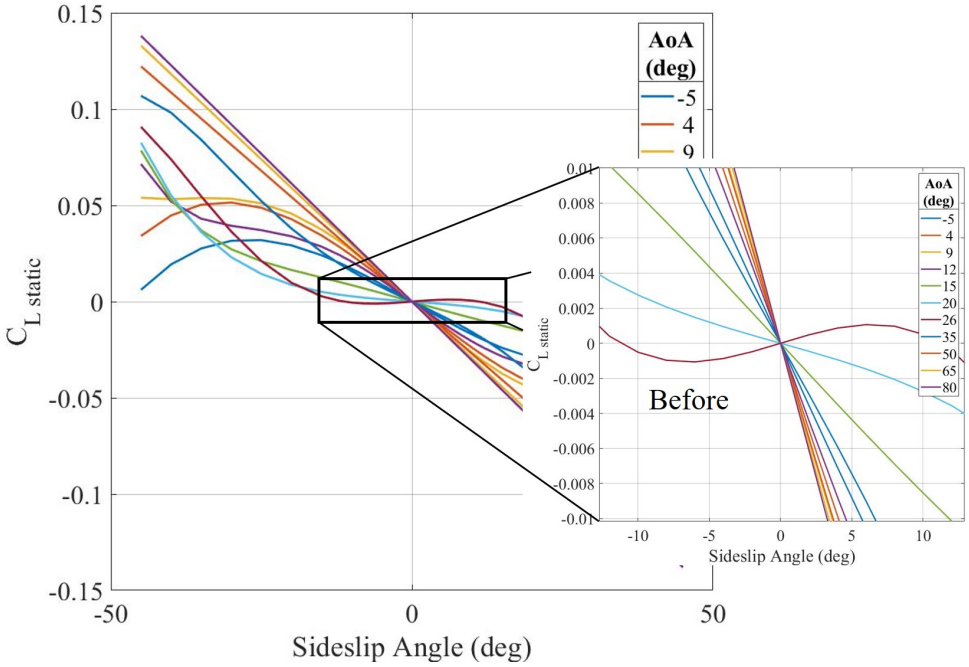

(a)

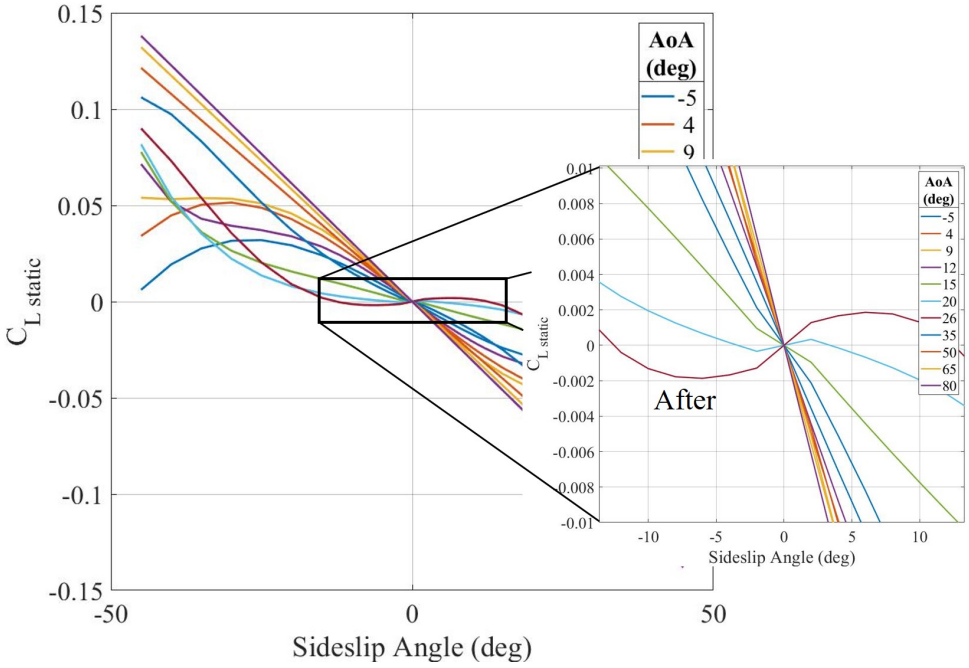

(b)

Figure 3.32: Modifications to the static rolling moment coefficient ($C_{L_{static}}$)

Figure 3.32 shows the modifications to the rolling moment coefficient. Note for AoA of

20 and 26 the coefficient was pulled down on the left and lifted up on the right. Instead of generating a damping rolling moment, an amplifying rolling moment is generated at these AoA and lower sideslip angles.

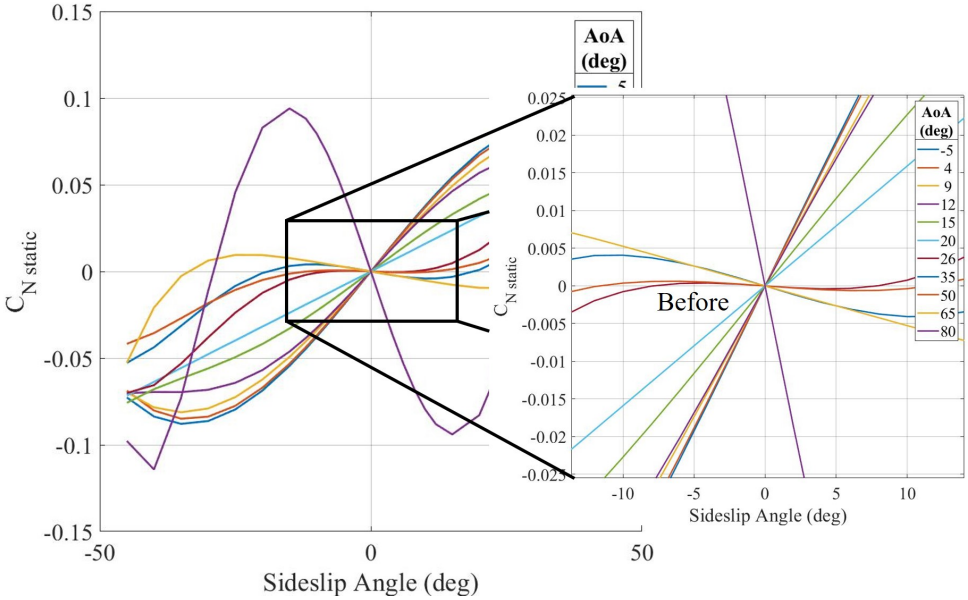

(a)

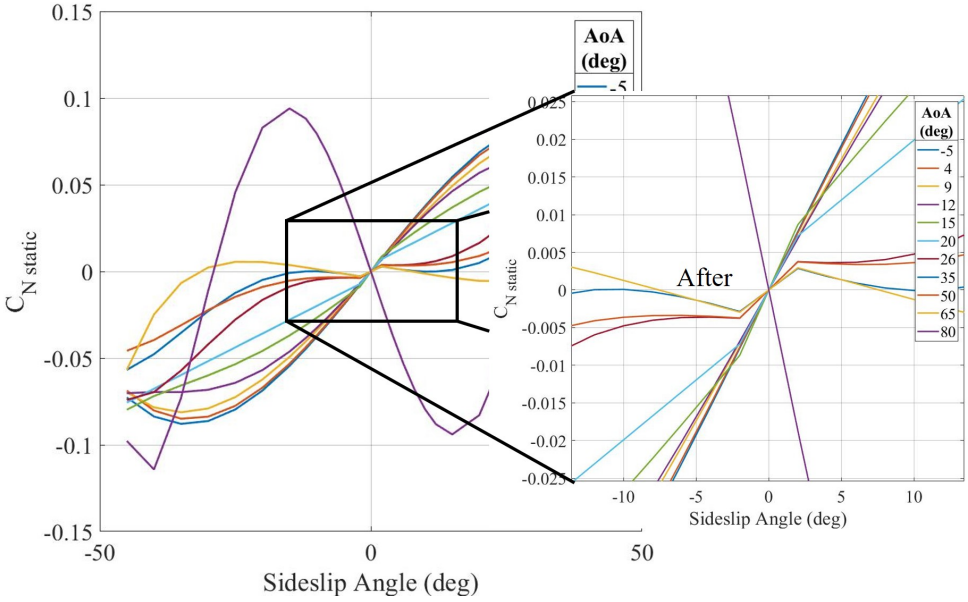

(b)

Figure 3.33: Modifications to the static yawing moment coefficient ($C_{N_{static}}$)

Figure 3.33 shows the modifications to the yawing moment coefficient. Similar to the previous modification, for AoA of 15 to 65 the yawing moment coefficient was pulled down on the left and lifted up on the right. Instead of generating a damping yawing moment, an amplifying yawing moment is generated at these high AoA and lower sideslip angles. With this modification applied the NASA GTM simulation was run and a ($\delta_E = -20°$) elevator deflection is applied from ($t = 3s$) to ($t = 5s$) as shown in Figure 3.34a.

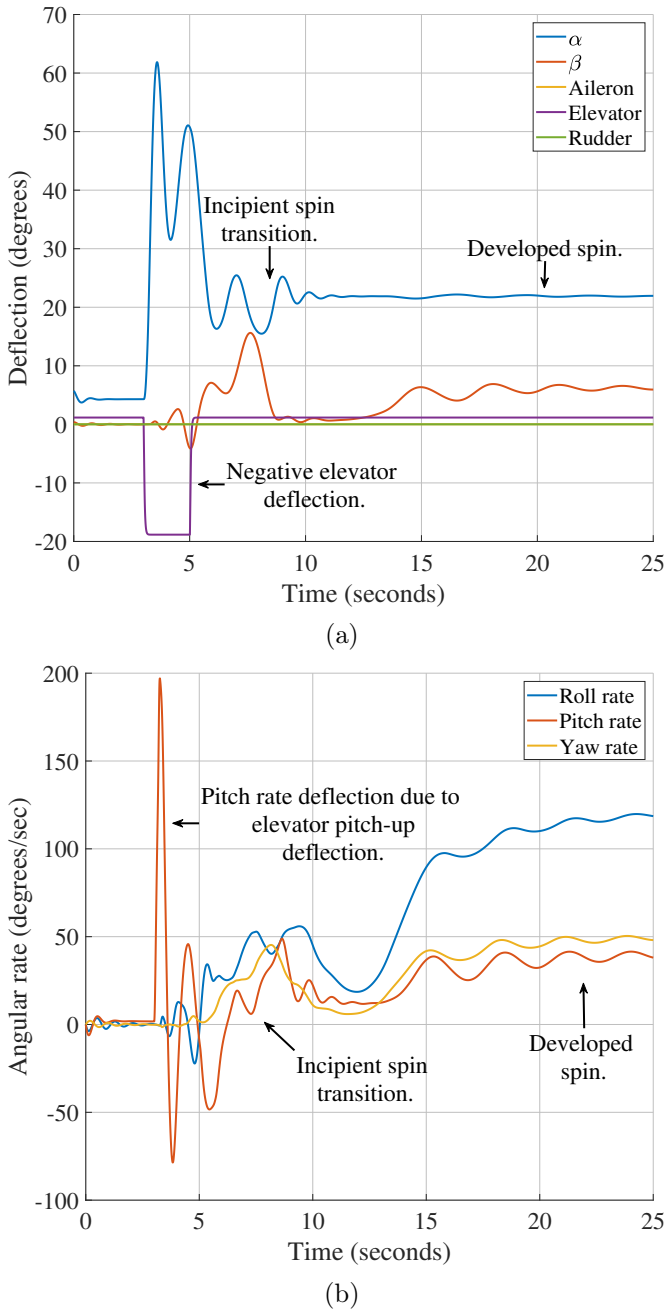

Figure 3.34: Sustained spin entry using a ($\delta_E = -20°$) elevator deflection on the spin modified NASA GTM.

In Figure 3.34b a large pitch rate deflection is observed due to the elevator deflection applied at ($t = 3s$). The angular rates transition to larger positive values as the aircraft settles at a high AoA of ($\alpha = 21°$) and this flight phase is known as the incipient spin. The sideslip angle also increases and settles at around ($\beta = 6°$) at ($t = 15s$). At ($t = 20s$) the aircraft's AoA, sideslip angle, and angular rates have settled and this flight phase is known as the developed spin. Due to no control surface deflection being actively applied while the aircraft is in the developed spin it can be said that this is a self-sustained spin. No further modifications to the NASA GTM are necessary and this finalises the spin modifications of the NASA GTM aerodynamic model.

3.5 Conclusion

This concludes Chapter 3 on the NASA GTM Aircraft model and the modifications made to the aerodynamic model. In this chapter the NASA GTM UAV as well as the simulation were introduced and a brief overview was given. The mathematical general flight dynamics model for a fixed-wing aircraft was explained to give a basic understanding of how the NASA GTM simulation works. It was attempted to enter the NASA GTM into a deep stall but was unsuccessful. After a few modifications to the NASA GTM aerodynamic model which are inline with the "Study of Deep Stall Characteristics and Longitudinal Special Phenomena of T-Tail Aircraft" by Wang and Shi [29] it is possible to enter the NASA GTM into a stable deep stall. The elevator deflections were also modified to have reduced effectiveness while the aircraft is in deep stall. Following this a brief overview of how spin is model is presented and it was attempted to enter the NASA GTM into a spin. A number of different spin states were noted but these were not self-sustaining spins. Modifications were made to the NASA GTM aerodynamic model and it was made possible to force the NASA GTM simulation into a stall using an elevator deflection. The spin modified NASA GTM transitioned from the incipient spin to a full developed spin without the application of control surface deflections. The modifications applied to the NASA GTM for both deep stall and spin modelling are satisfactory and in the following chapter the problem of deep stall recovery using trajectory planning will be addressed.

Chapter 4

Deep Stall Recovery

4.1 Introduction

This chapter will address the optimal deep stall recovery problem. First an overview of how the deep stall recovery algorithm is implemented into the control structure of an aircraft is given. Then the optimal control problem will be described and formulated and following that a reduced-order 3 degrees of freedom (3DoF) aircraft model is developed. The $A*$ trajectory planning solution will be presented and the optimal trajectory planning will be demonstrated. Finally, the planned trajectory will be executed on the NASA GTM for validation.

4.2 System Implementation

The diagram below proposes how the deep stall recovery system is to be integrated within an aircraft and in this case it would be the NASA GTM simulation.

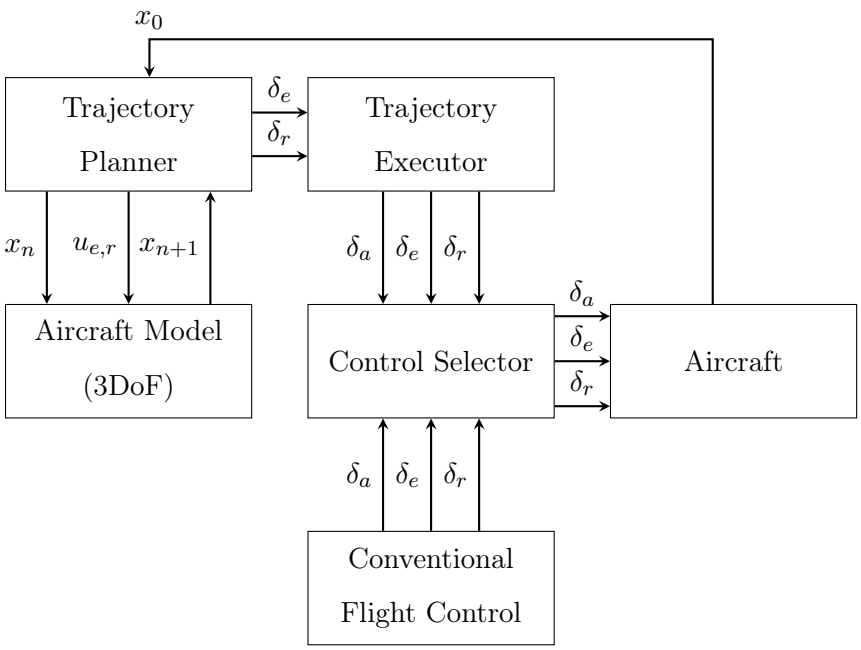

Figure 4.1: The architecture of the deep stall recovery system.

Once the system detects that the aircraft is in a deep stall condition, it uses a reduced-order, three-degrees-of-freedom (3DoF) model of the aircraft's fast rotational dynamics to determine the sequence of elevator and rudder actions that will transition the aircraft from its initial state in the deep stall region to a final state in the normal flight region. (The 3DoF model is sufficient for planning because the stall recovery is primarily a rotational recovery.) The deep stall recovery task is formulated as an optimal control problem and is solved using an A^* trajectory planning algorithm. The optimal sequence of elevator and rudder actions are then applied to the actual aircraft to perform the deep stall recovery.

4.3 Optimal Control Problem

The deep stall recovery task is formulated as an optimal control problem with the objective of finding the optimal sequence of control actions and the resulting optimal state trajectory to escape from the deep stall. It is assumed that the aircraft knows that it is in a state of deep stall and will only focus on recovering the aircraft to its normal flight envelope. The dynamic system is defined as the simplified, third-order nonlinear differential equations describing the fast rotational dynamics of the aircraft, while the slower point mass translational dynamics are treated as quasi-static. The fast rotational dynamics model therefore includes the wide-envelope aerodynamic models describing the aerodynamic moments, but not the aerodynamic forces.

The physical limits on the AoA, sideslip angle, and angular rates are specified by defining the sets of admissible states. The physical limits on the elevator and rudder deflections are specified by defining sets of admissible inputs. The requirement to recover the aircraft to the normal aerodynamic envelope (low AoA, low sideslip angle, and low angular rates) is translated into a set of admissible final states. The objective to recover the AoA as quickly as possible is translated into a cost function that is the time integral of the sum of the squares of the AoA and the sideslip angle.

Note that the deep stall recovery is not concerned with recovering the gross attitude (pitch angle and bank angle) of the aircraft relative to the inertial reference frame, nor is it concerned with recovering the flight vector (flight path angle and airspeed) of the aircraft. The purpose of deep stall recovery is rather to recover the AoA, sideslip angle and angular rates of the aircraft to the normal aerodynamic envelope where the normal flight control laws can be used to recover the gross attitude and point mass translation motion.

4.3.1 Problem Formulation

Given the initial state of the aircraft in the deep stall region (high AoA, low sideslip angle), the objective is to find the optimal sequence of elevator and rudder actions that will transition the aircraft to a final state in the normal flight region (low AoA, low sideslip angle) as quickly as possible, while obeying the aircraft's aerodynamic and physical constraints.

4.4 3DOF Dynamic Model

This section will give a full overview of the three degrees of freedom model which will be used to perform deep stall recovery trajectory planning. The 3DoF model's states are AoA, sideslip angle, roll rate, pitch rate and yaw rate.

$$\mathbf{x}(t) = \begin{bmatrix} \alpha & \beta & P & Q & R \end{bmatrix}^T \tag{4.1}$$

Kinematics

The 3DoF model inherits all of the rotational kinematics of the 6DoF model such as attitude parameters and angular rate coordinates. It is assumed that the deep stall recovery will be fast enough so that the translational kinematics of the aircraft will not change significantly throughout the recovery. For the 3DoF aircraft model the altitude (z) will be assumed to be quasi-static throughout the recovery and therefore the air density (ρ) will be quasi-static as it is directly dependent on the altitude. The airspeed ($\bar{v}$) will only significantly change after the aircraft recovers from the high AoA.

The aerodynamic drag of an aircraft is directly dependent on its AoA and therefore it will be assumed that the airspeed ($\bar{v}$) will be quasi-static throughout the recovery. Air density (ρ) and airspeed($\bar{v}$) determine the dynamic pressure ($\bar{q}$) as shown in Equation 3.13. Dynamic pressure ($\bar{q}$) is used to calculated the magnitude of the aerodynamic forces and moments applied on the aircraft as shown in equations 3.14 to 3.19.

The flight path angle (λ) and the heading angle (ψ) will also only change significantly after the AoA is recovered and full control authority is regained and therefore the flight path angle (λ) and the heading angle (ψ) will also be assumed to be quasi-static throughout the deep stall recovery. The translational kinematics therefore become quasi-static,

$$\begin{bmatrix} V_N \\ V_E \\ V_D \end{bmatrix} = \begin{bmatrix} V_{N_{static}} \\ V_{E_{static}} \\ V_{D_{static}} \end{bmatrix} \tag{4.2}$$

To determine the rotational kinematics that relate the AoA α and the sideslip angle β to the angular rates P, Q, and R the following equation derived by Pebble (2008) [25] (equation 2.29) will be used,

$$\begin{bmatrix} \dot{\alpha} \\ \dot{\beta} \end{bmatrix} = \begin{bmatrix} -\cos\alpha\tan\beta & 1 & -\sin\alpha\tan\beta \\ \sin\alpha & 0 & -\cos\alpha \end{bmatrix} \begin{bmatrix} P \\ Q \\ R \end{bmatrix} + \frac{1}{m\bar{V}} \begin{bmatrix} \sec\beta & 0 \\ 0 & 1 \end{bmatrix} \begin{bmatrix} Z_W \\ Y_W \end{bmatrix} \tag{4.3}$$

where Y_W and Z_W are the lateral and normal force vectors in the wind axis and are zero due to the quasi-static assumptions made previously.

$$\begin{bmatrix} \dot{\alpha} \\ \dot{\beta} \end{bmatrix} = \begin{bmatrix} -\cos\alpha\tan\beta & 1 & -\sin\alpha\tan\beta \\ \sin\alpha & 0 & -\cos\alpha \end{bmatrix} \begin{bmatrix} P \\ Q \\ R \end{bmatrix} \tag{4.4}$$

Kinetics

The kinetics of the 3DoF model include all the rotational dynamics of the aircraft as explained in the 6DoF model in Section 3.1.1. It does not include the translational dynamics as since the duration of the deep stall recovery is assumed to be short enough so that the translational dynamics can be neglected. The rotational dynamics that relates the angular acceleration of the aircraft to the aerodynamics moments acting on the aircraft body is given by

$$\begin{bmatrix} \dot{P} \\ \dot{Q} \\ \dot{R} \end{bmatrix} = \mathbf{I_B}^{-1} \left(- \begin{bmatrix} P \\ Q \\ R \end{bmatrix} \times \mathbf{I_B} \begin{bmatrix} P \\ Q \\ R \end{bmatrix} + \begin{bmatrix} L_A \\ M_A \\ N_A \end{bmatrix} \right) \tag{4.5}$$

where $\mathbf{I_B}$ is the moment of inertia matrix of the aircraft body, and L_A, M_A, and N_A are the aerodynamic moments acting on the aircraft.

Aerodynamic

The 3 DoF model inherits all the moment equations from the 6 DoF model as explained in 3.1.2. The aerodynamic moments are modelled by the following nonlinear equations,

$$\begin{bmatrix} L_A \\ M_A \\ N_A \end{bmatrix} = \frac{1}{2}\rho\bar{V}^2 S \begin{bmatrix} bC_l \\ \bar{c}C_m \\ bC_n \end{bmatrix} (\alpha, \beta, P, Q, R, \delta_A, \delta_E, \delta_R) \tag{4.6}$$

where ρ is the air density, $\bar{V}$ is the airspeed, S, $\bar{c}$, and b are the surface area, mean aerodynamic chord, and span of the wings, C_l, C_m, and C_n are the aerodynamic coefficient functions for rolling moment, pitch moment, and yawing moment and are formulated as:

$$C_l = F_{Cl}(\bar{V}, \alpha, \beta, p, q, r, \delta_A, \delta_E, \delta_R)$$

$$C_m = F_{Cm}(\bar{V}, \alpha, \beta, p, q, r, \delta_A, \delta_E, \delta_R)$$

$$C_n = F_{Cn}(\bar{V}, \alpha, \beta, p, q, r, \delta_A, \delta_E, \delta_R)$$

where δ_A, δ_E, and δ_E are the aileron, elevator and rudder deflections.

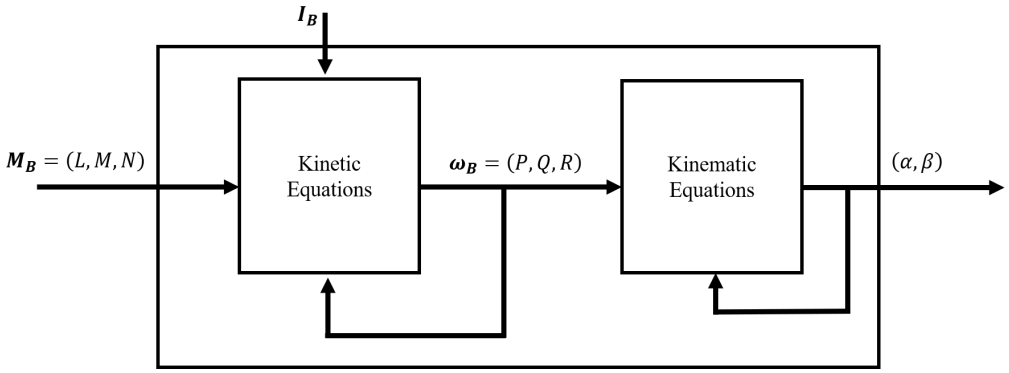

Figure 4.2: Block diagram overview of 3DoF EOM. Engelbrecht (2016) [9]

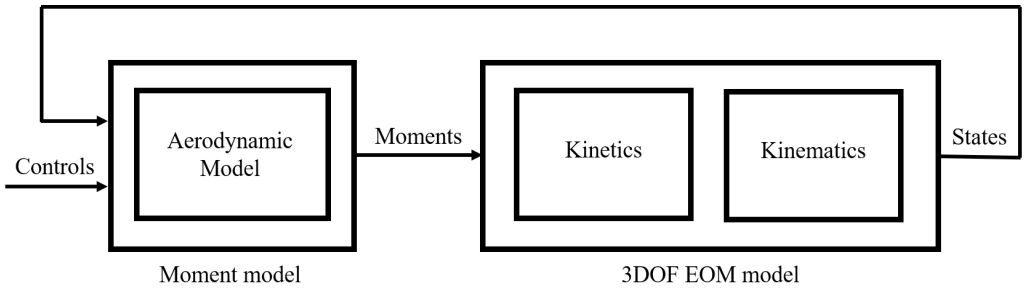

Figure 4.3: Block diagram overview of 3DoF aircraft model. Engelbrecht (2016) [9]

4.4.1 System State

The state vector $\mathbf{x}$ is defined as

$$\mathbf{x}(t) = \begin{bmatrix} \alpha & \beta & P & Q & R \end{bmatrix}^T \tag{4.7}$$

where α and β are the AoA and sideslip angle, P, Q and R are the roll rate, pitch rate and yaw rate coordinated in the body axis system.

4.4.2 Control Input

The control input vector $\mathbf{u}$ is defined as

$$\mathbf{u}(t) = \begin{bmatrix} \delta_A & \delta_E & \delta_R \end{bmatrix}^T \tag{4.8}$$

where δ_A, δ_E, and δ_E are the aileron, elevator and rudder deflections.

4.4.3 State Constraints

The state constraints are guided by the range of admissible states over which the aerodynamic model of the NASA GTM is valid.

$$\begin{aligned} \alpha(t) &\in [-5^\circ, +60^\circ] \\ \beta(t) &\in [-45^\circ, +45^\circ] \\ P(t) &\in [-200^\circ/s, +200^\circ/s] \\ Q(t) &\in [-80^\circ/s, +80^\circ/s] \\ R(t) &\in [-90^\circ/s, +90^\circ/s] \end{aligned}$$

To ensure that the planned trajectory does not cause any of the state variables to exceed the valid range of the NASA GTM while the actual trajectory is being performed it was decided to define the state constraints using the following reduced ranges:

$$\begin{aligned} \alpha(t) &\in [-5^\circ, +50^\circ] \\ \beta(t) &\in [-30^\circ, +30^\circ] \\ P(t) &\in [-110^\circ/s, +110^\circ/s] \\ Q(t) &\in [-45^\circ/s, +45^\circ/s] \\ R(t) &\in [-60^\circ/s, +60^\circ/s] \end{aligned}$$

4.4.4 Input Constraints

The control input constraints are defined by the range of admissible aileron, elevator, and rudder deflections

$$\begin{aligned} \delta_A(t) &\in [-20^\circ, +20^\circ] \\ \delta_E(t) &\in [-30^\circ, +20^\circ] \\ \delta_R(t) &\in [-30^\circ, +30^\circ] \end{aligned}$$

4.4.5 Goal Region / Terminal State Constraints

The requirement to recover the aircraft to the normal aerodynamic envelope (low angular rates, low AoA, and low sideslip angle) is translated into a goal region, or a set of admissible final states

$$\begin{aligned} \alpha(t_f) &\in [0^\circ, +10^\circ] \\ \beta(t_f) &\in [-10^\circ, +10^\circ] \\ P(t_f) &\in [-50^\circ/s, +50^\circ/s] \\ Q(t_f) &\in [-40^\circ/s, +0^\circ/s] \\ R(t_f) &\in [-50^\circ/s, +50^\circ/s] \end{aligned}$$

These values are chosen according for which states the aircraft is capable of returning to the normal flight orientation through the use of the normal flight control.

4.4.6 Cost Function

To compare different recovery trajectories to each other a cost function is required. The following costs are taken into consideration: The objective to return the AoA to the goal region in the shortest time possible is translated into the cost of absolute AoA multiplied by the time spent at that AoA. Therefore by reducing the AoA as fast as possible will translate into the lowest cost trajectory.

This could result in very high pitch rates in order to rapidly reduce the AoA. Therefore to prevent this the cost of the absolute pitch rate multiplied by the time spent at that pitch rate is also included. A weighting Q will be used to scale the cost added by the pitch rate.

$$J = \int_{t_0}^{t_f} [abs\left(\alpha(t) - \alpha_{\text{trim}}\right) \times t + Q \times abs\left(q(t) - q_{\text{trim}}\right) \times t]dt \tag{4.9}$$

where t_0 is the initial time of the recovery, t_f is the final time of the recovery, α_{trim} is the trim AoA to which the aircraft must be recovered, and q_{trim} is the trim pitch rate to which the aircraft must be recovered.

4.5 The *A** Solution

The optimal control problem is solved using the general A^* algorithm, shown in algorithm 1, described by [18]. The A^* algorithm was chosen because the five-dimensional state space of the 3DoF rotational dynamics model is too large for the optimal control problem to be solved using dynamic programming. The A^* algorithm starts at the initial state (x_I) and then generates all possible next states (x') by applying all possible input actions (u).

Each new state is tested to ensure that it is within the specified state constraints and that the state has not been visited before. A new state that was generated is selected and is then visited, and their next states are generated by applying all possible input actions again. Visited states are added to the closed list Q_{closed} and are referred to when checking if a specific state has been visited. The process is then iterated to grow a search tree until a goal state is found that is within the goal region.

Once a goal state is found, the algorithm follows the trail of previous states to determine the path from the initial state to the goal state. To find the optimal path, the A^* algorithm sorts the new states that are generated in a priority queue Q_{open} from the lowest path cost to the highest path cost.

The total path cost of a given state is calculated by adding the cost to come (the cost to reach the given state from the initial state) and the cost to go (the cost to reach the goal state from the given state). The cost to go is estimated using a heuristic function. By visiting the lowest cost states first, the A^* algorithm ensures that the first path that is found, will also be the optimal path according to a cost function.

Algorithm 1 Generic A^* Algorithm

Q_{open}.insert(x_I)
while Q_{open} not empty **and** size(Q_{closed}) $< N_{\max}$ **do**
  $x \leftarrow Q_{\text{open}}$.getFirst()
  if $x == x_G$ **then**
    return SUCCESS
  else
    for all $u \in U$ **do**
      $x' \leftarrow f(x, u)$
      if x' valid **then**
        $Q_{\text{open}}.insert(x')$
    Q_{closed}.insert(x)
return FAILURE

4.5.1 Algorithm Execution

A search tree is created to determine the optimal trajectory for the deep stall recovery. Each node in the tree contains the state, the action, the cost, and the time index of a possible point along the recovery trajectory. The algorithm starts with an initial node which represents the aircraft in a deep stall state as shown in Figure 4.4. The following diagrams will only show the AoA against the sideslip angle states of each node and its important to note that the other states such as the angular rates are also taken into consideration in the planning of the trajectory.

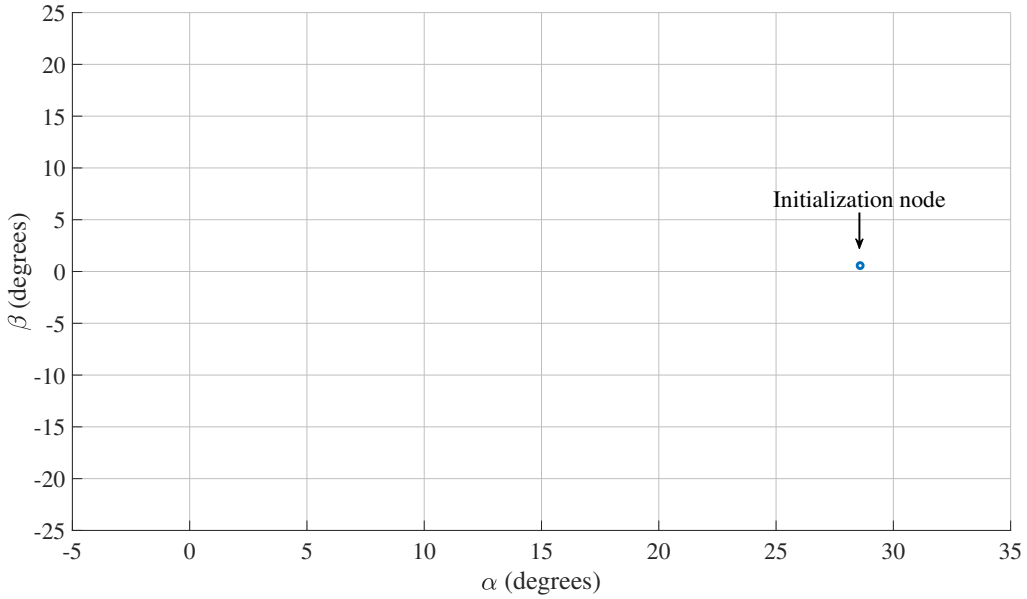

Figure 4.4: Initialisation of A^* trajectory planner.

Starting from the aircraft's initial state in the deep stall region, ($\alpha = 28°$) and ($\beta = 0.5°$), the search tree is grown to try and reach the goal region.

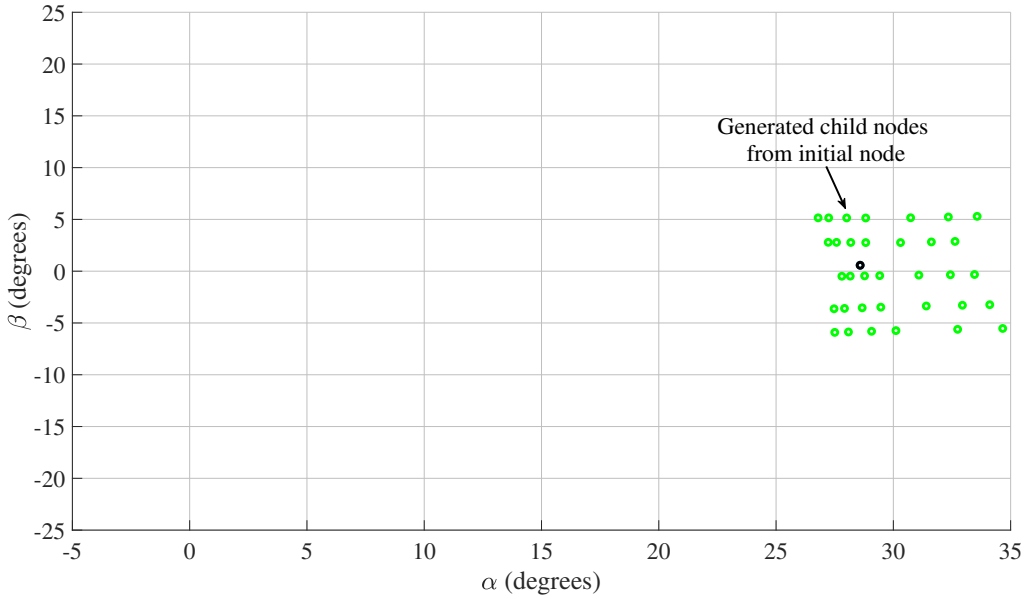

Figure 4.5: Generation of child nodes by A^* trajectory planner.

The initial node is selected to be visited and all combinations of available elevator and rudder actions in the action space are applied to that nodes state. The 3DoF dynamics model of the aircraft is used to calculated the new states which result from applying the control actions. These new states become the child nodes of the selected node. The cost-to-come and cost-to-go for each node is calculated and a priority queue is used determine the order in which the unvisited nodes are selected. The nodes in the priority queue are ordered from lowest to highest cost, so that the nodes with the lowest cost are selected first.

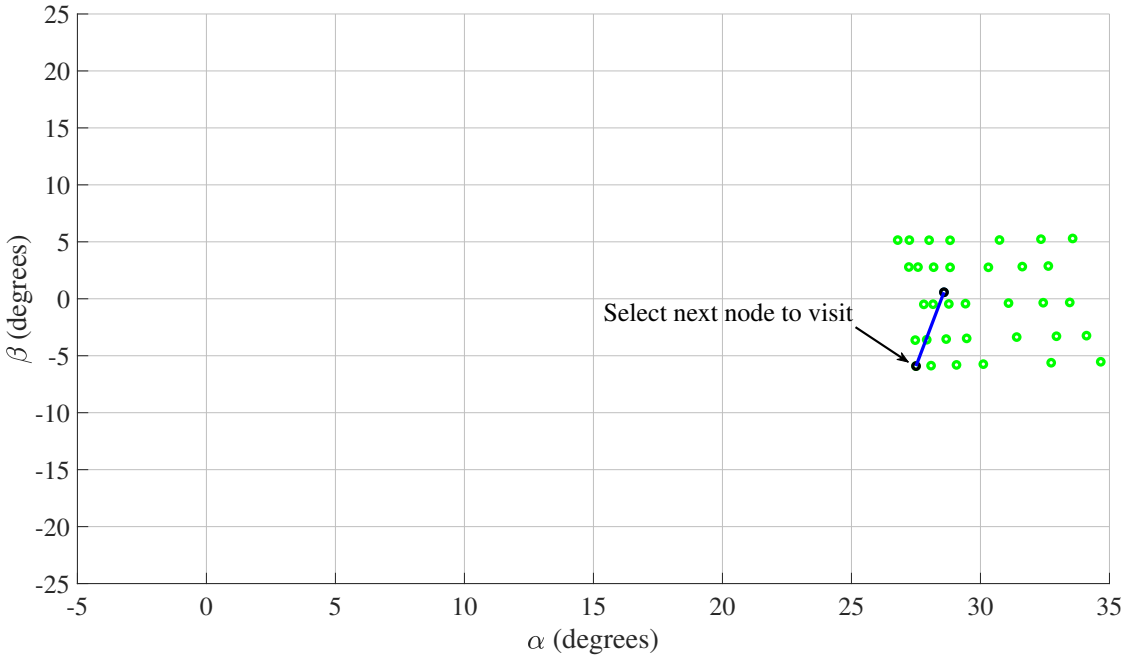

Figure 4.6: Selection of next node to visit by A^* trajectory planner.

When a new child node is created, its state is checked to make sure that it is admissible before it is added to the priority queue. This is done according to the admissible state

ranges as specified by the state constraints in Section 4.4.3.

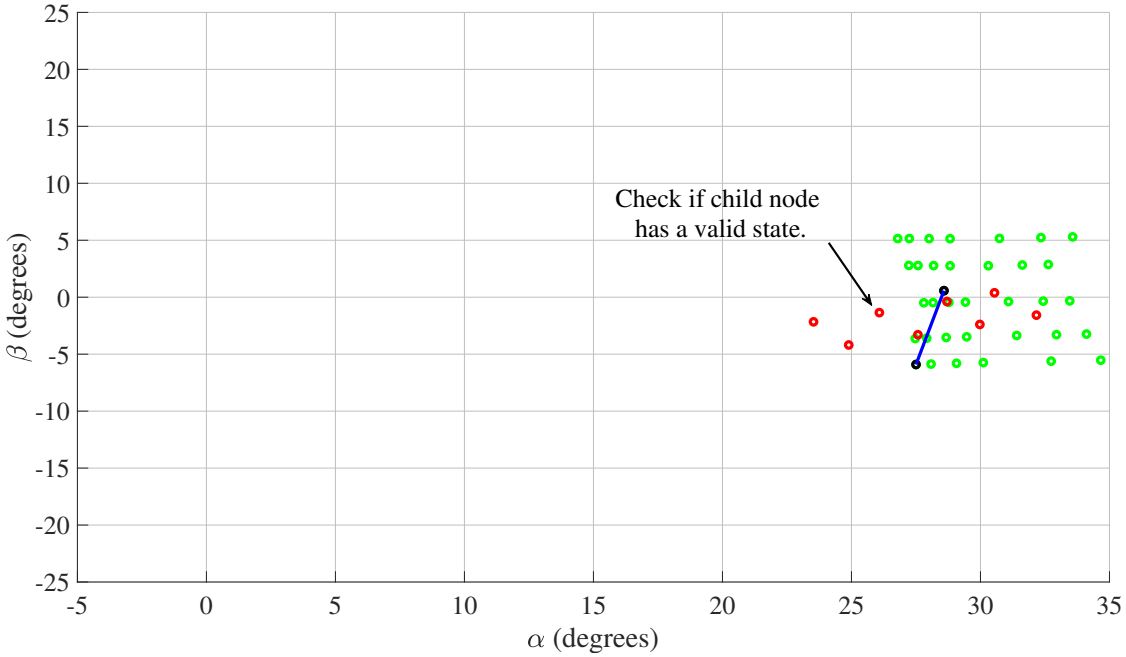

Figure 4.7: Elimination of invalid child nodes by A^* trajectory planner.

The A^* algorithm continues to explore the state space of the 3DoF dynamics model while repeating the steps of selecting the lowest cost node from the priority queue, applying the control actions to generate the new child nodes, removing invalid child nodes, calculating the cost of the valid child nodes and adding them to the priority queue.

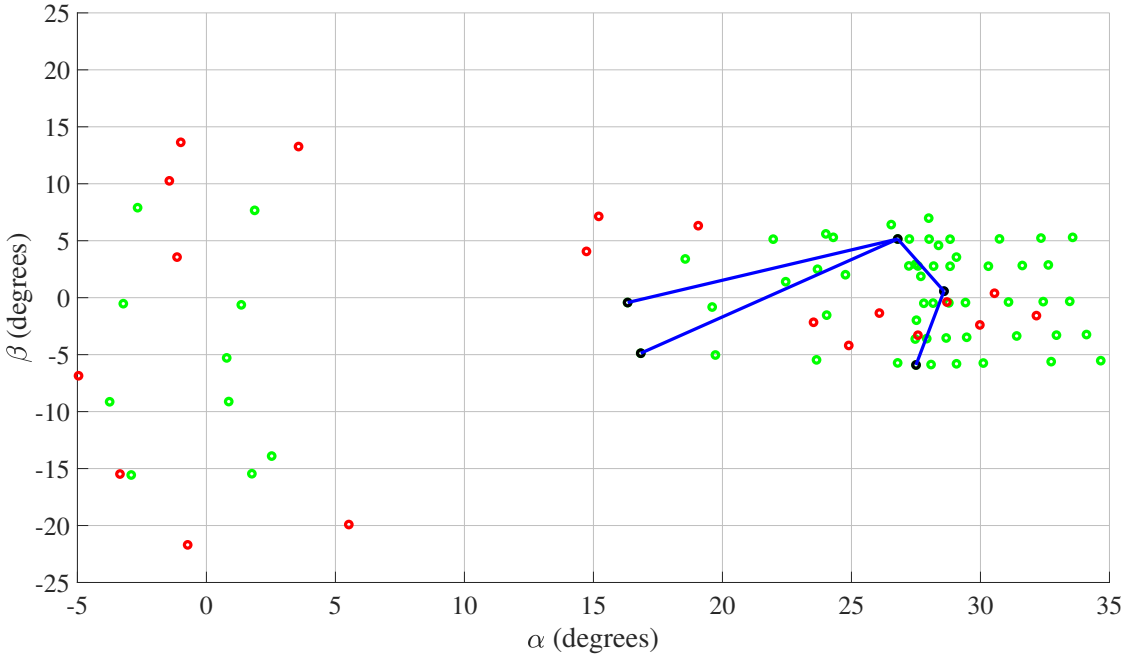

Figure 4.8: A^* trajectory planner search tree after a few iterations.

The A^* algorithm terminates when a node is selected that has a state which is within the goal region, or when the open queue is empty, or when the algorithm exceeds a predefined

maximum number of iterations.

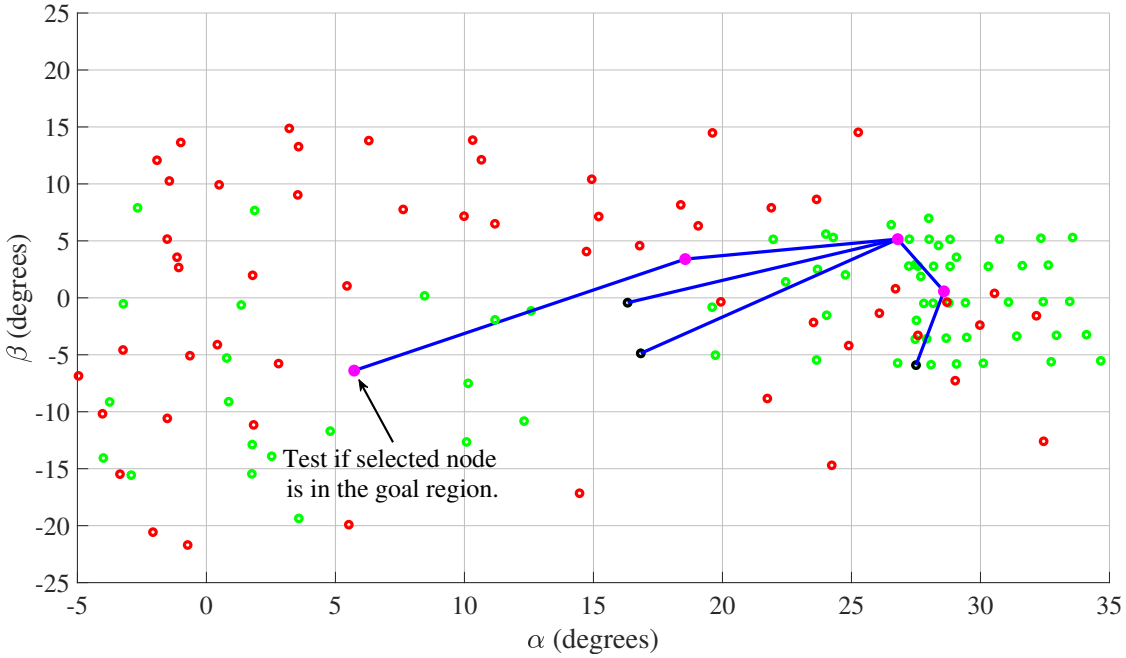

Figure 4.9: Testing if selected node is in the goal region by A^* trajectory planner.

This is a basic representation of how the A^* trajectory planner works to solve the deep stall recovery problem.

4.5.2 State Transition Equation

The following discrete-time, reduced-order, three-degrees-of-freedom model of the aircraft's fast rotational dynamics is used as the state transition equation to generate the child nodes from a given parent node,

$$\begin{aligned} \alpha(k+1) &= \alpha(k) + \dot{\alpha}(k)\Delta T \\ \beta(k+1) &= \beta(k) + \dot{\beta}(k)\Delta T \\ P(k+1) &= P(k) + \dot{P}(k)\Delta T \\ Q(k+1) &= Q(k) + \dot{Q}(k)\Delta T \\ R(k+1) &= R(k) + \dot{R}(k)\Delta T \end{aligned} \tag{4.10}$$

where k is the time index of the parent node, $k+1$ is the time index of the child node, ΔT is the sampling period of the discrete time step. The time derivatives $\dot{\alpha}$, $\dot{\beta}$, $\dot{P}$, $\dot{Q}$, and $\dot{R}$ for a given set of inputs δ_A, δ_E, and δ_R are calculated using equations 4.4, 4.5, and 4.6.

4.5.3 Action Space

The following discrete action space, consisting of a finite set of available elevator and rudder actions, is used to generate the child nodes from a given parent node

$$\begin{aligned} \delta_A(k) &\in \{0^\circ\} \\ \delta_E(k) &\in \{-30^\circ, -20^\circ, -10^\circ, 0^\circ, +8^\circ, +15^\circ, +20^\circ\} \\ \delta_R(k) &\in \{-30^\circ, -15^\circ, 0^\circ, +15^\circ, +30^\circ\} \end{aligned}$$

It is assumed that the ailerons will not be used for the deep stall recovery. This results in 35 different combinations of control input actions.

4.5.4 Cost To Come

The cost to come for each node is calculated incrementally as nodes are created and added to the search tree. The cost to come is the discrete-time integral of the absolute change in AoA and the change in time. The cost to come of a child node is calculated as the sum of the cost to come of the parent node and the incremental cost to transition from the parent node to the child node.

$$G(k+1) = G(k) + \Delta G \tag{4.11}$$

with

$$\Delta G = abs((\alpha(k+1) - \alpha(k)) + \Delta T \tag{4.12}$$

where $G(k)$ is the cost to come of the parent node, $G(k+1)$ is the cost to come of the child node, and ΔG is the incremental state transition cost.

4.5.5 Cost To Go Heuristic

The cost to go for each node is calculated using a heuristic function that estimates the cost of the best possible path from the child node to a goal node. The best possible path would be if the aircraft reached the goal node as fast as possible while still obeying the structural constraints of the aircraft.

$$H(k+1) = abs(\alpha(k+1) - \alpha_{\text{trim}}) + \frac{abs(\alpha(k+1) - \alpha_{\text{trim}})}{Q_{Max}} \times \Delta T \tag{4.13}$$

The cost to go is estimated to be the sum of the difference between the AoA at the child node and the AoA at trim, and the expected time required to reach the trim AoA from the the child node AoA.

4.5.6 Total Path Cost

The total path cost for each node is the sum of its cost to come and its cost to go.

$$J(k) \quad = \quad G(k) + H(k) \tag{4.14}$$

where J is the total path cost, G is the cost to come, and H is the cost to go for a given node in the deep stall recovery trajectory.

Choice of Sampling Period ΔT

The choice of time step was determined by taking into the consideration the slew rate of the control surfaces as well as the degree of discretisation used to divide up the control action space. The planned recovery sequence should be realistic and the control surface should be able to perform the sequence of actions. The control surfaces of the NASA GTM have a maximum rate of 300° per second. For the elevator control surface to move from the position of 20° to a position of −30° it requires therefore 0.1667s which if rounded

up to 0.2s meets the specified 5 Hz bandwidth which is applied to all the control surface within the NASA GTM simulation. It can therefore be concluded that the lower bound of the time step duration is 0.2s.

For every time step the $A*$ algorithm will generate 35 different control input combinations as specified by the control action space. If the deep stall recovery is to be 1.2s in duration then the recovery sequence will be 6 time steps in length if a time step size of 0.2s is used. At each time step 35 different action combinations are tested and will result at the 6th time step with the generation of $35^6 = 1838265625$ different recovery sequences. By increasing the time step size to 0.4s will reduce the number of time steps within the recovery to 3 and thereby the number of different possible recovery sequences is reduced to $35^3 = 42875$. It is therefore decided to use a time step size of 0.4s.

4.6 Optimal Trajectory Planning

The A* solution is used to find the sequence of control actions and the associated state trajectory to recover the aircraft from deep stall region. The planned sequence of control inputs and their expected deep stall recovery trajectory are shown in Figure 4.10. Note that the planned state trajectory and input sequence are generated using the simplified 3DoF aircraft model and the actual state trajectory executed by the real aircraft when the planned actions are applied may differ from the planned trajectory due to approximation errors.

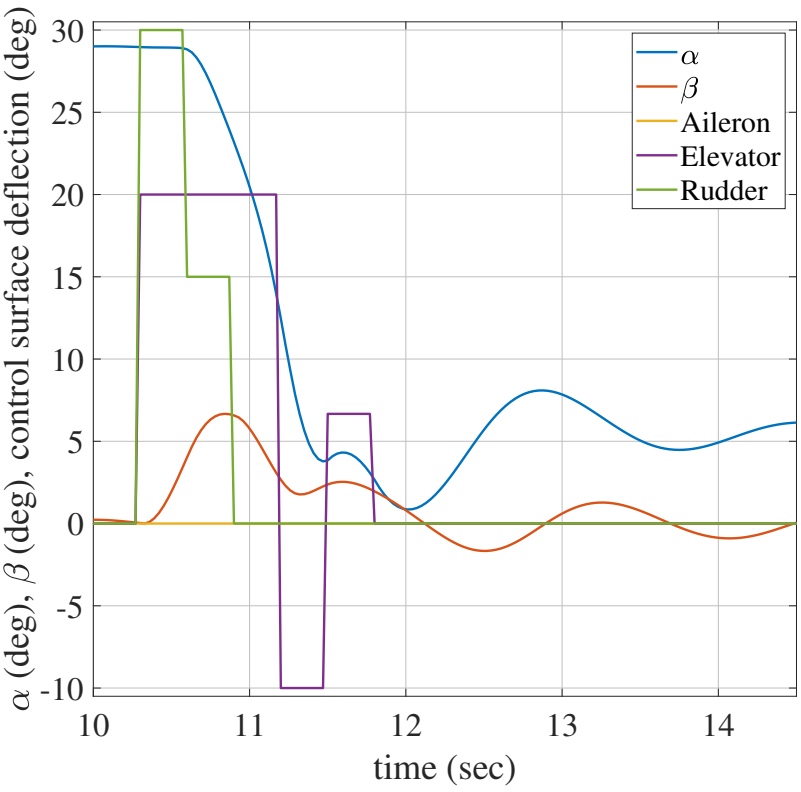

Figure 4.10: Planned deep stall recovery actions and trajectory.

The initial deep stall state that was given to the optimal trajectory planner was obtained from the deep stall entry performed with the full 6DoF GTM model in Section 3.4. The state at time $t = 10$s in Figure 3.24, when the aircraft had already settled at the deep

stall AoA, was assumed to be the initial deep stall state from which the aircraft must be recovered. The time histories in Figure 4.10 show that the initial state of the aircraft at $t = 10$s was an AoA of $\alpha = 28°$ and a sideslip angle of $\beta = 0°$. The planned sequence of recovery actions starts by simultaneously applying a rudder deflection, $\delta_R = 30°$, and a nose-down elevator deflection, $\delta_E = 20°$. The rudder deflection causes the sideslip angle β to increase from 0°to 6°, effectively swinging the horizontal tailplane out of the aircraft's wake to regain elevator effectiveness. When the sideslip angle β exceeds about 5°, the AoA α starts recovering due to the nose-down pitching moment produced by the elevators. While the AoA recovers, the rudder deflection is reduced to $\delta_R = 15°$ and then to $\delta_R = 0°$. When the AoA has been recovered to about $\alpha = 15°$, a nose-up elevator deflection $\delta_E = -10°$ is commanded to slow down the pitch rate. When the AoA drops below about $\alpha = 5°$, a nose-down elevator deflection $\delta_E = 6°$ is briefly commanded, and then the elevators are returned to trim. At this point, the aircraft has been recovered from the deep stall region, and the AoA returns to the trim AoA of $\alpha = 5°$ and the sideslip angle returns to zero degrees. This result is very pleasing, since it shows that the state trajectory and control inputs planned by the optimal trajectory planner agree with a typical prescribed deep stall recovery procedure that would be used by a human pilot.

4.7 Deep Stall Recovery Verification

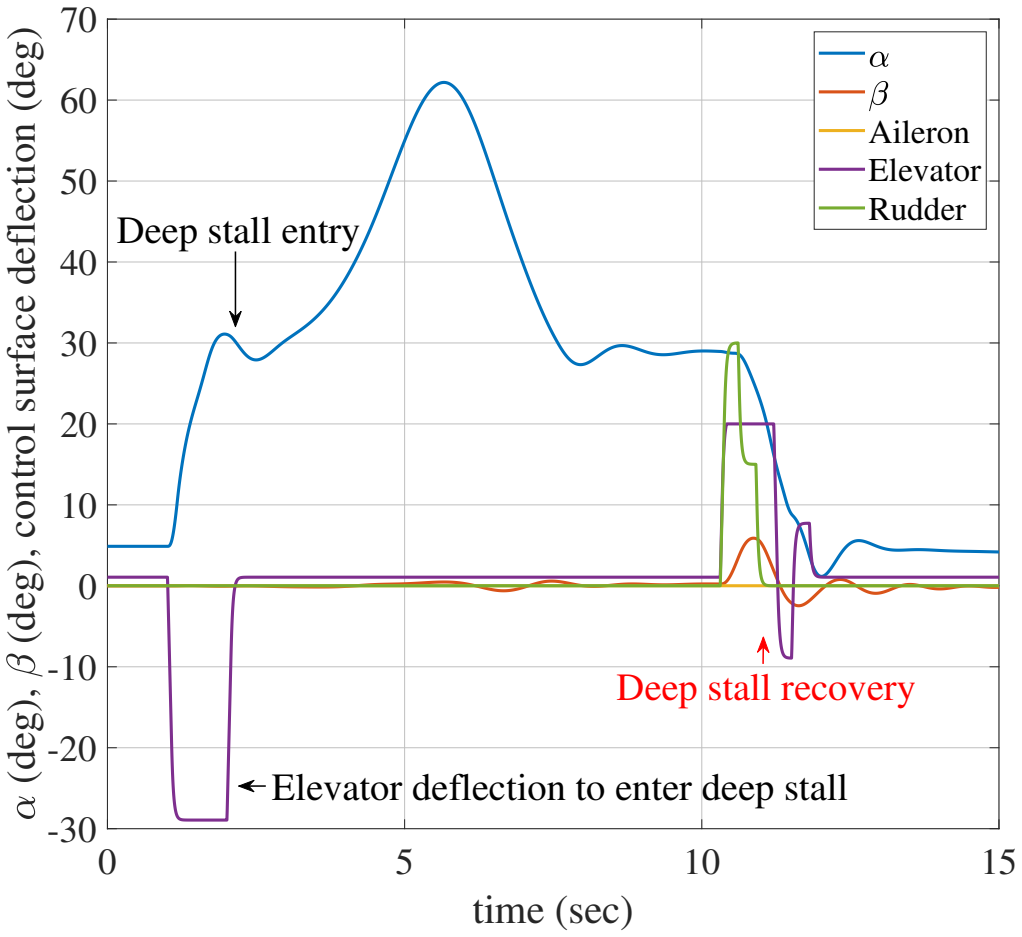

Figure 4.11: Deep stall recovery on the NASA GTM

The deep stall recovery actions that were planned using the simplified 3DoF model in the previous section will now be applied to the full 6DoF NASA GTM simulation model to verify that the automatic deep stall recovery system can successfully recover the "real" aircraft from deep stall. The simulation results are shown in Figure 4.11 and 4.12. The time histories of the AoA, sideslip angle, aileron, elevator, and rudder are shown in Figure 4.11. The first part of the simulation from time $t = 0$ to 10s follows exactly the same sequence as was performed in Figure 3.24 to push the aircraft into deep stall. However, this time the automatic deep stall recovery system is activated at $t = 10$s. The recovery system captures the aircraft state at that moment, plans the optimal sequence of recovery actions, and then executes the planned recovery actions on the aircraft. The simulation results from time $t = 0$ to 15s show that the full NASA GTM model is successfully recovered from deep stall to the normal aerodynamic envelope following a similar state trajectory to the planned state trajectory that was expected using the simplified 3DoF model. This validates the assumption that the simplified 3DoF model can be used to plan the deep stall recovery actions for the full aircraft. After the recovery sequence, the aircraft settles to an AoA $\alpha = 6°$ and a sideslip angle $\beta = 0°$ inside the normal aerodynamic envelope.

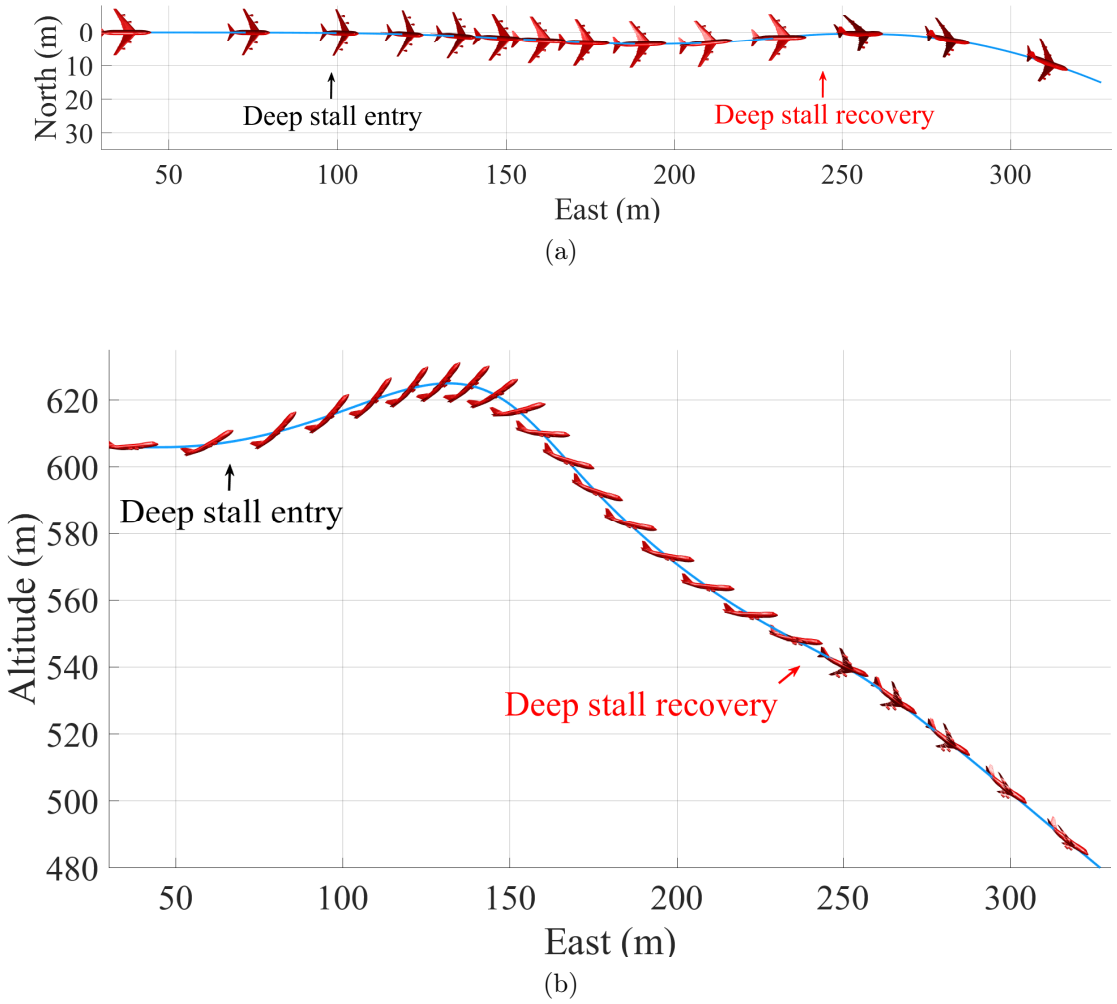

Figure 4.12: Deep stall entry and recovery trajectory (top view and side view).

The aircraft's trajectory during the deep stall entry and successful automatic recovery is shown in Figure 4.12. The trajectory shows that after the deep stall recovery, the aircraft

still has a nose-down pitch angle and a steeply descending flight path angle. As mentioned before, the deep stall recovery is only concerned with recovering the aerodynamic envelope, so that the conventional flight control laws and envelope protection functions are available again to perform the next stage of the recovery sequence. Once the aircraft has been recovered from deep stall, a different upset recovery function can be engaged to perform the attitude, flight path angle and airspeed recovery.

4.8 Conclusion

This chapter addressed the optimal deep stall recovery problem. The optimal control problem was described and formulated and the $A*$ solution was presented and implemented. The optimal trajectory planning was demonstrated and explained and it was explained how the solution is to be implemented in an actual aircraft. Finally, the deep stall recovery actions that were planned using the simplified 3DoF model were applied to the full 6DoF NASA GTM simulation model to verify that the automatic deep stall recovery system can successfully recover an actual aircraft from deep stall.

Chapter 5

Spin Recovery

5.1 Introduction

In this chapter a very similar approach to the previous chapter is followed in solving the optimal spin recovery problem. The formulation of the spin recovery trajectory planning algorithm is almost the same as that of the deep stall trajectory planning algorithm and therefore this chapter will focus on explaining the differences. The optimal control problem will be formulated for spin recovery.

The A^* solution as used in the previous chapter as well as and a Rapidly-exploring Random Tree (RRT) trajectory planning solution will be presented. The optimal trajectory planning system will be demonstrated and finally, the planned trajectory for the spin recovery will be simulated on the NASA GTM simulation and then discussed.

5.2 System Integration

The Figure 5.1 shows how the spin recovery system is integrated with the aircraft (NASA GTM). Once the flight control system detects that the aircraft is in a spin condition, it uses a six-degrees-of-freedom (6DoF) model of the aircraft dynamics to determine the sequence of elevator and rudder actions that will transition the aircraft from its initial state in the spin region to a final state in the normal flight region.

The spin recovery task is formulated as an optimal control problem and is solved using an A^* trajectory planning algorithm or the RRT trajectory planning algorithm. The optimal sequence of elevator and rudder actions as well as the recovery trajectory are passed to the trajectory regulator. The trajectory regulator applies the recovery sequence to the aircraft, the NASA GTM, to perform the spin recovery and ensures that the aircraft's states track the calculated recovery trajectory.

Once the system detects that the aircraft has re-entered the normal flight envelope it switches back to using the normal flight control of the aircraft and starts attitude, altitude, airspeed and heading recovery. The switching function will be described in the following Section 6.3.

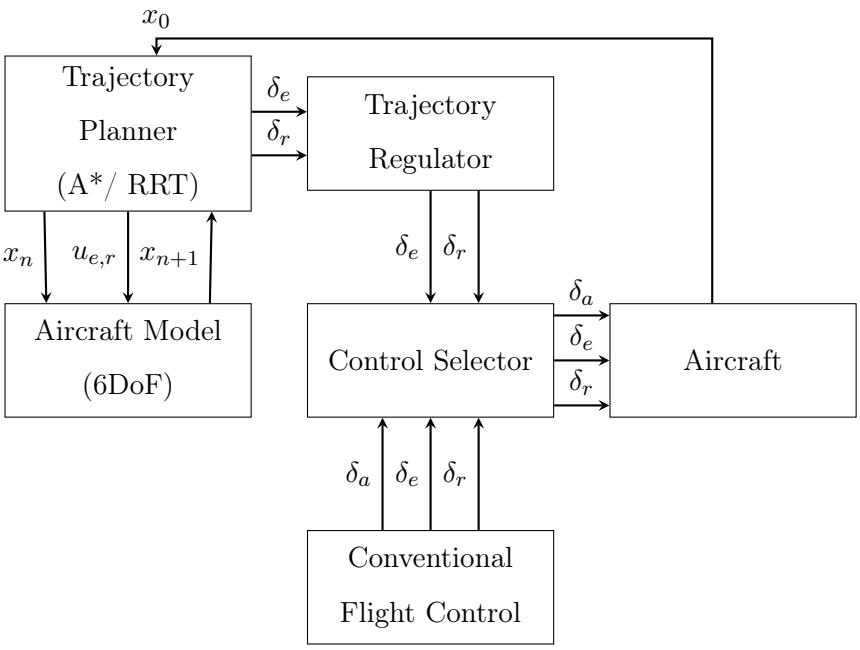

Figure 5.1: The architecture of the spin recovery system.

5.3 Optimal Control Problem

The spin recovery task is formulated as an optimal control problem with the objective of finding the optimal sequence of control actions and the resulting optimal state trajectory to escape from the spin and recover the normal flight envelope. The dynamic system cannot be defined as the simplified, third-order nonlinear differential equations describing just the fast rotational dynamics of the aircraft. This is because the slower point mass translational dynamics cannot be treated as quasi-static. The dynamic system for spin recovery requires the full sixth-order nonlinear differential equations as described in the Aircraft Models chapter under Section 3.2.

The physical limits on the AoA, sideslip angle, and angular rates are specified by defining the sets of admissible states. The physical limits on the elevator and rudder deflections are specified by defining sets of admissible inputs. The requirement to recover the aircraft to the normal aerodynamic envelope (low AoA, low sideslip angle, and low angular rates) is translated into a set of admissible final states. The objective to recover the AoA as quickly as possible is translated into a cost function that is the time integral of the sum of the change in AoA and the duration of the recovery.

Note that the spin recovery is also not concerned with recovering the gross attitude (pitch angle and bank angle) of the aircraft relative to the inertial reference frame, nor is it concerned with recovering the flight vector (flight path angle and airspeed) of the aircraft. The purpose of spin recovery is rather to recover mainly the angular rates, the AoA and the sideslip angle of the aircraft to the normal aerodynamic envelope from where the normal flight control laws can be used to recover the gross attitude and point mass translation motion.

5.3.1 Problem Formulation

Given the initial state of the aircraft in the spin region (high AoA and angular rates, low sideslip angle), the objective is to find the optimal sequence of elevator and rudder actions

that will transition the aircraft to a final state in the normal flight region (low AoA, low angular rates and low sideslip angle) as quickly as possible, while obeying the aircraft's aerodynamic and physical constraints.

5.3.2 Dynamic System

The dynamic system is represented by the six-degrees-of-freedom nonlinear differential equations that describe the full dynamics of the aircraft. The north and east components of the inertial position vector do not couple back into the 6DoF model equations and therefore can be neglected. The down component of the inertial position vector is used in the calculation of the air density but due to the assumption as made in the previous deep stall recovery chapter it too can be assumed to be quasi-static and therefore the air density can also be assumed to be quasi-static. With this assumption in place it can be assumed that the inertial velocity vector can also be neglected. In the 6DoF model the body angular rate coordinates of the aircraft (P,Q,R) are related to the rate of change of attitude parameter coordinates.

$$\begin{bmatrix} \dot{\Phi} \\ \dot{\Theta} \\ \dot{\Psi} \end{bmatrix} = \begin{bmatrix} 1 & \sin(\Phi)\tan(\Theta) & \cos(\Phi)\tan(\Theta) \\ 0 & \cos(\Phi) & -\sin(\Phi) \\ 0 & \sin(\Phi)\sec(\Theta) & \cos(\Phi)\sec(\Theta) \end{bmatrix} \begin{bmatrix} P_b \\ Q_b \\ R_b \end{bmatrix}$$

The general six degree of freedom vector equations of motion relate the forces and moments acting on the aircraft to changes in the aircraft's translational position, velocity and acceleration,

$$\dot{U} = \frac{X}{m} - WQ + VR \tag{5.1}$$

$$\dot{V} = \frac{Y}{m} - UR + WP \tag{5.2}$$

$$\dot{W} = \frac{Z}{m} - VP + UQ \tag{5.3}$$

and changes in the aircraft's rotational position, velocity and acceleration,

$$\dot{P} = \frac{L}{I_{xz}} - \frac{QR(I_{zz} - I_{yy})}{I_{xx}} \tag{5.4}$$

$$\dot{Q} = \frac{M}{I_{yy}} - \frac{PR(I_{xx} - I_{zz})}{I_{yy}} \tag{5.5}$$

$$\dot{R} = \frac{N}{I_{zz}} - \frac{PQ(I_{yy} - I_{xx})}{I_{zz}} \tag{5.6}$$

The different forces and moments are summed together in their respective directions to yield the following equations,

$$X = X^A + X^G + X^T \tag{5.7}$$

$$Y = Y^A + Y^G + Y^T \tag{5.8}$$

$$Z = Z^A + Z^G + Z^T \tag{5.9}$$

$$L = L^A + L^{CG} \tag{5.10}$$

$$M = M^A + M^{CG} \tag{5.11}$$

$$N = N^A + N^{CG} \tag{5.12}$$

Aerodynamic forces (X,Y,Z) and moments (L,M,N) are described within the body axis system and yield the following equations:

$$\begin{aligned} X^A &= qSC_X \\ Y^A &= qSC_Y \\ Z^A &= qSC_Z \\ L^A &= qSbC_l \\ M^A &= qS\bar{c}C_m \\ N^A &= qSbC_n \end{aligned}$$

where S is the wing area, b is the wing span, $\bar{c}$ is the mean aerodynamic chord and $C_{()}$ are the non-dimensional aerodynamic force and moment coefficients.

$$\begin{aligned} C_X &= F_{CX}(\overline{V}, \alpha, \beta, p, q, r, \delta_A, \delta_E, \delta_R) \\ C_Y &= F_{CY}(\overline{V}, \alpha, \beta, p, q, r, \delta_A, \delta_E, \delta_R) \\ C_Z &= F_{CZ}(\overline{V}, \alpha, \beta, p, q, r, \delta_A, \delta_E, \delta_R) \\ C_l &= F_{Cl}(\overline{V}, \alpha, \beta, p, q, r, \delta_A, \delta_E, \delta_R) \\ C_m &= F_{Cm}(\overline{V}, \alpha, \beta, p, q, r, \delta_A, \delta_E, \delta_R) \\ C_n &= F_{Cn}(\overline{V}, \alpha, \beta, p, q, r, \delta_A, \delta_E, \delta_R) \end{aligned}$$

where the function looks-up the value of the coefficient from the extensive aerodynamic model of the NASA GTM at given specific parameter states. The lookup table requires the AoA and sideslip angle and these are calculated as follows,

$$\begin{aligned} \overline{V} &= \sqrt{U^2 + V^2 + W^2} \\ \alpha &= \tan^{-1}\left(\frac{U}{\overline{V}}\right) \\ \beta &= \sin^{-1}\left(\frac{U}{\overline{\overline{V}}}\right) \end{aligned}$$

The force of gravity is described as follows,

$$\begin{bmatrix} X^G \\ Y^G \\ Z^G \end{bmatrix} = \begin{bmatrix} -\sin\Theta \\ \cos\Theta\sin\Phi \\ \cos\Theta\cos\Phi \end{bmatrix} mg$$

Due to the choice of using the centre of gravity of the aircraft as the origin of the body axis system there will be no moment caused by gravity acting on the aircraft. The aircraft will be kept at constant trim thrust throughout the recovery,

$$T = T_{trim}$$

and is directed in the negative direction of the x-axis of the body axes system.

$$X^T = T$$

This is a summary of the six-degrees of freedom aircraft model which was explained in Section 3.2.

5.3.3 System State

The state vector $\mathbf{x}$ is defined as

$$\mathbf{x}(t) = \begin{bmatrix} U & V & W & P & Q & R & \Phi & \Theta & h \end{bmatrix}^T \tag{5.13}$$

where U, V and W are the velocity vectors relative to the body axis reference frame, P, Q and R are the roll rate, pitch rate and yaw rate also coordinated in the body axis system, Φ and Θ are the roll angle and pitch angle relative to the inertial reference frame, and h is the altitude of the aircraft relative to the inertial reference frame.

5.3.4 Control Input

The control input vector $\mathbf{u}$ is defined as,

$$\mathbf{u}(t) = \begin{bmatrix} \delta_A & \delta_E & \delta_R \end{bmatrix}^T \tag{5.14}$$

where δ_A, δ_E, and δ_E are the aileron, elevator and rudder deflections.

5.3.5 State Constraints

The state constraints are defined in the previous chapter and restated. These state constraints represent the range of admissible states over which the aerodynamic model of the NASA GTM simulation is valid.

$$\begin{aligned} \alpha(t) &\in [-5^\circ, +60^\circ] \\ \beta(t) &\in [-45^\circ, +45^\circ] \\ P(t) &\in [-200^\circ/s, +200^\circ/s] \\ Q(t) &\in [-80^\circ/s, +80^\circ/s] \\ R(t) &\in [-90^\circ/s, +90^\circ/s] \end{aligned}$$

The search algorithm was restricted to use the following state constraints:

$$\begin{aligned} \alpha(t) &\in [-5^\circ, +60^\circ] \\ \beta(t) &\in [-30^\circ, +30^\circ] \\ P(t) &\in [-200^\circ/s, +200^\circ/s] \\ Q(t) &\in [-80^\circ/s, +80^\circ/s] \\ R(t) &\in [-90^\circ/s, +90^\circ/s] \end{aligned}$$

This is to ensure that no trajectory is generated which approaches the actual model constraints too closely. It was decided to not restrict the state constraints by much as spin is a very dynamic maneuver which will result in aircraft parameters coming close to the state constraints but which are still valid.

5.3.6 Input Constraints

The control input constraints are defined by the range of admissible aileron, elevator, and rudder deflections and are restated here from the previous chapter.

$$\begin{aligned} \delta_A(t) &\in [-20^\circ, +20^\circ] \\ \delta_E(t) &\in [-30^\circ, +20^\circ] \\ \delta_R(t) &\in [-30^\circ, +30^\circ] \end{aligned}$$

5.3.7 Goal Region / Terminal State Constraints

The requirement to recover the aircraft to the normal aerodynamic envelope (low angular rates, low AoA, and low sideslip angle) is translated into a goal region, or a set of admissible final states.

$$\begin{aligned} \alpha(t_f) &\in [-5^\circ, +15^\circ] \\ \beta(t_f) &\in [-15^\circ, +15^\circ] \\ P(t_f) &\in [-80^\circ/s, +80^\circ/s] \\ Q(t_f) &\in [-50^\circ/s, +50^\circ/s] \\ R(t_f) &\in [-60^\circ/s, +60^\circ/s] \end{aligned}$$

The goal region for spin is larger than that of deep stall due to the high angular rates that occur during a spin. Over constraining the goal region could result in overly complex recovery sequences and under constraining the goal region could lead to infeasible recovery solutions. Examples of this will be given in the verification section.

5.3.8 Cost Function

Similar to the deep stall recovery,the objective is to return the AoA to the normal aerodynamic envelope as soon as possible in order to reattach the airflow across the main wings by returning the AoA to the trim AoA. Thereby normal control authority is regained and allows for well developed control laws to be applied to recover from over or under speed as well as attitude, heading, flight path angle and altitude recovery. Due to the high angular rates present in spin it is important to include them into the cost function as well, else a trajectory could be selected which results in angular rates which exceed the state constraints. The following cost function is used,

$$J = \int_{t_0}^{t_f} [\sqrt[2]{\mathbf{\Delta x}(t)^T Q \mathbf{\Delta x}(t)} + \sqrt[2]{\mathbf{\Delta u}(t)^T R \mathbf{\Delta u}(t)}] dt \tag{5.15}$$

$$\mathbf{\Delta x}(t) = abs\left(\mathbf{x_{A^*}}(t) - \mathbf{x}_{\text{trim}}\right) \times t) \tag{5.16}$$

$$\mathbf{x_{A^*}}(t) = \begin{bmatrix} \alpha(t) & \beta(t) & p(t) & q(t) & r(t) \end{bmatrix}^T \tag{5.17}$$

$$\mathbf{x}_{\text{trim}} = \begin{bmatrix} \alpha_{trim} & \beta_{trim} & p_{trim} & q_{trim} & r_{trim} \end{bmatrix}^T \tag{5.18}$$

$$\mathbf{\Delta u}(t) = abs\left(\mathbf{u_{A^*}}(t) - \mathbf{u}_{\text{trim}}\right) \times t) \tag{5.19}$$

$$\mathbf{u_{A^*}}(t) = \begin{bmatrix} \delta_e(t) & \delta_r(t) \end{bmatrix}^T \tag{5.20}$$

$$\mathbf{u}_{\text{trim}} = \begin{bmatrix} \delta_{e(trim)} & \delta_{r(trim)} \end{bmatrix}^T \tag{5.21}$$

where t_0 is the initial time, t_f is the final time, and α_{trim} is the trim AoA to which the aircraft must be recovered.

5.4 The A^* Solution

It is attempted to solve the spin recovery problem using the general A^* algorithm, shown in Algorithm 1 in the previous chapter, described by [18].The nine-dimensional state space of the 6DoF dynamics model is too large for the optimal control problem to be solved using dynamic programming. The A^* solution is well suited for problems with high-dimensional state spaces. An overview of how the algorithm works is given in the previous chapter under Section 4.5.

Algorithm Execution

The A^* solution for spin recovery makes use of a 6DoF aircraft model and an explanation of how the algorithm is executed is given in the previous chapter under Section 4.5.1.

State Transition Equation

The following discrete-time, six-degrees-of-freedom (6DoF) model of the aircraft is used as the state transition equation to generate the child nodes from a given parent node,

$$\begin{aligned}
U(k+1) &= U(k) + \dot{U}(k)\Delta T \\
V(k+1) &= V(k) + \dot{V}(k)\Delta T \\
W(k+1) &= W(k) + \dot{W}(k)\Delta T \\
P(k+1) &= P(k) + \dot{P}(k)\Delta T \\
Q(k+1) &= Q(k) + \dot{Q}(k)\Delta T \\
R(k+1) &= R(k) + \dot{R}(k)\Delta T \\
\Phi(k+1) &= \Phi(k) + \dot{\Phi}(k)\Delta T \\
\Theta(k+1) &= \Theta(k) + \dot{\Theta}(k)\Delta T \\
H(k+1) &= H(k) + \dot{H}(k)\Delta T
\end{aligned} \tag{5.22}$$

where k is the time index of the parent node, $k+1$ is the time index of the child node, ΔT is the sampling period of the discrete time step. The time derivatives $\dot{U}$, $\dot{V}$, $\dot{W}$, $\dot{P}$, $\dot{Q}$, $\dot{R}$, $\dot{\Phi}$, $\dot{\Theta}$, and $\dot{H}$ for a given set of inputs δ_A, δ_E, and δ_R are calculated using equations 3.2, 3.3, 3.7, and 3.10. For trajectory planning the states $\alpha(k), \beta(k)$ are calculated using the following equations,

$$\alpha(k) = \arctan\left(\frac{W(k)}{U(k)}\right) \tag{5.23}$$

$$\beta(k) = \arcsin\left(\frac{V(k)}{\overline{V}(k)}\right) \tag{5.24}$$

where,

$$\overline{V}(k) = \sqrt{U^2 + V^2 + W^2} \tag{5.25}$$

Action Space

The following discrete action space, consisting of a finite set of available elevator and rudder actions, is used to generate the child nodes from a given parent node. Note that here the sample set is expanded when compared to the deep stall recovery solution action space. This is due to the spin recovery requiring finer control of roll and yaw rates which required the addition of the smaller rudder deflections $+/-5°$.

$$\begin{aligned}\delta_A(k) &\in \{0°\}\\ \delta_E(k) &\in \{-30°, -20°, -10°, -5°, 0°, +5°, +10°, +20°\}\\ \delta_R(k) &\in \{-30°, -20°, -10°, -5°, 0°, +5°, +10°, +20°, +30°\}\end{aligned}$$

To improve performance of the algorithm the method of input limiting was applied. This refers to limiting the available actions dependent on the previous action. For example if the previous elevator command was 0 degrees for the next time step the possible elevator commands can only include positions which are close to 5°such as -10°, 0°, or 10°.

This reduces the input space which the search algorithm must explore and therefore improves the algorithms performance. This example has an input spread of one. For spin an input spread of two was applied which allows for elevator commands to be -10°, -5°, 0°, 5°, 10°if the current elevator command is 0°.

Choice of Sampling Period ΔT

As explained in the previous chapter the choice of time step was determined by taking into the consideration the slew rate of the control surfaces as well as the degree of discretisation used to divide up the control action space. For every time step the $A*$ algorithm for the spin recovery solution could generate up to 72 different control input combinations as specified by the control action space and input limiting.

If the spin recovery is to be $0.6s$ in duration then the recovery sequence will be three time steps in length if a time step size of $0.2s$ is used. At each time step 72 different action combinations could be tested and will result at the 3rd time step with the generation of 373248 different recovery sequences. By increasing the time step size to $0.3s$ the number of different possible recovery sequences is reduced to 5184.

Cost To Come

Similar to the previous chapter the cost to come for each node is calculated incrementally as nodes are created and added to the search tree. The cost to come for spin is similar to that defined in Section 4.5.4.

$$G(k+1) = G(k) + \Delta G(k)$$

with

$$\mathbf{\Delta G}(k) = \sqrt[2]{\mathbf{\Delta x}(k)^T_{cc} Q \mathbf{\Delta x}_{cc}(k)} + \sqrt[2]{\mathbf{\Delta u}_{cc}(k)^T R \mathbf{\Delta u}_{cc}(k)} \tag{5.26}$$

$$\mathbf{\Delta x}_{cc}(k) = \frac{\mathbf{x}(k) + \mathbf{x}(k-1)}{2} \times \Delta T \tag{5.27}$$

$$\mathbf{\Delta u}_{cc}(k) = \frac{\mathbf{u}(k) + \mathbf{u}(k-1)}{2} \times \Delta T \tag{5.28}$$

where $G(k)$ is the cost to come of the parent node, $G(k+1)$ is the cost to come of the child node, and ΔG is the incremental state transition cost and is adapted from Equation 5.15. $\mathbf{\Delta x}(k)$ and $\mathbf{\Delta u}(k)$ both are calculated using trapezium area formula. Q and R are defined as,

$$\boldsymbol{Q} = \begin{bmatrix} \alpha_{Cost} & 0 & 0 & 0 & 0 \\ 0 & \beta_{Cost} & 0 & 0 & 0 \\ 0 & 0 & P_{Cost} & 0 & 0 \\ 0 & 0 & 0 & Q_{Cost} & 0 \\ 0 & 0 & 0 & 0 & R_{Cost} \end{bmatrix} \tag{5.29}$$

$$\boldsymbol{R} = \begin{bmatrix} \delta_{E_{Cost}} & 0 \\ 0 & \delta_{R_{Cost}} \end{bmatrix} \tag{5.30}$$

where $[]_{Cost}$ is the cost weighting applied for that specific state.

Cost To Go Heuristic

Similar to the deep stall recovery solution chapter the cost to go for each node is calculated using a heuristic function that estimates the cost of the cheapest path from the child node to a goal node. The equation is similar to that of deep stall in Section 4.5.5,

$$H(k+1) = \sqrt[2]{\boldsymbol{\Delta x}(k)_{cg}^{T} Q \boldsymbol{\Delta x}_{cg}(k)} + \sqrt[2]{\boldsymbol{\Delta u}_{cg}(k)^{T} R \boldsymbol{\Delta u}_{cg}(k)} \tag{5.31}$$

$$\boldsymbol{\Delta x}_{cg}(k) = \frac{\mathbf{x}(k) + \mathbf{x}_{goal}}{2} \times \Delta T \tag{5.32}$$

$$\boldsymbol{\Delta u}_{cg}(k) = \frac{\mathbf{u}(k) + \mathbf{u}_{trim}}{2} \times \Delta T \tag{5.33}$$

where $\mathbf{x}_{goal}$ is the goal state which is the centre of the goal region as defined in Section 5.3.7. $\mathbf{u}_{trim}$ is the trim settings for the control surfaces.

Total Path Cost

The total path cost for each node is the sum of its cost to come and its cost to go. This equation is defined in Section 4.5.6 and restated here,

$$J(k) \quad = \quad G(k) + H(k)$$

5.4.1 Optimal Trajectory Planning

The A^* trajectory planner was used to find the sequence of control actions and the associated state trajectory to recover the aircraft from a given initial state in the spin region. In Figure 5.2 the search tree diagram is shown which shows the different paths explored by the A^* algorithm.

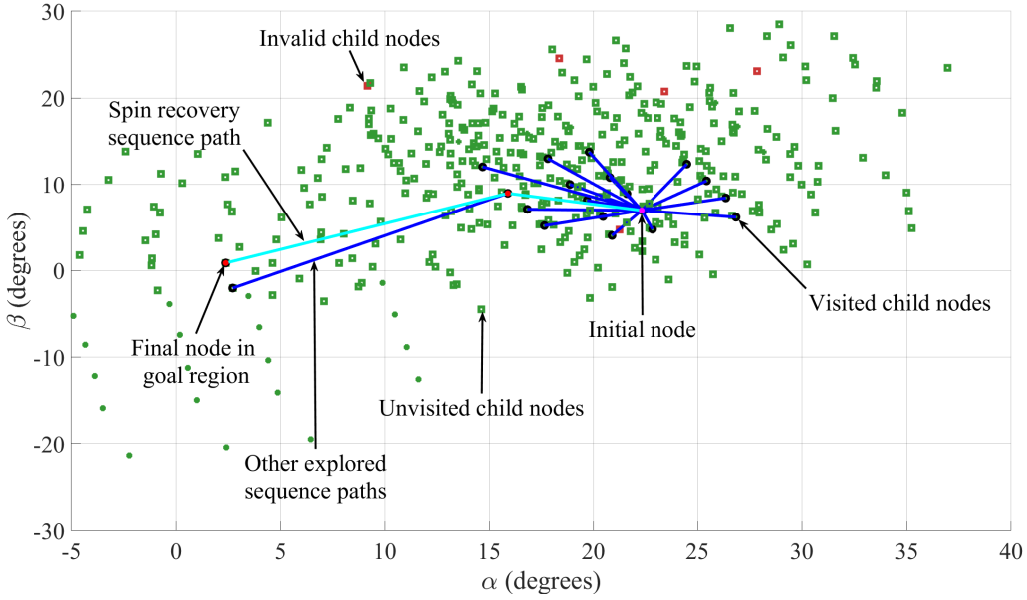

Figure 5.2: A^* trajectory planning to solve spin recovery sequence.

The planned sequence of control inputs and their expected spin recovery trajectory are shown in Fig. 5.3.

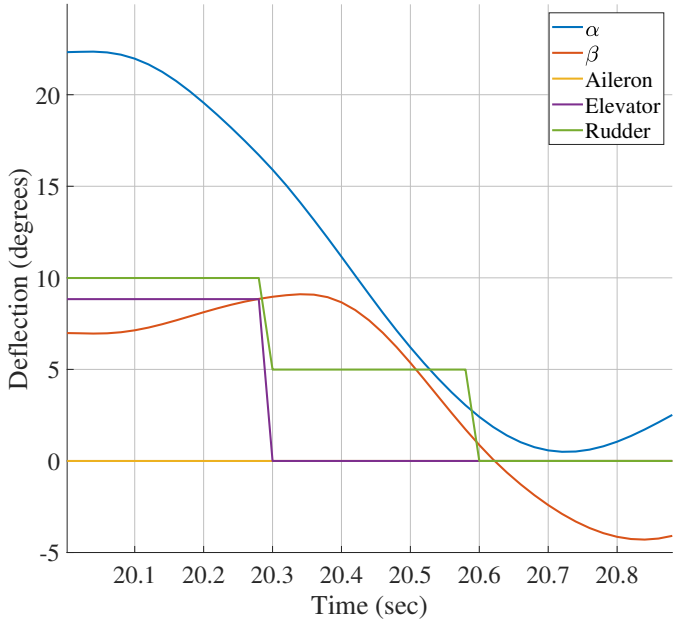

Figure 5.3: Planned spin recovery control actions and α, β trajectory using A*

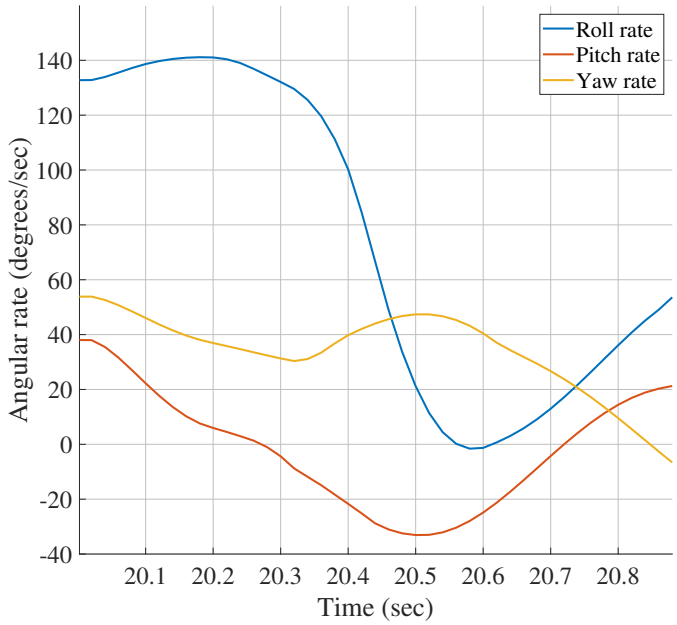

Figure 5.4: Planned spin recovery P, Q, R trajectory using A*

The initial spin state that was given to the optimal trajectory planner was obtained from the spin simulation performed with the full 6DoF GTM model in Section 3.2. The state at time $t = 20s$ in Figure 3.34, when the aircraft had already settled at the spin AoA and angular rates, was assumed to be the initial spin state from which the aircraft must be recovered.

The time histories in Fig. 5.3 show that the initial state of the aircraft at $t = 15s$ is an AoA of $\alpha = 38$ degrees, a sideslip angle of $\beta = 8$ degrees, roll rate of $P = 120$ degrees per

second, pitch rate of $Q = 0$ degrees per second, and a yaw rate of $R = -100$ degrees per second.

The planned sequence of recovery actions starts by simultaneously applying a rudder deflection $\delta_R = -30$ degrees and a nose-down elevator deflection $\delta_E = 20$ degrees. The rudder deflection causes the sideslip angle β to decrease from $\beta = 8$ to $\beta = 0$ degrees and the yaw rate to decrease from $R = -100$ to $R = 0$ degrees per second. The elevator deflection produces a negative pitching moment which increases from $Q = 0$ to $Q = -50$ degrees per second.

While the AoA, sideslip and angular rates recovers, the rudder deflection is reduced to $\delta_R = 15$ degrees and then to $\delta_R = 0$ degrees. When the AOA has been recovered to about $\alpha = 20$ degrees, the elevator deflection is set to $\delta_E = 10$ degrees to slow down the pitch rate to $Q = -20$ degrees per second. When the AoA drops below about $\alpha = 10$ degrees, the elevator deflection is returned to trim.

The aircraft has been recovered from the spin region, and the AoA returns to the trim AoA of $\alpha = 5$ degrees and the sideslip angle returns to zero degrees. This result is very pleasing, since it shows that the state trajectory and control inputs planned by the optimal trajectory planner agree with a typical prescribed spin recovery procedure that would be used by a human pilot as described in Section 2.1. This completes the section of the A* solution.

5.5 RRT Solution

The optimal control problem is also shown to be solved using the general RRT algorithm, shown in algorithm 2, described by [18]. The RRT algorithm is capable of exploring high-dimensional state spaces and are therefore ideal for working with the nine-dimensional state space of the 6DoF aircraft model.

Algorithm 2 Generic *RRT* Algorithm

L_{open}.insert(x_I)
while L_{open} not empty **and** size(L_{closed}) $< N_{\max}$ **do**
  $x_{\text{rand}} \leftarrow$ getRandom()
  $x_{\text{nearest}} \leftarrow L_{\text{open}}$.getNearest($x_{\text{rand}}$)
  for all $u \in U$ **do**
    $x' \leftarrow f(x_{\text{nearest}}, u)$
    if x' valid **then**
      $L_{\text{open}}.insert(x')$
      if $x' == x_G$ **then**
        return SUCCESS
  L_{closed}.insert(x_{nearest})
return FAILURE

The RRT algorithm starts at the initial state x_I also known as the starting node. The algorithm then selects at random a point with in the state space and searches for the nearest node which which is known to it within the state space. In the beginning this is the starting node. From this node it then generates all possible next states x' by applying

all possible actions u. These new states are saved as nodes along with a link to its parent node and the input action which generated its state. The algorithm then selects a new random point and iterates the previously explained actions.

This generates a tree of connected nodes which grows until a goal state is found. Once a goal state is found, the algorithm follows the trail of previous states to determine the path from the initial state to the goal state. This algorithm does not guarantee to find the optimal trajectory but does come close to optimal.

5.5.1 Algorithm Execution

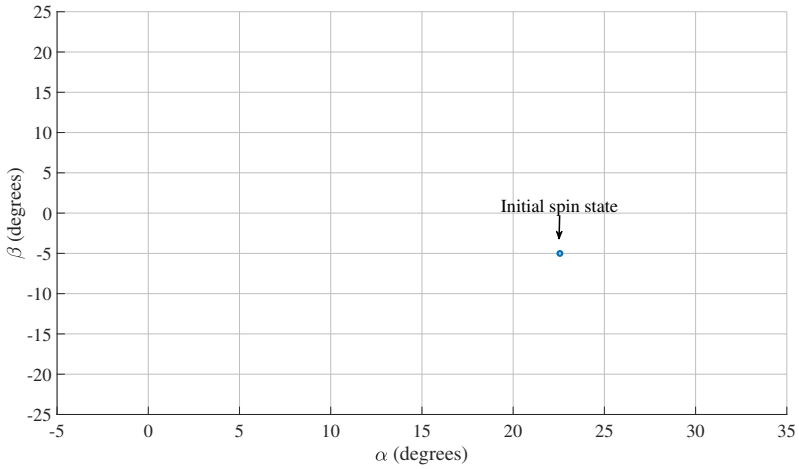

Figure 5.5: Initial setup for RRT spin recovery algorithm.

The RRT algorithm is initialised by populating the initial node states with the aircraft states while it is in a spin. The aircraft has a high AoA ($\alpha = 22.5°$) and a moderate sideslip angle of ($\beta = -5°$) in a developed spin and this is plotted in Figure 5.5 as the initial spin node.

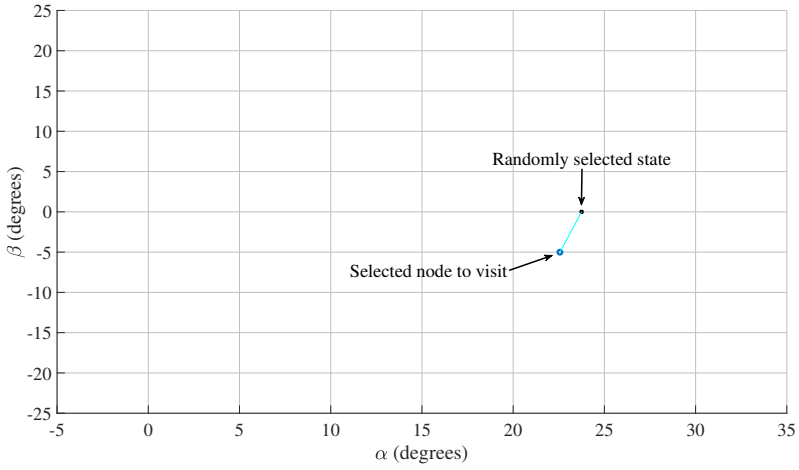

Figure 5.6: Random state generated and nearest node selected.

A random state is generated and the node which has the closest matching states according to the AoA and sideslip angle is then selected as the next node which the algorithm will visit. The selected node is linked to the randomly generated state by a light blue line.

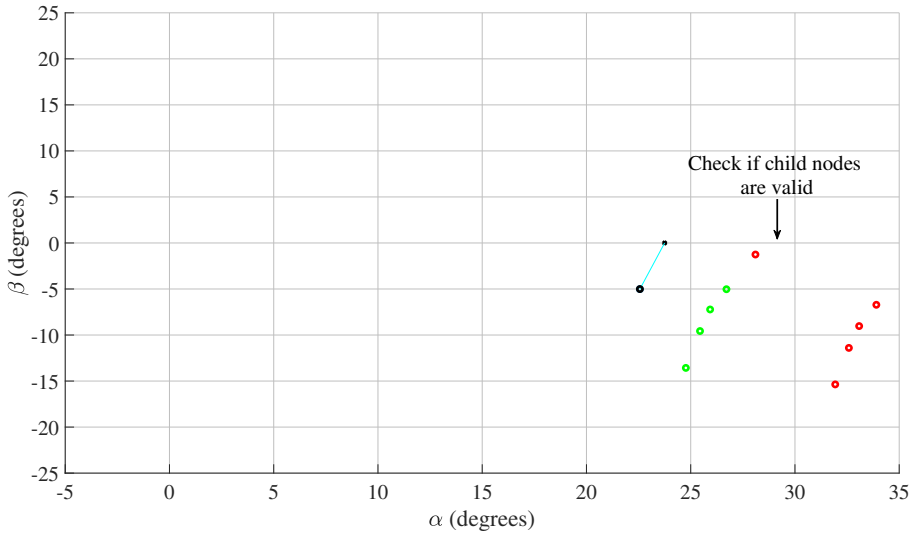

Figure 5.7: Child nodes calculated and state constraints checked.

This selected node is visited and new child nodes are generated by applying different combinations of control input actions to the selected node state and propagating the aircraft states for one time step ($Ts = 0.3s$) using the 6DoF model and thereby determine the new child node states.

Child node states which fall outside the specified state constraints are discarded and only the valid nodes are kept. Valid nodes that have not yet been visited are marked in green. Invalid nodes are marked in red. Valid child nodes are also check if they fall within the specified goal region. So far none of them do so and therefore the algorithm continues.

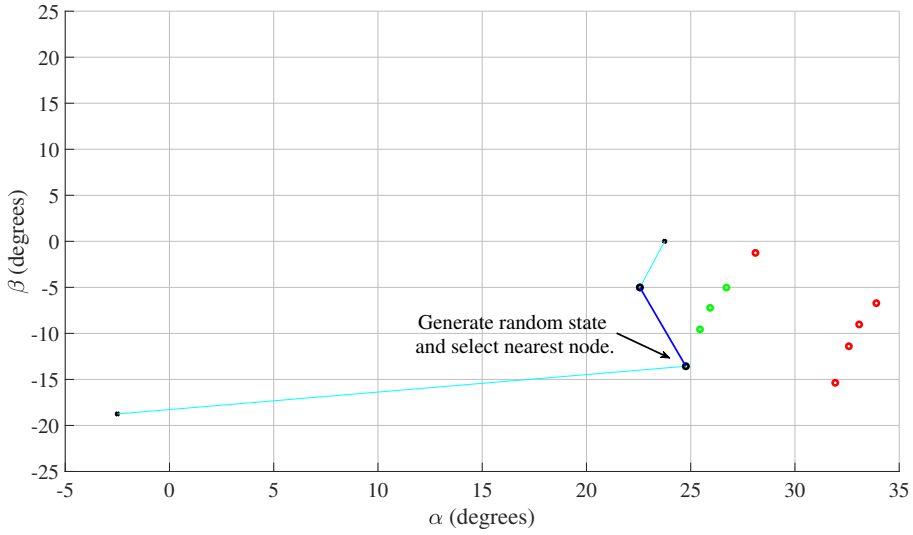

Figure 5.8: Next random state generated and valid unvisted state selected.

A new random state is generated and the nearest unvisited node is selected by the algorithm.

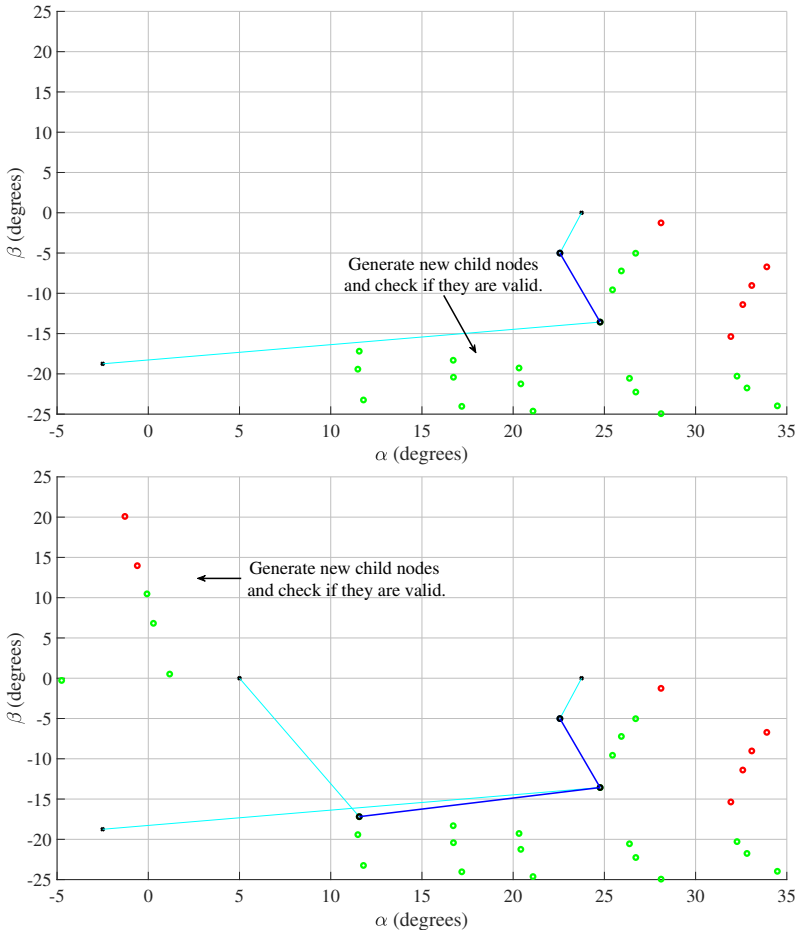

Figure 5.9: Number of iterations of the RRT spin recovery algorithm.

The newly selected node is visited and new child nodes are generated. Visited nodes are marked as black and are linked to their parent nodes by a dark blue line. The child nodes are checked if they are valid and if they fall within the goal region. This process continues until a child node is found to be within the specified goal region.

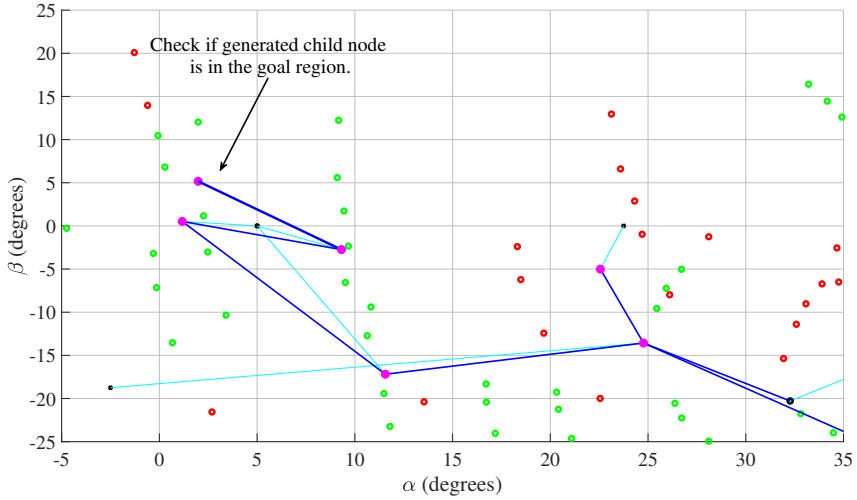

Figure 5.10: Goal region reached and spin recovery sequence noted.

The RRT algorithm terminates if a child node is found within the goal region, the algorithm

reaches the set maximum number of iterations, or if there are no valid unvisited child nodes are available. If a child node is found within the goal region the sequence to reach the child node is recorded as the spin recovery sequence. This sequence of nodes is marked using the colour magenta.

State Transition Equation

The following discrete-time, six-degrees-of-freedom model of the aircraft is used as the state transition equation to generate the child nodes from a given parent node

$$\begin{aligned} U(k+1) &= U(k) + \dot{U}(k)\Delta T \\ V(k+1) &= V(k) + \dot{V}(k)\Delta T \\ W(k+1) &= W(k) + \dot{W}(k)\Delta T \\ P(k+1) &= P(k) + \dot{P}(k)\Delta T \\ Q(k+1) &= Q(k) + \dot{Q}(k)\Delta T \\ R(k+1) &= R(k) + \dot{R}(k)\Delta T \\ \Phi(k+1) &= \Phi(k) + \dot{\Phi}(k)\Delta T \\ \Theta(k+1) &= \Theta(k) + \dot{\Theta}(k)\Delta T \\ H(k+1) &= H(k) + \dot{H}(k)\Delta T \end{aligned} \tag{5.34}$$

where k is the time index of the parent node, $k+1$ is the time index of the child node, ΔT is the sampling period of the discrete time step. The time derivatives $\dot{U}$, $\dot{V}$, $\dot{W}$, $\dot{P}$, $\dot{Q}$, $\dot{R}$, $\dot{\Phi}$, $\dot{\Theta}$, and $\dot{H}$ for a given set of inputs δ_A, δ_E, and δ_R are calculated using equations 3.2, 3.3, 3.7, and 3.10.

Action Space

The following discrete action space, consisting of a finite set of available elevator and rudder actions, is used to generate the child nodes from a given parent node.

$$\begin{aligned} \delta_A(k) &\in \{0\} \\ \delta_E(k) &\in \{-30, -20, -10, 0, +10, +20\} \\ \delta_R(k) &\in \{-30, -15, -5, 0, +5, +15, +30\} \end{aligned}$$

Input limiting was also applied to the RRT algorithm and was explained in the previous $A*$ solution section.

Choice of Sampling Period ΔT

As explained in the previous $A*$ solution section the time step size of $0.2s$ was implemented.

Random State Selection

The original RRT algorithm uses a completely random state selection process. This does find valid solutions but at the risk of having to explore regions of the state space which are of no interest.

To improve the convergence of the algorithm the random state is set to be within the goal state every second iteration of the algorithm. Another improvement is to use grid based selection of random states to guarantee that a uniform distribution of states are selected. The resolution of the grid will be chosen to provide the best algorithm performance.

5.5.2 Trajectory Planning: RRT

The optimal trajectory planner is used to find the sequence of control actions and the associated state trajectory to recover the aircraft from a given initial state in the spin region. The planned sequence of control inputs and their expected spin recovery trajectory are shown in Fig. 5.11.

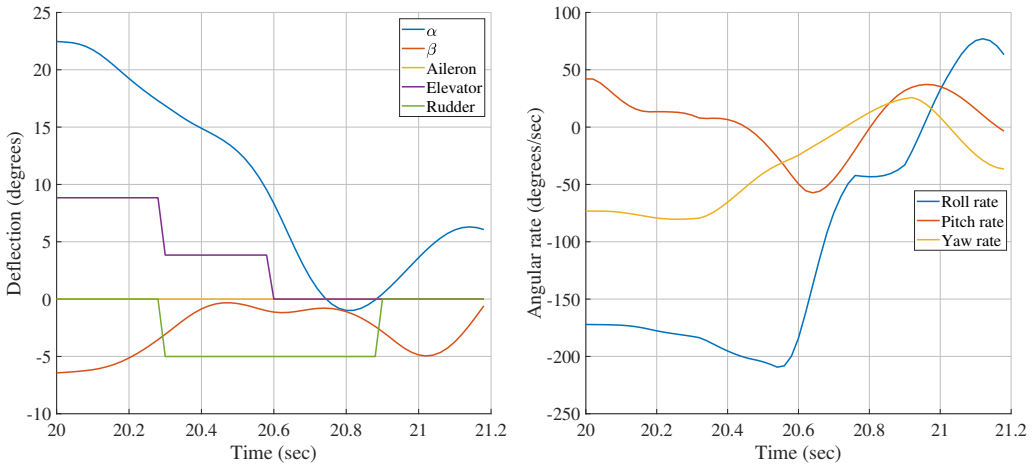

(a) (b)

Figure 5.11: Planned spin recovery actions and trajectory using RRT

The initial spin state that was given to the optimal trajectory planner was obtained from the spin simulation performed with the full 6DoF GTM model in Section 3.2. The state at time $t = 15s$ in Figure 3.34, when the aircraft had already settled at the spin AoA and angular rates, was assumed to be the initial spin state from which the aircraft must be recovered.

The time histories in Fig. 5.11 show that the initial state of the aircraft at $t = 15$ s is an AoA of $\alpha = 38$ degrees, a sideslip angle of $\beta = 8$ degrees, roll rate of $P = -120$ degrees per second, pitch rate of $Q = 0$ degrees per second, and a yaw rate of $R = -100$ degrees per second. This describes the conditions of a left spin.

The planned sequence of recovery actions starts by simultaneously applying a rudder deflection $\delta_R = -10$ degrees and a nose-up elevator deflection $\delta_E = -6$ degrees. After one time period the elevator is switched to a nose-down elevator deflection of $\delta_E = +4$ degrees. These actions cause the aircraft to pitch up and increase its AoA to $\alpha = 40$ degrees.

By combining the aircraft's tendency to return to an AOA of $\alpha = 38$ degrees and the downwards pitching moment of a nose-down elevator deflection of $\delta_E = +4$ degrees the aircraft generates enough downwards pitching momentum to escape the spin. The elevator deflection is increased to $\delta_E = +20$ degrees before it is gradually decreased to trim condition. The rudder deflection of $\delta_R = -10$ degrees reduces the sideslip angle from $\beta = 8$ degrees to $\beta = -3$ degrees. The rudder deflection is then reduced to $\delta_R = 0$ degrees as recover the sideslip angle to $\beta = 0$ degrees. The rudder is then deflected again to $\delta_R = -10$ degrees as to reduce the yaw rate to $R = 0$ degrees per second before being set back to trim.

This result are different to those of the A* algorithm but are still very pleasing, since they show that the state trajectory and control inputs planned by the RRT algorithm agree with a typical prescribed spin recovery procedure that would be used by a human pilot as described in Section 2.1.

5.6 Simulation Verification

The spin recovery actions that were planned using the 6DoF model in the previous Section 3.2 will now be applied to the full 6DoF NASA GTM simulation model to verify that the automatic spin recovery system can successfully recover the aircraft from spin.

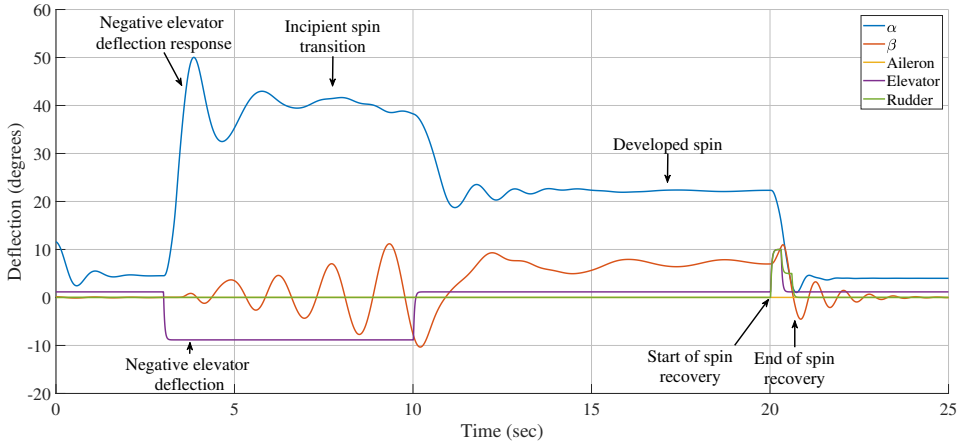

(a)

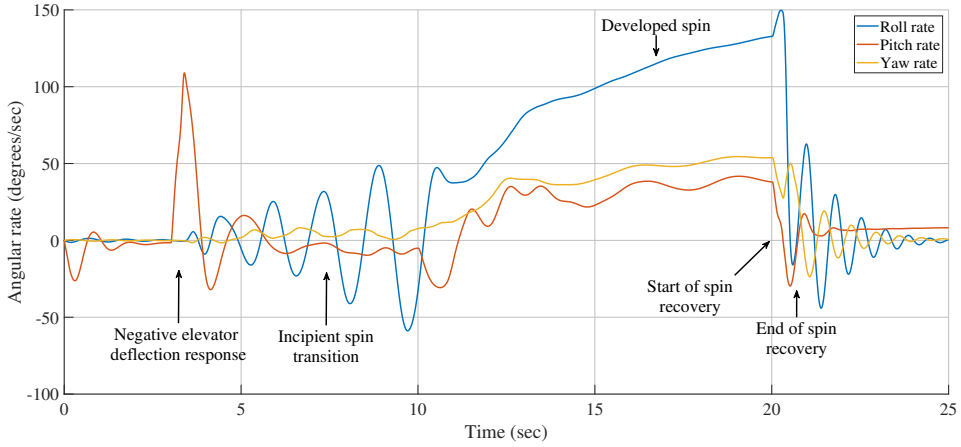

(b)

Figure 5.12: Simulated spin entry and successful recovery using A*

The simulation results for the A^* trajectory planning algorithm are shown in Fig. 5.12 and 5.14. The time histories of the AoA, sideslip angle, aileron, elevator, and rudder are shown in Fig. 5.12. The first part of the simulation, $t = (0s, 20s)$, follows a similar sequence as was performed in Fig. 3.34 to push the aircraft into Spin. However, this time the automatic spin recovery system is activated at $t = 20s$. The recovery system captures the aircraft state at that moment, plans the optimal sequence of recovery actions, and then executes the planned recovery actions on the aircraft.

The simulation results from time $t = (20s, 25s)$ show that the NASA GTM model is successfully recovered from spin to the normal aerodynamic envelope following a similar state trajectory to the planned state trajectory that was expected using the 6DoF model. After the recovery sequence, the aircraft settles to an AoA $\alpha = 5$ degrees and a sideslip angle $\beta = 0$ degrees inside the normal aerodynamic envelope.

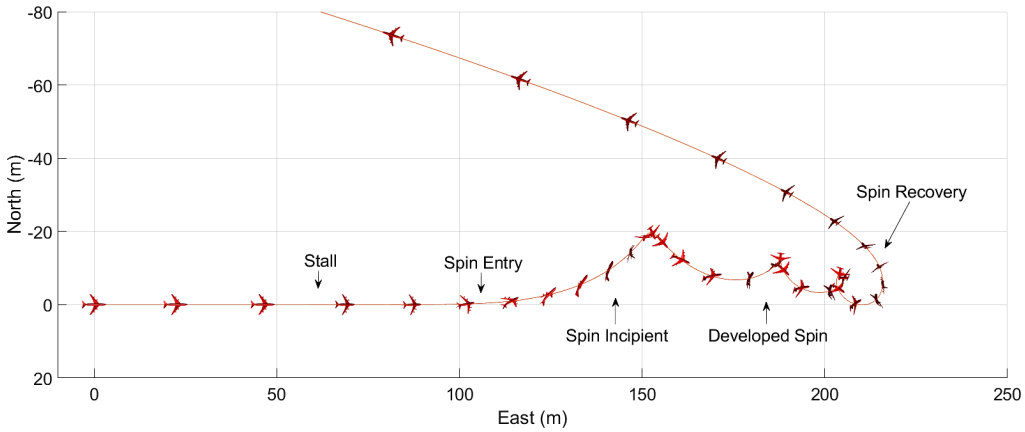

Figure 5.13: Spin entry and recovery trajectory using A* (top view).

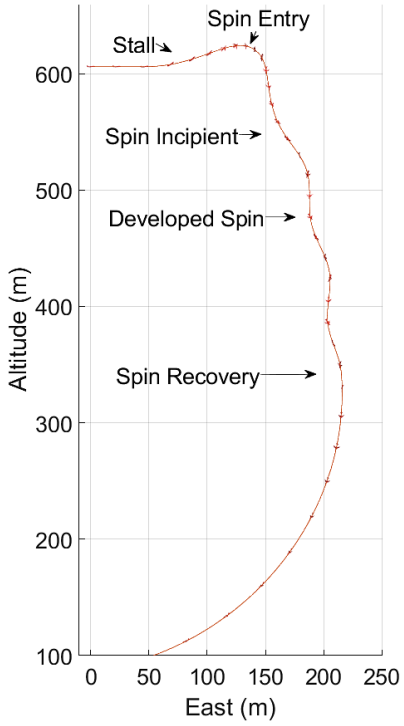

Figure 5.14: Spin entry and recovery trajectory using A* (side view).

The aircraft's trajectory during the spin entry and successful automatic recovery is shown in Fig. 5.14. The trajectory shows that after the spin recovery, the aircraft still has a nose-down pitch angle and a steeply descending flight path angle.

As mentioned before, the spin recovery is only concerned with recovering the aerodynamic envelope, so that the conventional flight control laws and envelope protection functions are available again to perform the next stage of the recovery sequence. Once the aircraft has been recovered from spin, a different upset recovery function can be engaged to perform the attitude, flight path angle and airspeed recovery.

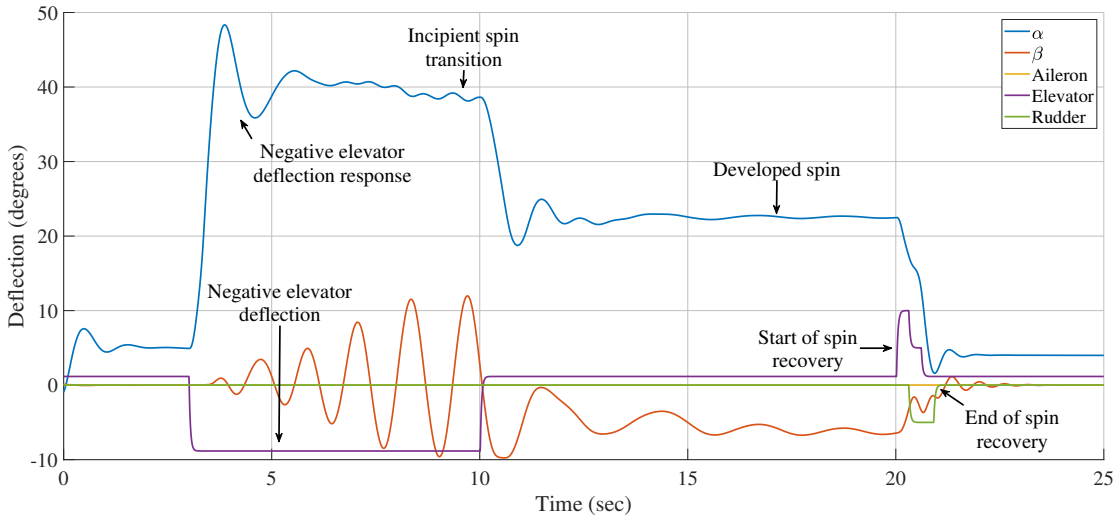

(a)

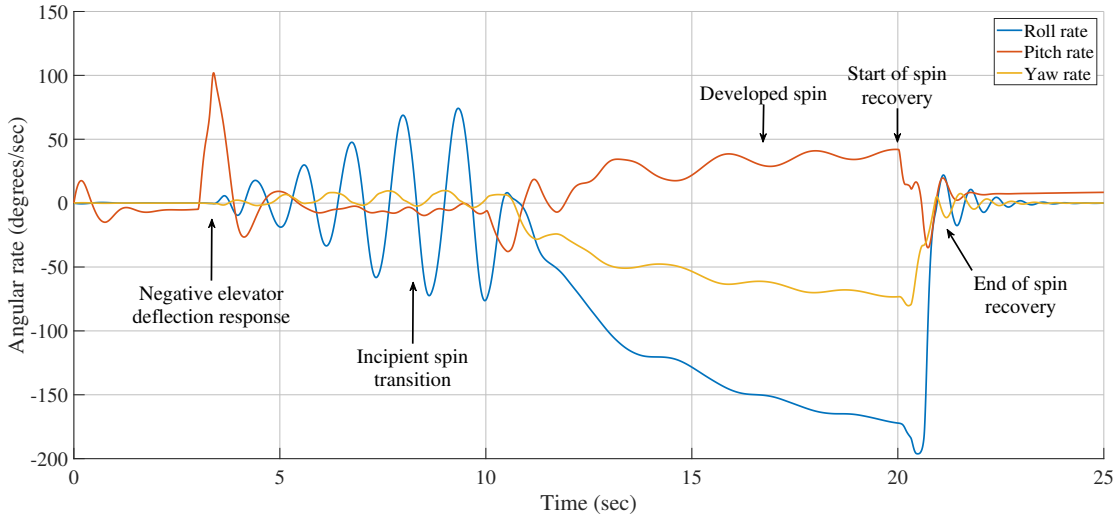

(b)

Figure 5.15: Simulated spin entry and successful recovery using RRT

The simulation results for the *RRT* trajectory planning algorithm are shown in Figure 5.15 and 5.16. The time histories of the AoA, sideslip angle, aileron, elevator, and rudder are shown in Fig. 5.15.

The first part of the simulation, $t = (0s, 20s)$, follows exactly the same sequence as was performed in Fig. 3.34 to push the aircraft into Spin. The automatic spin recovery system is activated at $t = 20s$. The recovery system captures the aircraft state at that moment, plans the optimal sequence of recovery actions using the *RRT* trajectory planning algorithm, and then executes the planned recovery actions on the aircraft.

The simulation results from time $t = (20s, 25s)$ show that the NASA GTM model is successfully recovered from spin to the normal aerodynamic envelope following a similar state trajectory to the planned state trajectory that was expected using the 6DoF model and the *RRT* trajectory planning algorithm.

After the recovery sequence, the aircraft settles to an AoA $\alpha = 5$ degrees and a sideslip angle $\beta = 0$ degrees inside the normal aerodynamic envelope. For this point on the normal flight control can take over and complete the flight-path angle, airspeed, altitude and orientation recovery.

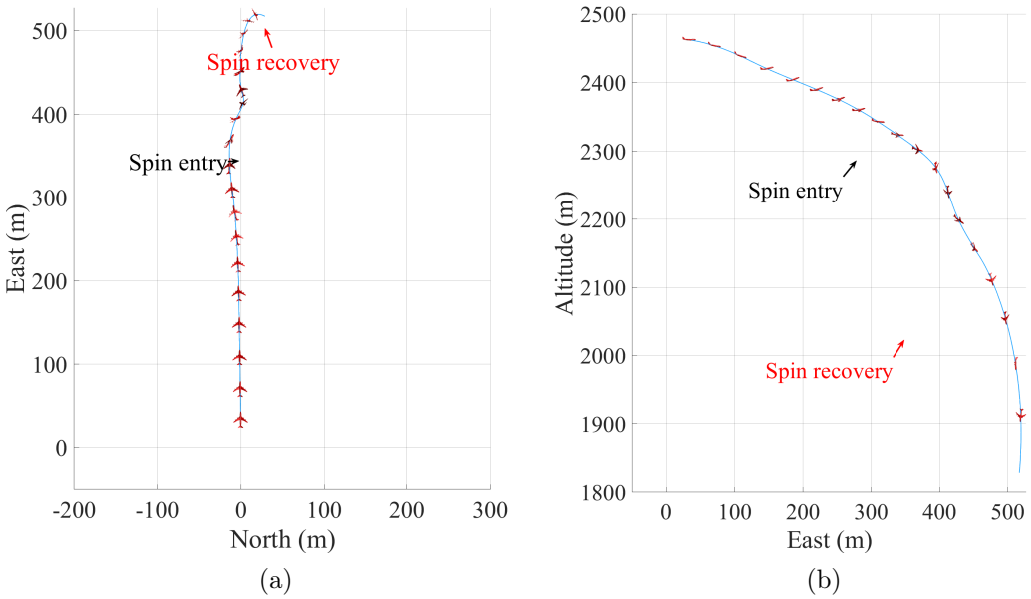

Figure 5.16: Spin entry and recovery trajectory using RRT (top view and side view).

5.7 Conclusion

In this chapter the spin recovery problem was solved using both an $A*$ and a RRT solution. An overview of how these algorithms are to be implemented into an actual aircraft control system was given and the optimal control problem of spin recovery was formulated. Both the $A*$ and the RRT spin recovery solutions were presented and an explanation of how these algorithms work was shown. The algorithms were verified in simulation by forcing the spin modified NASA GTM into a sustained spin, initialising the spin recovery algorithms with the developed spin states, calculating the recovery trajectories, and applying them to the NASA GTM to perform the spin recovery.

Chapter 6

Trajectory Regulation

In the previous chapters it was shown how the recovery trajectory and control input actions are planned. The control input actions can be applied directly to the control surfaces as an open-loop system or through a feedback control system as a closed-loop system. First, the open-loop and the closed-loop approaches are presented and both their strengths and weakness are noted. It will be explained as to why closed-loop control is chosen and how it was implemented in the form of linear-quadratic control.

Closed-loop control is used to improve the robustness of the recovery system against model uncertainty and other environmental effects. The implementation of closed-loop control for this recovery strategy enables the relaxation of the goal region constraints as specified in the Deep Stall and Spin recovery Chapters.

Second, a basic form of proportional angular rate damping is implemented to represent the normal flight control laws which would be present on any aircraft. The criteria to switch from the trajectory regulator as explained in the first part to the normal flight control will be defined. The gains of the proportional angular rate dampers were implemented using gain scheduling to take into consideration different air densities at different altitudes. A verification of this control switching and the angular rate dampers will be presented and discussed.

6.1 Open-Loop Trajectory Execution

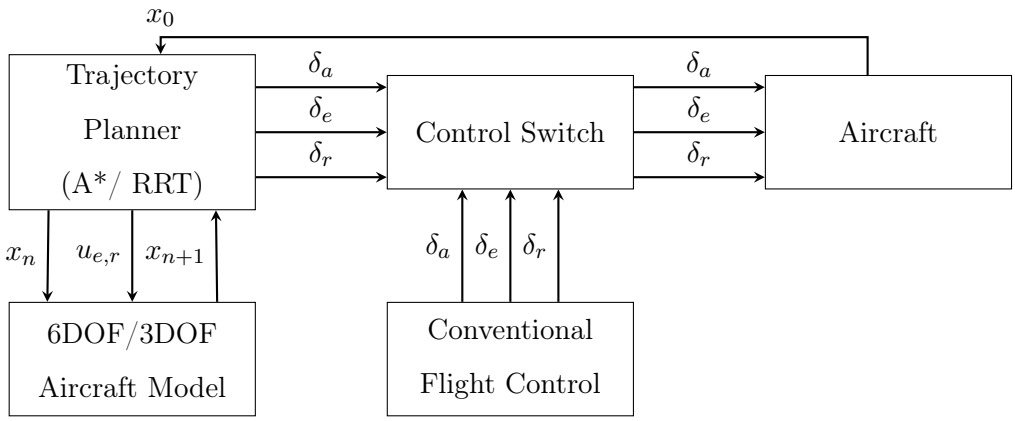

Figure 6.1: Open-loop implementation.

For the open-loop trajectory execution approach, the planned control surface deflection time-series are directly applied as the control signal to the control surfaces. The block diagram below represents the implementation. Due to not relying on feedback from sensors to monitor its current state the open-loop approach is not effected by sensor noise and inaccuracies. However the open-loop approach is vulnerable against external disturbances such as wind and turbulence. It also requires the 3DoF or 6DoF aircraft model which is used by the trajectory planner to be highly accurate because any model uncertainty will cause the aircraft to deviate from the planned recovery trajectory.

6.2 Closed-Loop Trajectory Execution

To address the short comings of the open-loop approach it was decided to implement a closed-loop approach. For the closed-loop trajectory execution approach a linear quadratic regulator is implemented. Because the recovery actions and the state trajectories are generated as discrete time signals with finite duration, the finite-horizon, discrete-time form of the Linear Quadratic Regulator (LQR) is used.

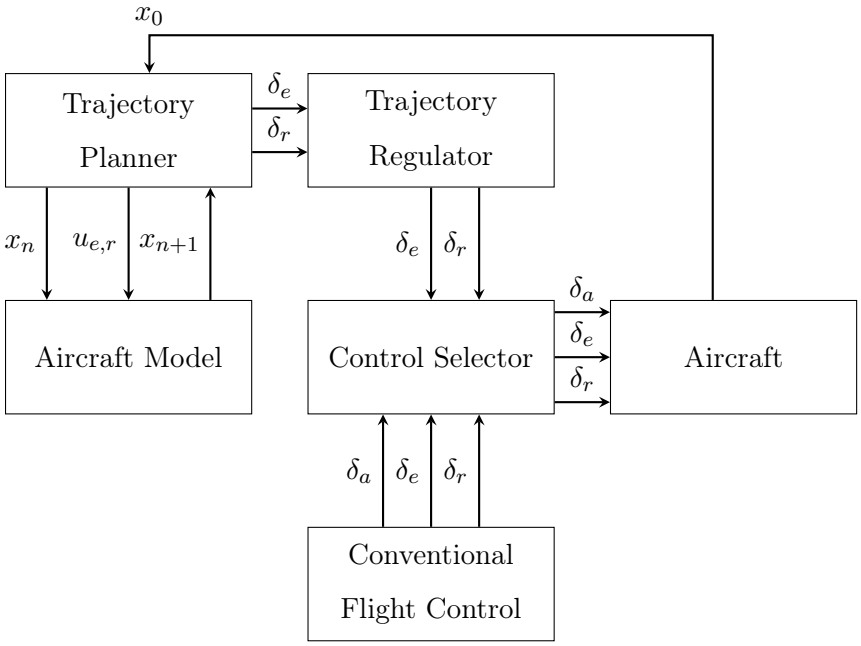

Figure 6.2: High level control system overview.

Figure 6.3 is a block diagram of the linear quadratic regulator. The aircraft dynamics are represented as a multiple-input multiple-output system,

$$\boldsymbol{x}(k+1) = F(k)\boldsymbol{x}(k) + G(k)\boldsymbol{u}(k) \tag{6.1}$$

where F is the discrete state-matrix and G is the discrete input matrix. The LQR control law is as follows,

$$\boldsymbol{u}_p(k) = -\boldsymbol{K}_{LQR}(k)\boldsymbol{x}_{\mathrm{p}}(k) \tag{6.2}$$

where $\boldsymbol{x}_{\mathrm{p}}(k)$ is the difference between the actual state of the aircraft and the planned trajectory state at time step k.

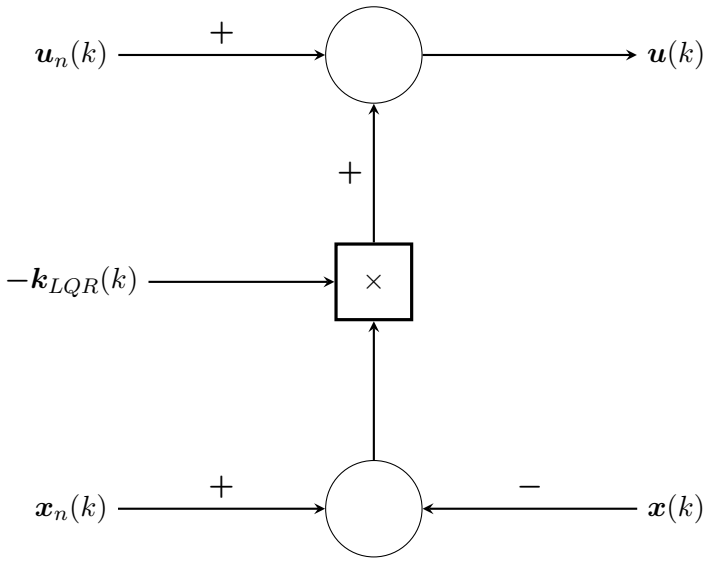

Figure 6.3: Trajectory regulator.

The LQR determines a set of gains to which minimises the following cost function,

$$J = \sum_{k=0}^{N} \boldsymbol{x}_{\mathrm{p}}(k)^T Q \boldsymbol{x}_{\mathrm{p}}(k) + \boldsymbol{u}_{\mathrm{p}}(k)^T R \boldsymbol{u}_{\mathrm{p}}(k) \tag{6.3}$$

The perturbation in the system states are calculated as

$$\boldsymbol{x}_{\mathrm{p}}(k) = \boldsymbol{x}(k) - \boldsymbol{x}_n(k) \tag{6.4}$$

where $\boldsymbol{x}(k)$ is the actual aircraft state and $\boldsymbol{x}_n(k)$ is the planned nominal trajectory state at time step k. The current control states are calculated as,

$$\boldsymbol{u}(k) = \boldsymbol{u}_{\mathrm{p}}(k) + \boldsymbol{u}_n(k) \tag{6.5}$$

where $\boldsymbol{u}_{\mathrm{p}}(k)$ is the current control perturbation calculated by the LQR control law and $\boldsymbol{u}_n(k)$ is the planned nominal control input at time step k. The system state cost matrix Q is chosen to be as follows,

$$\boldsymbol{Q} = \begin{bmatrix} 1/\alpha_{max}^2 & 0 & 0 & 0 & 0 \\ 0 & 1/\beta_{max}^2 & 0 & 0 & 0 \\ 0 & 0 & 1/P_{max}^2 & 0 & 0 \\ 0 & 0 & 0 & 1/Q_{max}^2 & 0 \\ 0 & 0 & 0 & 0 & 1/R_{max}^2 \end{bmatrix} \tag{6.6}$$

where α_{max}, β_{max}, P_{max}, Q_{max}, and R_{max} are the maximum allowed state deviations for each aircraft state from the planned trajectory. The control state cost matrix R is chosen to be as follows,

$$\boldsymbol{R} = \begin{bmatrix} 1/\delta_{E_{max}}^2 & 0 \\ 0 & 1/\delta_{R_{max}}^2 \end{bmatrix} \tag{6.7}$$

where $\delta_{E_{max}}$ and $\delta_{R_{max}}$ are the maximum allowed control state deviations from the planned control states. Bryson's rule scales the variables that appear in Equation 6.3 so that the maximum acceptable value for each term is 1 and this is used in determining the initial Q and R matrices. The optimal gain matrix K is calculated as follows,

$$\boldsymbol{K}_{LQR}(j) = [\boldsymbol{R} + \boldsymbol{G}^T \boldsymbol{S}(j+1)\boldsymbol{G}]^{-1} \boldsymbol{G}^T \boldsymbol{S}(j+1)\boldsymbol{F} \tag{6.8}$$

where $\boldsymbol{S}$ is calculated as,

$$\boldsymbol{S}(j) = \boldsymbol{F}^T \boldsymbol{M}(j+1)\boldsymbol{F} + \boldsymbol{Q} \tag{6.9}$$

and M is calculated as,

$$\boldsymbol{M}(j+1) = \boldsymbol{S}(j+1) - \boldsymbol{S}(j+1)\boldsymbol{G}[\boldsymbol{R} + \boldsymbol{G}^T \boldsymbol{S}(j+1)\boldsymbol{G}]^{-1}\boldsymbol{G}^T \boldsymbol{S}(j+1) \tag{6.10}$$

with the boundary conditions,

$$\boldsymbol{S}(N) = \boldsymbol{Q} \tag{6.11}$$

$$\boldsymbol{K}_{LQR}(N) = [\boldsymbol{0}_{5\times 2}] \tag{6.12}$$

and is solved recursively using the discrete Riccati equation. The gain matrix K is calculated for each time step along the recovery sequence. The transition from a high AoA state to a trim AoA state causes the aircraft dynamics to change significantly along the recovery sequence. For example the open-loop root locus plots of the transfer function which represents the AoA dynamics of the aircraft while at a high AoA ($\alpha = 22°$), that is represented in Figure 6.4a, drastically differ to the open-loop root locus plots at a trim AoA ($\alpha = 5°$) as shown in Figure 6.4b. The gain calculated to provide optimal control at a high AoA is therefore not optimal for control at trim AoA and therefore the optimal gain is calculated at each time step along the recovery sequence.

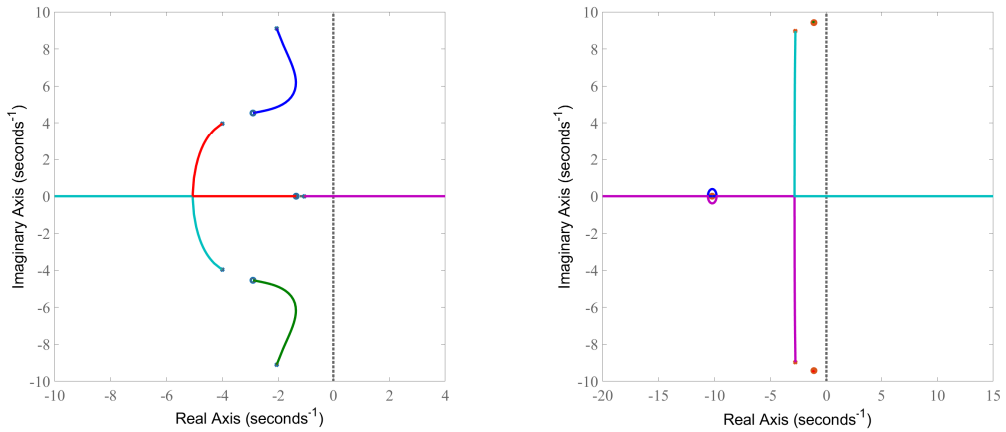

(a) Aircraft at a high AoA.

(b) Aircraft at trim AoA and wings level flight.

Figure 6.4: Aircraft AoA dynamics open-loop root locus.

6.2.1 Linear System Description

To obtain the state matrix $\boldsymbol{A}(k)$ and the control matrix $\boldsymbol{B}(k)$ for the NASA GTM with the states α, β, P, Q, and R the following was considered. The system matrix and the control matrix changes depending on the current states of the aircraft which means that the aircraft will react differently to a control input at a low AoA than how it would react at a high AoA. The system matrix and control matrix are linear descriptions of how a system will behave at an equilibrium point. By applying the small deviation theorems, it is possible to generate a number of system matrices and control matrices that describe the behaviour of the aircraft at specific equilibrium points. The small deviation theorems state that a nonlinear system will behave in a linear fashion if given a small deviation input. The system matrix and control matrix was generated from the 3DOF reduced-order model using the function $\boldsymbol{f_{3DOF}}(\boldsymbol{x}(k), \boldsymbol{u}(k))$. The state vector is defined as,

$$\mathbf{x}(k) = \begin{bmatrix} \alpha & \beta & P & Q & R \end{bmatrix}^T$$

where α and β are the AoA and sideslip angle, P, Q and R are the roll rate, pitch rate and yaw rate coordinated in the body axis system. The control input vector $\mathbf{u}$ is defined as

$$\mathbf{u}(k) = \begin{bmatrix} \delta_E & \delta_R \end{bmatrix}^T$$

where δ_E and δ_R are the elevator and rudder deflections. The state matrix $\boldsymbol{A}(k)$ is defined as follows,

$$\boldsymbol{A}(k) = \begin{bmatrix} \frac{\delta_\alpha(k)}{\delta_\alpha(k)} & \frac{\delta_\alpha(k)}{\delta_\beta(k)} & \frac{\delta_\alpha(k)}{\delta_P(k)} & \frac{\delta_\alpha(k)}{\delta_Q(k)} & \frac{\delta_\alpha(k)}{\delta_R(k)} \\ \frac{\delta_\beta(k)}{\delta_\alpha(k)} & \frac{\delta_\beta(k)}{\delta_\beta(k)} & \frac{\delta_\beta(k)}{\delta_P(k)} & \frac{\delta_\beta(k)}{\delta_Q(k)} & \frac{\delta_\beta(k)}{\delta_R(k)} \\ \frac{\delta_P(k)}{\delta_\alpha(k)} & \frac{\delta_P(k)}{\delta_\beta(k)} & \frac{\delta_P(k)}{\delta_P(k)} & \frac{\delta_P(k)}{\delta_Q(k)} & \frac{\delta_\alpha(k)}{\delta_R(k)} \\ \frac{\delta_Q(k)}{\delta_\alpha(k)} & \frac{\delta_Q(k)}{\delta_\beta(k)} & \frac{\delta_Q(k)}{\delta_P(k)} & \frac{\delta_Q(k)}{\delta_Q(k)} & \frac{\delta_Q(k)}{\delta_R(k)} \\ \frac{\delta_R(k)}{\delta_\alpha(k)} & \frac{\delta_R(k)}{\delta_\beta(k)} & \frac{\delta_R(k)}{\delta_P(k)} & \frac{\delta_R(k)}{\delta_Q(k)} & \frac{\delta_R(k)}{\delta_R(k)} \end{bmatrix} \tag{6.13}$$

and the control matrix $\boldsymbol{B}(k)$ is defined as follows,

$$\boldsymbol{B}(k) = \begin{bmatrix} \frac{\delta_\alpha(k)}{\delta_{\delta_E}(k)} & \frac{\delta_\alpha(k)}{\delta_{\delta_R}(k)} \\ \frac{\delta_\beta(k)}{\delta_{\delta_E}(k)} & \frac{\delta_\beta(k)}{\delta_{\delta_R}(k)} \\ \frac{\delta_P(k)}{\delta_{\delta_E}(k)} & \frac{\delta_P(k)}{\delta_{\delta_R}(k)} \\ \frac{\delta_Q(k)}{\delta_{\delta_E}(k)} & \frac{\delta_Q(k)}{\delta_{\delta_R}(k)} \\ \frac{\delta_R(k)}{\delta_{\delta_E}(k)} & \frac{\delta_R(k)}{\delta_{\delta_R}(k)} \end{bmatrix} \tag{6.14}$$

To obtain these matrices a small deviation will be applied to one of the variables and the resulting deviation in all the variables is recorded. The deviation in all the variables are then divided by the magnitude of the deviation that was applied to that one variable. This determines the linear response of variables due to a change in one of the variables. The mathematics of this approach will now be explained. The state equation is defined as,

$$\dot{\boldsymbol{x}}(k) = \boldsymbol{A}(k)\boldsymbol{x}(k) + \boldsymbol{B}(k)\boldsymbol{u}(k) \tag{6.15}$$

By adding a deviation, $\boldsymbol{\Delta_x}$, to the system state $\boldsymbol{x}(k)$ in equation 7.15 the following equation is derived,

$$\dot{\boldsymbol{x}}(k) + \boldsymbol{A}(k)\boldsymbol{\Delta_x} = \boldsymbol{A}(k)(\boldsymbol{x}(k) + \boldsymbol{\Delta_x}) + \boldsymbol{B}(k)\boldsymbol{u}(k) \tag{6.16}$$

and by adding a deviation, $\boldsymbol{\Delta_u}$, to the control state $\boldsymbol{u(k)}$ in equation 7.15 the following equation is derived,

$$\dot{\boldsymbol{x}}(k) + \boldsymbol{B}(k)\boldsymbol{\Delta_u} = \boldsymbol{A}(k)\boldsymbol{x}(k) + \boldsymbol{B}(k)(\boldsymbol{u}(k) + \boldsymbol{\Delta_u}) \tag{6.17}$$

The function $\boldsymbol{f_{3DOF}}(\boldsymbol{x}(k), \boldsymbol{u}(k))$ is based on the 3DOF aircraft model as described in Section 4.4 and is used to calculate the vector $\boldsymbol{\dot{x}(k)}$,

$$\dot{\boldsymbol{x}}(k) = \boldsymbol{f_{3DOF}}(\boldsymbol{x}(k), \boldsymbol{u}(k)) \tag{6.18}$$

By adding a deviation, $\boldsymbol{\Delta_x}$, to $\boldsymbol{x}(k)$ in equation 7.18,

$$\dot{\boldsymbol{x}}(k) + \boldsymbol{A}(k)\boldsymbol{\Delta_x} = \boldsymbol{f_{3DOF}}(\boldsymbol{x}(k) + \boldsymbol{\Delta_x}, \boldsymbol{u}(k)) \tag{6.19}$$

By adding a deviation, $\boldsymbol{\Delta_u}$, to $\boldsymbol{u}(k)$ in equation 7.18,

$$\dot{\boldsymbol{x}}(k) + \boldsymbol{B}(k)\boldsymbol{\Delta_u} = \boldsymbol{f_{3DOF}}(\boldsymbol{x}(k), \boldsymbol{u}(k) + \boldsymbol{\Delta_u}) \tag{6.20}$$

By subtracting a deviation, $\boldsymbol{\Delta_x}$, from $\boldsymbol{x}(k)$ in equation 7.18,

$$\dot{\boldsymbol{x}}(k) - \boldsymbol{A}(k)\boldsymbol{\Delta_x} = \boldsymbol{f_{3DOF}}(\boldsymbol{x}(k) - \boldsymbol{\Delta_x}, \boldsymbol{u}(k)) \tag{6.21}$$

By subtracting a deviation, $\boldsymbol{\Delta_u}$, from $\boldsymbol{u}(k)$ in equation 7.18,

$$\dot{\boldsymbol{x}}(k) - \boldsymbol{B}(k)\boldsymbol{\Delta_u} = \boldsymbol{f_{3DOF}}(\boldsymbol{x}(k), \boldsymbol{u}(k) - \boldsymbol{\Delta_u}) \tag{6.22}$$

The matrix $\boldsymbol{A}(k)$ is calculated by combining equation 7.19 and 7.21,

$$2\boldsymbol{A}(k)\boldsymbol{\Delta_x} = \boldsymbol{f_{3DOF}}(\boldsymbol{x}(k) + \boldsymbol{\Delta_x}, \boldsymbol{u}(k)) - \boldsymbol{f_{3DOF}}(\boldsymbol{x}(k) - \boldsymbol{\Delta_x}, \boldsymbol{u}(k)) \tag{6.23}$$

and by dividing both sides by two system state deviations, $2\boldsymbol{\Delta_x}$,

$$\boldsymbol{A}(k) = \frac{\boldsymbol{f_{3DOF}}(\boldsymbol{x}(k) + \boldsymbol{\Delta_x}, \boldsymbol{u}(k)) - \boldsymbol{f_{3DOF}}(\boldsymbol{x}(k) - \boldsymbol{\Delta_x}, \boldsymbol{u}(k))}{2\boldsymbol{\Delta_x}} \tag{6.24}$$

The matrix $\boldsymbol{B}(k)$ is calculated by combining equation 7.20 and 7.22,

$$2\boldsymbol{B}(k)\boldsymbol{\Delta_u} = \boldsymbol{f_{3DOF}}(\boldsymbol{x}(k), \boldsymbol{u}(k) + \boldsymbol{\Delta_u}) - \boldsymbol{f_{3DOF}}(\boldsymbol{x}(k), \boldsymbol{u}(k) - \boldsymbol{\Delta_u}) \tag{6.25}$$

and by dividing both sides by two control state deviations, $2\boldsymbol{\Delta_u}$,

$$\boldsymbol{B}(k) = \frac{\boldsymbol{f_{3DOF}}(\boldsymbol{x}(k), \boldsymbol{u}(k) + \boldsymbol{\Delta_u}) - \boldsymbol{f_{3DOF}}(\boldsymbol{x}(k), \boldsymbol{u}(k) - \boldsymbol{\Delta_u})}{2\boldsymbol{\Delta_u}} \tag{6.26}$$

If $\boldsymbol{\Delta_x}$ is defined as a one by five matrix,

$$\boldsymbol{\Delta_x} = \begin{bmatrix} \Delta_\alpha \\ \Delta_\beta \\ \Delta_P \\ \Delta_Q \\ \Delta_R \end{bmatrix} \tag{6.27}$$

and $\boldsymbol{\Delta_u}$ as a one by two matrix,

$$\boldsymbol{\Delta_u} = \begin{bmatrix} \Delta_{\delta_E} \\ \Delta_{\delta_R} \end{bmatrix} \tag{6.28}$$

By setting $\boldsymbol{\Delta_x}$ as follows,

$$\boldsymbol{\Delta_x} = \begin{bmatrix} \Delta_\alpha \\ 0 \\ 0 \\ 0 \\ 0 \end{bmatrix} \tag{6.29}$$

and naming it $\boldsymbol{\Delta_{x_\alpha}}$ and multiplying it with the state matrix $\boldsymbol{A}(k)$,

$$\begin{bmatrix} \frac{\delta_\alpha(k)}{\delta_\alpha(k)}\Delta_\alpha \\ \frac{\delta_\beta(k)}{\delta_\alpha(k)}\Delta_\alpha \\ \frac{\delta_P(k)}{\delta_\alpha(k)}\Delta_\alpha \\ \frac{\delta_Q(k)}{\delta_\alpha(k)}\Delta_\alpha \\ \frac{\delta_R(k)}{\delta_\alpha(k)}\Delta_\alpha \end{bmatrix} = \begin{bmatrix} \frac{\delta_\alpha(k)}{\delta_\alpha(k)} & \frac{\delta_\alpha(k)}{\delta_\beta(k)} & \frac{\delta_\alpha(k)}{\delta_P(k)} & \frac{\delta_\alpha(k)}{\delta_Q(k)} & \frac{\delta_\alpha(k)}{\delta_R(k)} \\ \frac{\delta_\beta(k)}{\delta_\alpha(k)} & \frac{\delta_\beta(k)}{\delta_\beta(k)} & \frac{\delta_\beta(k)}{\delta_P(k)} & \frac{\delta_\beta(k)}{\delta_Q(k)} & \frac{\delta_\beta(k)}{\delta_R(k)} \\ \frac{\delta_P(k)}{\delta_\alpha(k)} & \frac{\delta_P(k)}{\delta_\beta(k)} & \frac{\delta_P(k)}{\delta_P(k)} & \frac{\delta_P(k)}{\delta_Q(k)} & \frac{\delta_\alpha(k)}{\delta_R(k)} \\ \frac{\delta_Q(k)}{\delta_\alpha(k)} & \frac{\delta_Q(k)}{\delta_\beta(k)} & \frac{\delta_Q(k)}{\delta_P(k)} & \frac{\delta_Q(k)}{\delta_Q(k)} & \frac{\delta_Q(k)}{\delta_R(k)} \\ \frac{\delta_R(k)}{\delta_\alpha(k)} & \frac{\delta_R(k)}{\delta_\beta(k)} & \frac{\delta_R(k)}{\delta_P(k)} & \frac{\delta_R(k)}{\delta_Q(k)} & \frac{\delta_R(k)}{\delta_R(k)} \end{bmatrix} \begin{bmatrix} \Delta_\alpha \\ 0 \\ 0 \\ 0 \\ 0 \end{bmatrix} \tag{6.30}$$

by dividing the result by Δ_α,

$$\frac{\boldsymbol{A}(k)\boldsymbol{\Delta_{x_\alpha}}}{\Delta_\alpha} = \begin{bmatrix} \frac{\delta_\alpha(k)}{\delta_\alpha(k)} \\ \frac{\delta_\beta(k)}{\delta_\alpha(k)} \\ \frac{\delta_P(k)}{\delta_\alpha(k)} \\ \frac{\delta_Q(k)}{\delta_\alpha(k)} \\ \frac{\delta_R(k)}{\delta_\alpha(k)} \end{bmatrix} \tag{6.31}$$

yields the first column of the $\boldsymbol{A}(k)$ matrix. By setting $\boldsymbol{\Delta_x}$ as follows,

$$\boldsymbol{\Delta_x} = \begin{bmatrix} 0 \\ \Delta_\beta \\ 0 \\ 0 \\ 0 \end{bmatrix} \tag{6.32}$$

and naming it $\boldsymbol{\Delta}_{\boldsymbol{x}_\beta}$ and multiplying it with the state matrix $\boldsymbol{A}(k)$ and dividing by Δ_β,

$$\frac{\boldsymbol{A}(k)\boldsymbol{\Delta}_{\boldsymbol{x}_\beta}}{\Delta_\beta} = \begin{bmatrix} \frac{\delta_\alpha(k)}{\delta_\beta(k)} \\ \frac{\delta_\beta(k)}{\delta_\beta(k)} \\ \frac{\delta_P(k)}{\delta_\beta(k)} \\ \frac{\delta_Q(k)}{\delta_\beta(k)} \\ \frac{\delta_R(k)}{\delta_\beta(k)} \end{bmatrix} \tag{6.33}$$

yields the second column of the $\boldsymbol{A}(k)$ matrix. Therefore by iterating through the different $\boldsymbol{\Delta_x}$ configurations the whole state matrix $\boldsymbol{A}(k)$ is reconstructed. The same approach is used for the control matrix $\boldsymbol{B}(k)$. $\boldsymbol{\Delta_u}$ is set as,

$$\boldsymbol{\Delta_u} = \begin{bmatrix} \Delta_{\delta_E} \\ 0 \end{bmatrix} \tag{6.34}$$

and by naming it $\boldsymbol{\Delta}_{\boldsymbol{u}_{\delta_E}}$ and by multiplying it by $\boldsymbol{B}(k)$ and dividing by Δ_{δ_E},

$$\frac{\mathbf{B}(k)\boldsymbol{\Delta}_{\boldsymbol{u}_{\delta_E}}}{\Delta_{\delta_E}} = \begin{bmatrix} \frac{\delta_\alpha(k)}{\delta_{\delta_E}(k)} \\ \frac{\delta_\beta(k)}{\delta_{\delta_E}(k)} \\ \frac{\delta_P(k)}{\delta_{\delta_E}(k)} \\ \frac{\delta_Q(k)}{\delta_{\delta_E}(k)} \\ \frac{\delta_R(k)}{\delta_{\delta_E}(k)} \end{bmatrix} \tag{6.35}$$

yields the first column of the control matrix $\boldsymbol{B}(k)$. Therefore by iterating through the different $\boldsymbol{\Delta_u}$ configurations the whole control matrix $\boldsymbol{B}(k)$ is reconstructed. This completes the method used to calculate the state matrix $\boldsymbol{A}(k)$ and the control matrix $\boldsymbol{B}(k)$.

It is assume that the Linear Quadratic regulator has access to all the system states and therefore the output matrix C is defined as an identity matrix;

$$\mathbf{C}(k) = \begin{bmatrix} 1 & 0 & 0 & 0 & 0 \\ 0 & 1 & 0 & 0 & 0 \\ 0 & 0 & 1 & 0 & 0 \\ 0 & 0 & 0 & 1 & 0 \\ 0 & 0 & 0 & 0 & 1 \end{bmatrix} \tag{6.36}$$

which provides the full state feedback. There is no direct state feed-forward and therefore the feed-through matrix $D(k)$ is set to zero. These two matrices stay constant throughout all recoveries.

The state-matrix and the control-matrix are calculated at each time-step along the recovery trajectory. These matrices will be used to calculate the appropriate LQR gain for each time-step.

6.2.2 Discretization of Linear System

To use the continuous state and control-matrix calculated in the previous section it is necessary to discretize them. It is assumed that the control inputs are piecewise linear over the sample time T_s and therefore the triangle approximation, also known as the modified first order hold method is used to discretize the state and control-matrix. The built in $c2d$ function developed by MatLab was used to perform the discretization of the continuous system description to obtain the discrete system description.

6.3 Control Switch

At a certain point during each recovery the aircraft will return to its normal flight envelope, and the normal flight control laws, that were designed for the normal flight envelope, will be able to control the aircraft again and can then take over and perform rest of the recovery. A function is required to determine when the control of the aircraft can be transferred from the aircraft recovery system back to the normal flight control of the aircraft. Normal flight control is a well developed field of control and performs well in the linear flight state space. For the purposes of this research a basic rate damping controller will be implemented as the normal flight control. It will be demonstrated that this normal flight control is capable of returning the aircraft to wings level flight state from an envelope of different flight states. Other more sophisticated control could and should be implemented in place of this basic control.

6.3.1 Switching Criteria

The following design is based upon observation and the understanding of regions of attraction within the state space of aircraft. It is proposed that if the aircraft is within a specific flight envelope which is defined by the states α, β, P, Q, and R that the aircraft will always tend to return to the normal wings-level flight state. This observation is dependent on the aircraft model which is used and should be tested and determined for each different aircraft model. To determine the normal flight envelope for the NASA GTM with the basic rate damping control the following Monte-Carlo simulations were performed.

The following initial states will be varied: Airspeed, angular rates, altitude, aircraft mass, AoA, and sideslip angle. From the 6DoF equations in Section 3.2 it is noted that airspeed, and altitude have a direct relationship to the amount of force that is applied onto the aircraft due to dynamic pressure which is calculated using airspeed and air density which is dependent on altitude. The 6DoF equations also show that the angular rates are a good representation of the rotational inertia of the aircraft.

Large angular rates could result the aircraft to not damping to the wings level flight but instead to overshoot and result in the aircraft entering a different aerodynamic upset. It is important to test different AoA and sideslip initial states as relying alone on the angular rates could result in a state of low angular rates and sideslip angle but with a high AoA. This is representative of a deep stall and therefore the normal flight control did not return the aircraft to normal wing-level flight even though the angular rates criteria is met. The Table 6.1 describes the range for each initial state; These ranges are the admissible states for which the NASA GTM aerodynamic model is valid and were defined by [5] Section 3B. The NASA GTM will be run for 10 seconds starting with a random set of initial states which are within the above defined ranges.

The period of 10 seconds is deemed long enough for the normal flight rate damping control to settle the aircraft to the trim AOA and sideslip angle. For each iteration of the Monte-Carlo simulation the time series of each state is recorded and later on analysed to

State	Minimum	Maximum
AoA	-5°	50°
Sideslip angle	-45°	45°
Roll Rate	-200°/s	200°/s
Pitch Rate	-80°/s	80°/s
Yaw Rate	-90°/s	90°/s
Altitude	0ft	45000ft
Air Speed .	16ft/s	300ft/s

Table 6.1: Switch test state ranges

determine if the the aircraft stayed within the structural flight envelope as shown in Table 4.9 which is shown again below for reference;

$$\begin{aligned} \alpha(t) &\in [-5^\circ, +60^\circ] \\ \beta(t) &\in [-45^\circ, +45^\circ] \\ P(t) &\in [-200^\circ/s, +200^\circ/s] \\ Q(t) &\in [-80^\circ/s, +80^\circ/s] \\ R(t) &\in [-90^\circ/s, +90^\circ/s] \end{aligned}$$

If none of the above state constraints are exceeded during the 10 seconds of simulation and if at the end of the simulation the AoA, sideslip angle and angular rates are close to their trim values, it is deemed that the rate damping control was capable of returning the aircraft to normal trim flight. Table 6.37 below shows the aircraft state ranges for normal trim flight for the GTM:

$$\begin{aligned} \alpha(t=10) &\in [+2^\circ, +6^\circ] \\ \beta(t=10) &\in [-4^\circ, +4^\circ] \\ P(t=10) &\in [-10^\circ/s, +10^\circ/s] \\ Q(t=10) &\in [-5^\circ/s, +5^\circ/s] \\ R(t=10) &\in [-5^\circ/s, +5]^\circ/s \end{aligned}$$

A batch of 10000 simulations was run and then automatically analysed to determine if the aircraft exceeded the state constraints. If it was found that the aircraft did exceed the state constraints then the initial state ranges as shown in Table 6.1 where reduced using a trail and error approach. This iterative adjustment of the set of initial state ranges was done until a set of initial state ranges were found for which the batch of 10000 simulations did not exceed the state constraints and met the end criteria as described by Table 6.37. Below is the table of the initial state ranges which were determined:

Each batch of simulations were analysed and certain observations were made. It was noted that if the aircraft was at a low airspeed combined with positive pitch angle θ it is very likely to stall and enter a deep stall. This fits well with the understanding that a stall is caused either due to a AoA which is greater than the specified critical AoA or that there is insufficient airflow across the main wings.

State	Minimum	Maximum
AoA	-5°	18°
Sideslip angle	-15°	15°
Roll Rate	-150°/s	150°/s
Pitch Rate	-80°/s	0°/s
Yaw Rate	-70°/s	70°/s
Altitude	500ft	45000ft
Airspeed	67ft/s	278ft/s

Table 6.2: Switch test state ranges

6.4 Proportional Rate Damping Control

For the normal flight control a rate damping controller was implemented. This control is only focused on reducing the angular rates to zero. For each angular axis a rate damping controller was added which uses the basic proportional gain control law.

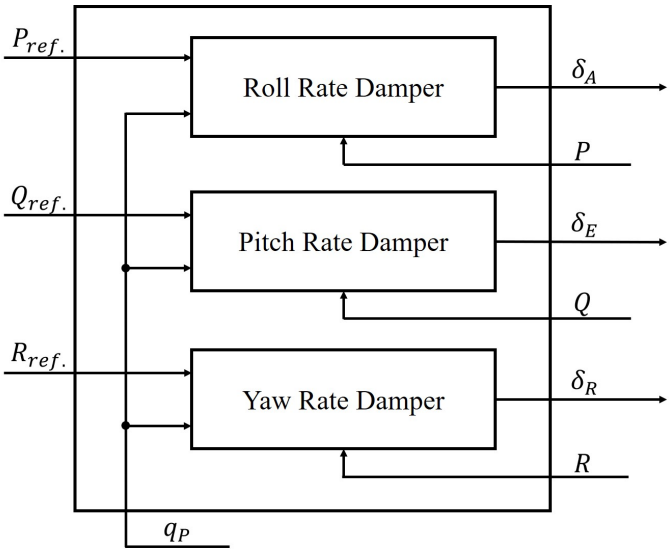

Figure 6.5: Normal flight control high level overview

The respective control surface for the respective angular axis is set to a degree of deflection which is proportional to that angular axis' angular rate. The effectiveness of the control surfaces is directly dependent on the dynamic pressure which is present at the current state of the aircraft. Dynamic pressure is a function of the airspeed and altitude of the aircraft. To address this change in dynamics at different states, gain scheduling was implemented. Gain scheduling is implemented by looking up the proportional gain for the rate damper from a piece-wise linear graph where the gain is a function of the dynamic pressure experienced by the aircraft. This graph was developed by calculating a stable proportional gain at different dynamic pressures and then linking these gains linearly using linear interpolation.

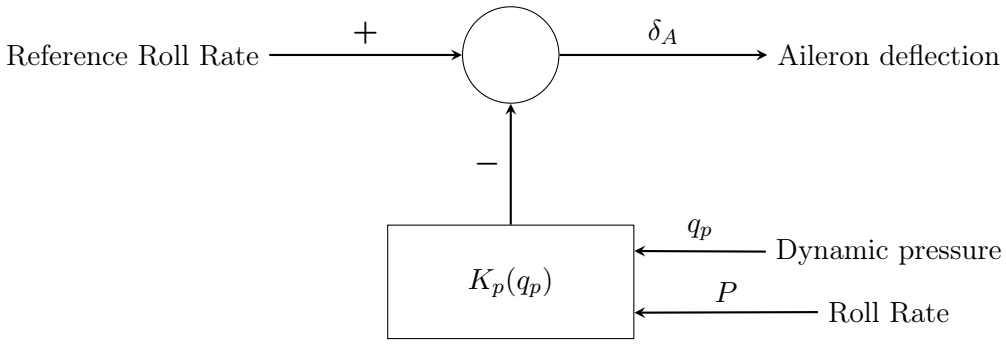

Figure 6.6: Roll rate damper

Figure 6.6 shows the structure of the roll rate damper which damps the roll rate of the aircraft by controlling the aileron control surface. The gain $K_p(q_p)$ is a function of dynamic pressure q_p and the graph of the function is shown in Figure 6.7

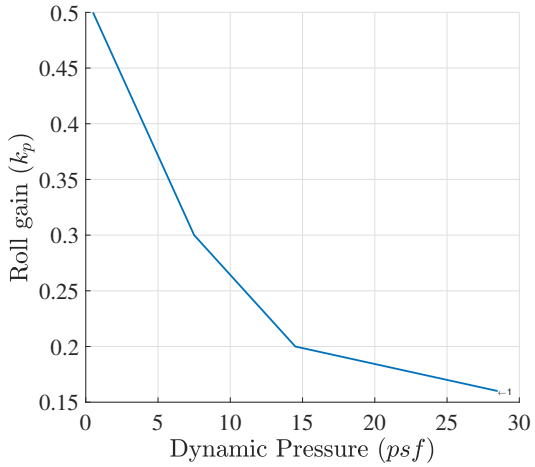

Figure 6.7: Roll rate damper gain schedule

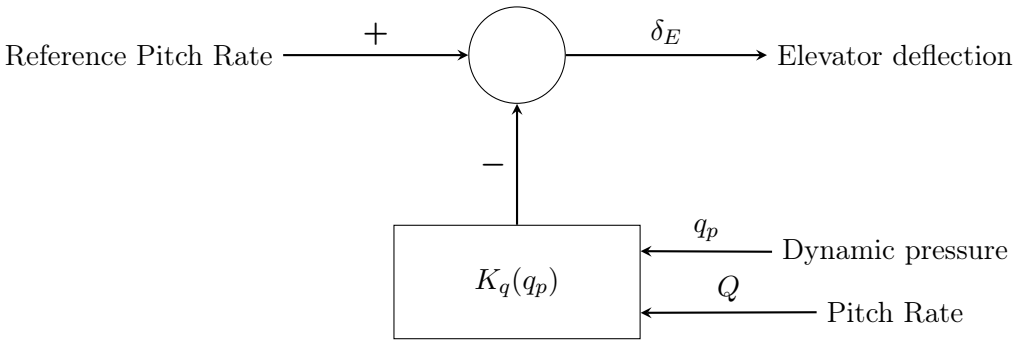

Figure 6.8: Pitch rate damper

Figure 6.8 shows the structure of the pitch rate damper which damps the pitch rate of the aircraft by controlling the elevator control surface. The gain $K_q(q_p)$ is a function of dynamic pressure q_p and the graph of the function is shown in Figure 6.9

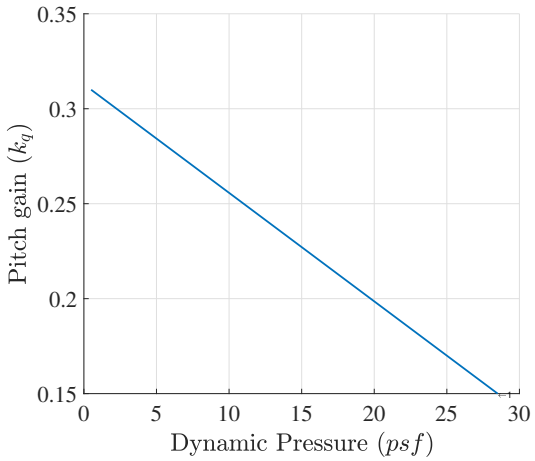

Figure 6.9: Pitch rate damper gain schedule

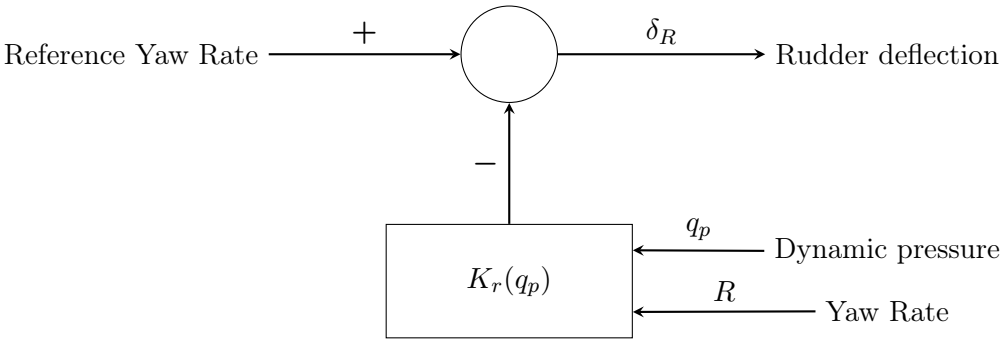

Figure 6.10: Yaw rate damper

Figure 6.10 shows the structure of the yaw rate damper which damps the yaw rate of the aircraft by controlling the rudder control surface. The gain $K_r(q_p)$ is a function of dynamic pressure q_p and the graph of the function is shown in Figure 6.11

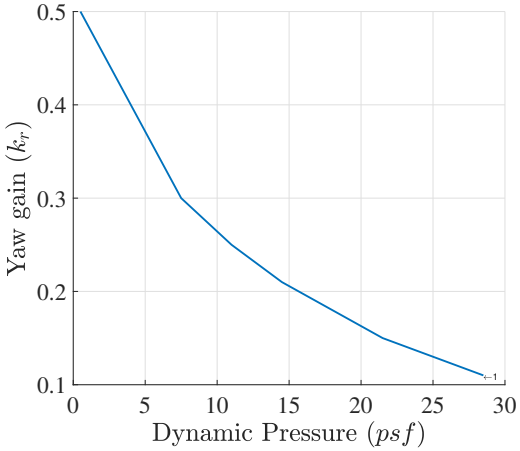

Figure 6.11: Yaw rate damper gain schedule

6.5 Conclusion

This concludes the trajectory regulator chapter. The implementation of an open-loop system was discussed and the reasons for the use of a closed-loop system were explained. For the closed-loop approach, a linear quadratic regulator was presented for which the optimal gain is calculated according to the cost weighting matrix. By multiplying this gain with the deviation of the aircraft trajectory from the planned trajectory one determines the control deflection necessary for the elevator and rudder control surfaces in order to correct the aircraft's trajectory.

It was discussed how the aircraft will switch from flight recovery control to normal flight control and determined the safe switching state ranges. A basic form of angular rate damping was implemented to represent the conventional flight control. In the following chapter the flight recovery system will be verified.

Chapter 7

Verification and Testing

In this chapter the ability of the stall and spin recovery system to recover an aircraft from random deep stall and spin conditions is tested. The robustness of the system to model uncertainty and external disturbances is also verified. Monte Carlo simulations are performed with random initial states, random variations in the aircraft model parameters, and random external wind disturbances. To test the robustness of the system to model uncertainty, the trajectory planner is given a set of nominal aircraft model parameters whereas the simulations are performed using varying aircraft model parameters that are randomly sampled from the uncertainty set.

The performance of the stall and spin recovery systems will be evaluate according to these parameters: the recovery success rate, the number of nodes searched to find a solution, the total duration of the recovery, and the total altitude lost during the recovery. Next the execution of the stall and spin recovery trajectories are tested using four different configurations, open-loop execution, open-loop execution with control switching, closed-loop execution, and closed-loop execution with control switching. The results of the four different configurations are evaluated and compared. Finally, the recovery control action sequences calculated by the trajectory planner are analysed to determine whether they suggest standard procedures for deep stall and spin recovery.

7.1 Monte Carlo Method

The Monte Carlo method performs a large number of repeated simulations with randomised parameters and initial conditions to obtain the distribution of the resulting trajectories, which can then be statistically analysed. Firstly the domains of initial states are defined and then the random initial states are generated from a probability distribution over the domains. Using these initial states the simulations are run and the results recorded. Finally the results are analysed and observations and conclusions are made. By performing a sufficiently large number of simulations that cover the domains of the model parameter and initial conditions, the system performance can be evaluated statistically.

7.1.1 Random Initial States

The Monte Carlo simulations were performed for the fixed aircraft trim setting shown in Table 7.1, and using random initial aircraft states that were sampled uniformly from the ranges shown in Table 7.2.

State	Value	Unit	Description
Trim AoA	5.0	degrees	The AoA for which the aircraft is trimmed.
Trim Airspeed	126.6	feet/sec.	The airspeed for which the aircraft is trimmed.
Trim Heading	0.0	degrees	The heading for which the aircraft is trimmed.

Table 7.1: Aircraft trim settings

Random Initial States

The following initial states were randomly sampled from the defined state domains. These states can be set to any value between the maximum and minimum values shown for each specific state in the table below.

State	Min	Max	Unit	Description
Air Speed	67	337	*ft/s*	The air speed of the aircraft at the initialisation of the simulation.
Altitude	4000	45000	*ft*	The altitude of the aircraft at the initialisation of the simulation.
Initial AoA	-3	15	*deg*	The AoA of the aircraft at the initialisation of the simulation.
Wind Speed	0	125	*ft/s*	The wind speed during the simulation.
Wind Direction	0	360	*deg*	The wind direction during the simulation.

Table 7.2: Random initial states domains.

States such as, sideslip angle (β), roll, pitch and yaw angle (ϕ, θ, ψ), roll, pitch and yaw rates (p, q, r), and flight path angle (γ) were all initialised for wings-level flight.

External Disturbances

The flight recovery system must be robust to external disturbances such as wind, wind gusts, turbulence and wind sheer. Wind is set as a variable state and is set at the beginning of each simulation instance. Wind gusts and sheer are enforced as soon as the flight recovery is being performed by the trajectory regulator. This will ensure that the trajectory planner has no prior knowledge of the oncoming disturbance.

Wind gusts are a brief change in airspeed usually with a magnitude of 12 ft/s. A strong wind gust has a magnitude of 20 ft/s. Wind shear, also known as a wind gradient, is a sudden change in wind speed and direction and is categorised as having a change of airspeed of usually 30ft/s to 40 ft/s.

To model this, the built-in wind gust and shear models which generate the appropriate airspeed vector were used. For wind gusts, an amplitude of 20 ft/s was set and the length of the gust was set to generate the maximum excitation of the natural modes of the NASA GTM. For wind shear an amplitude of 35 ft/s is set and the direction of the wind shear is set to be 90 deg to the direction of the current wind vector.

Turbulence experienced by aircraft is described to cause violent buffeting of the aircraft similar to hitting bumps in the road while driving. In aviation, turbulence is known as clear-air turbulence (CAT). For the simulation tests, the Dryden turbulence model was used which is based on the MILS-F-8785 specifications[7].

Aircraft Model

To verify the robustness of the stall and spin recovery system; it is not given the exact randomly selected aircraft model instance which is being simulated. For example the aircraft's actual mass in simulation is varied between its minimum and maximum value but the recovery system is given a fixed nominal mass value of $82lbs$.

The aerodynamic coefficient functions are also randomly varied in the simulation, but the recovery system uses the nominal aerodynamic model for the trajectory planning and the feedback controller design. Table 7.3 lists all states which differ between the simulated aircraft model and the nominal aircraft model which the trajectory planner uses to determine a recovery solution.

Parameter	**Min**	**Max**	**Nominal**	**Description**
$C_{M_{Static}\delta_E}(\alpha)$	$(10°, 35°)$	$(14°, 35°)$	$[12°, 35°]$	The AoA range wherein the effectiveness of the elevator is reduced.
$C_{M_{Static}\delta_E}(\beta)$	$[-2°, 2°]$	$[-6°, 6°]$	$[-4°, 4°]$	The sideslip angle range wherein the effectiveness of the elevator is reduced.
$C_{M_{Static}\delta_E}$	0%	20%	10%	The percentage of effectiveness of the elevator in the reduced effectiveness area.
$Mass$	52lbs	112lbs	82lbs	The mass of the aircraft.
$C_{N_{Static}\delta_R}(\alpha)$	$[10°, 35°]$	$[14°, 35°]$	$[12°, 35°]$	The AoA range wherein the effectiveness of the rudder is reduced.
$C_{N_{Static}\delta_R}(\beta)$	$[-2°, 2°]$	$[-4°, 4°]$	$[-4°, 4°]$	The sideslip angle range wherein the effectiveness of the rudder is reduced.
$C_{N_{Static}\delta_R}$	70%	100%	85%	The percentage of effectiveness of the rudder in the reduced effectiveness area.

Table 7.3: Aircraft simulation states and fixed controller states.

7.1.2 Random Input State Generation

The variable states which are described in Section 7.1.1 are sampled from a uniform distribution so that all of the values in the range have an equal chance of being sampled. The uniform distribution is described by the following probability density function where a is the minimum value and b is the maximum value for the specific variable state as defined in Tables 7.2 and 7.3.

$$f(x) = \begin{cases} \frac{1}{b-a} & \text{for } a \leq x \leq b \\ 0 & \text{for } x < a \text{ or } x > b \end{cases} \tag{7.1}$$

7.1.3 Recovery Criteria

The following requirements in Table 7.4 are defined as our output state tests for the Monte Carlo method which determine if a recovery is successful or not. These ranges were defined in [5] as an analysis method to determine the effectiveness of control strategies for the recovery of aircraft in flight upset conditions.

Requirement	State	Time period	Min.	Max.	Description
Structural loading	Load factor	Ti:Tf	-2gs	2gs	The acceleration of the aircraft needs to be below the loading limit of the fuselage.
Admissible roll rate	Roll rate	Ti:Tf	-200 deg/s	200 deg/s	Range of allowable roll rate to ensure safe recovery.
Admissible pitch rate	Pitch rate	Ti:Tf	-80 deg/s	80 deg/s	Range of allowable pitch rate to ensure safe recovery.
Admissible yaw rate	Yaw rate	Ti:Tf	-90 deg/s	90 deg/s	Range of allowable yaw rate to ensure safe recovery.
Admissible AoA	AoA	Ti:Tf	-5 deg	50 deg	Range of allowable AoA to ensure safe recovery.
Admissible sideslip	Sideslip	Ti:Tf	-30 deg	30 deg	Range of allowable sideslip to ensure safe recovery.
Admissible airspeed	Airspeed	Ti:Tf	67 ft/s	337 ft/s	Range of allowable airspeed to ensure safe recovery.
Admissible altitude loss	Altitude loss	Ti:Tf	0 ft	1500 ft	Range of allowable altitude loss which is acceptable.
Final roll rate	Roll rate	Tf	-20	20	Roll rate range at final time of the recovery.
Final pitch rate	Pitch rate	Tf	-10	10	Pitch rate range at final time of the recovery.
Final yaw rate	Yaw rate	Tf	-15	15	Yaw rate range at final time of the recovery.
Final AoA	AoA	Tf	2 deg	6 deg	AoA range at the final time of the recovery.
Final sidslip	Sideslip	Tf	-4 deg	4 deg	Sideslip range at the final time of the recovery.

Table 7.4: State requirements for successful recovery. [5] (Analysis of control strategies for aircraft flight upset recovery)

A recovery is considered to be successful if the state variables all remain within their admissible ranges for the duration of the simulation run, and if the angle of attack, sideslip angle, and angular rates are in their admissible final ranges (goal region) at the end of the simulation. Otherwise, the recovery is considered unsuccessful. This allows for the generation of a binomial distribution of the recoveries.

7.1.4 Number of Monte Carlo Simulations

As explained in the previous section the results of each simulation run is checked to determine if the aircraft recovery was performed successfully or not according to the set requirements in Table 7.4. To determine the number of Monte Carlo simulations necessary to test the recovery system the rule of three from the field of statistics was used. It states that if an event such as an unsuccessful recovery does not occur within a sample of n trails then it can be said with 95% confidence that the probability of the outcome occurring is approximately $\frac{3}{n}$ or less. For example if a batch of 1000 flight recovery tests were run and all of them were successful then it can be said with 95% confidence that the probability of the aircraft not recovering to be $\frac{3}{1000}$ or 0.003.

7.1.5 Deep Stall Simulation Example

For deep stall recovery simulations, the aircraft is initialised in trimmed wings-level flight using the randomly selected initial states and aircraft model parameters. At $t = 1s$ a negative elevator deflection of $-30°$ is applied for one second to force the aircraft into a stall. The aircraft is expected to enter into a deep stall and settle at the deep stall AoA of about 29°.

At $t = 10s$ a snapshot of the aircraft's states is taken, it is tested if the aircraft has entered a deep stall and if true, the states are passed to the deep stall recovery algorithm. The algorithm computes the recovery sequence and then the recovery trajectory regulator applies the recovery sequence to the aircraft. The time series of all the aircraft states are recorded for later analysis.

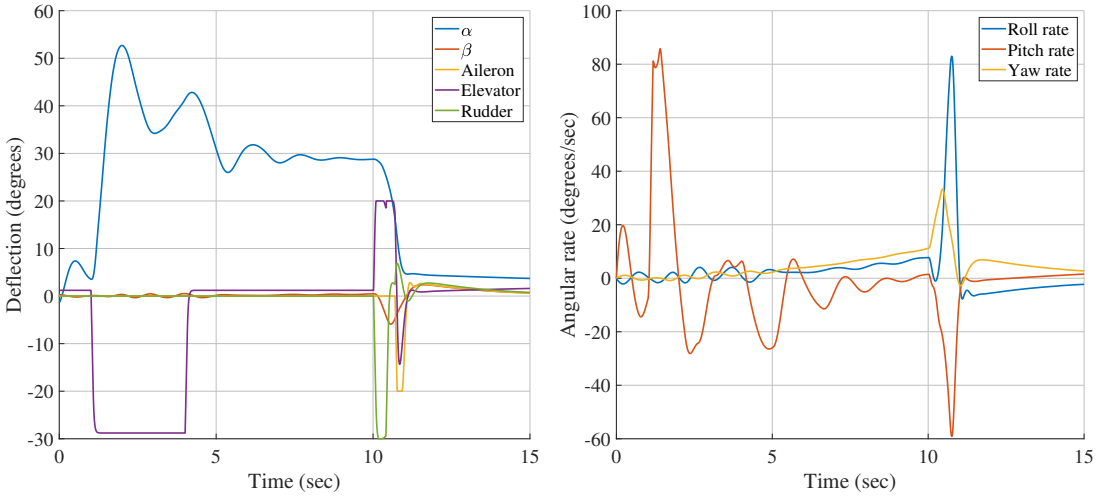

(a) (b)

Figure 7.1: Deep stall recovery simulation example

7.1.6 Spin Simulation Example

For the spin recovery simulations, the aircraft is initialised in trimmed wings-level flight using the randomly selected initial states and aircraft model parameters. At $t = 4s$ a negative elevator deflection of $-10°$ is applied for four seconds to force the aircraft into a stall. The aircraft is expected to enter into a spin and settle at the spin AoA of between 20° and 25°.

At $t = 20s$ a snapshot of the aircraft's states is taken and it is tested if the aircraft has

entered a spin. If true, the states are passed to the spin recovery algorithm. The algorithm computes the recovery sequence and then the recovery trajectory regulator applies the recovery sequence to the aircraft. The time series of all the aircraft states are recorded for later analysis.

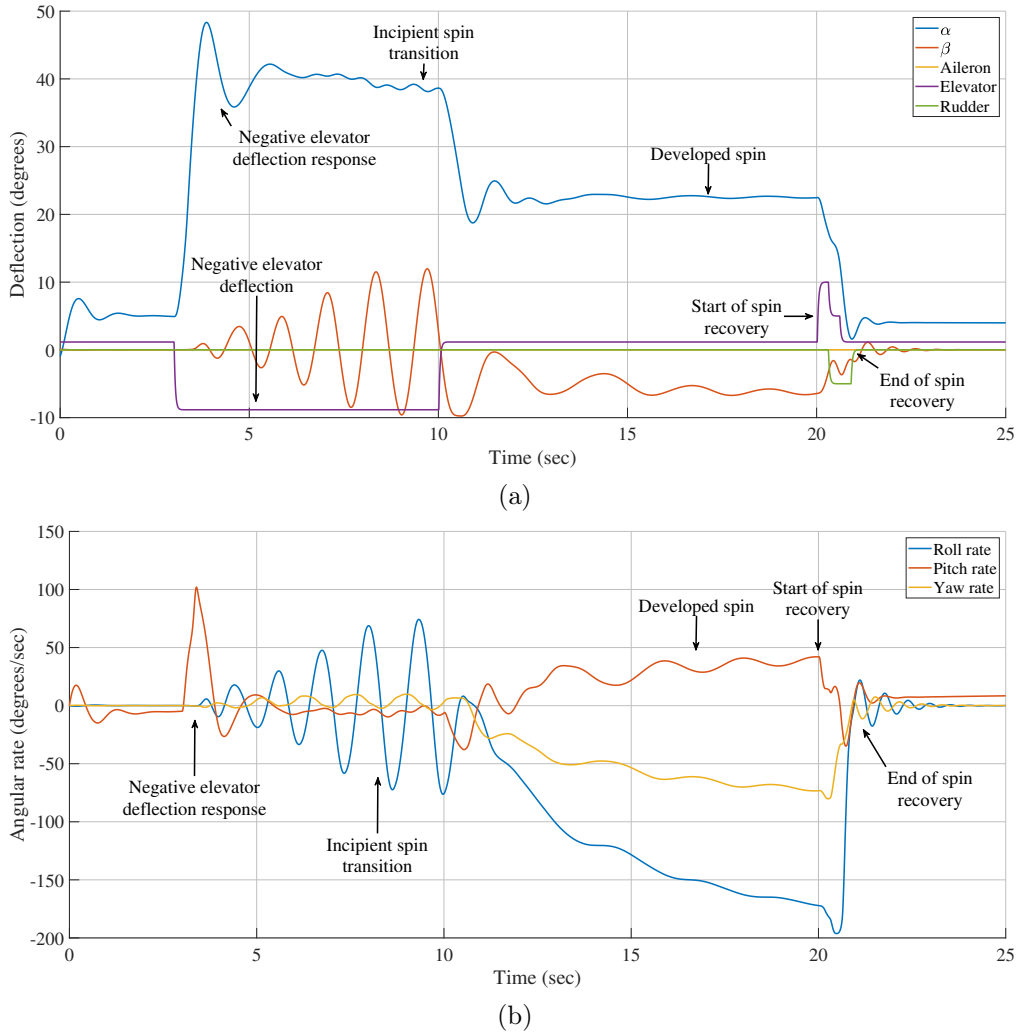

Figure 7.2: Spin recovery simulation example

7.1.7 Trajectory Regulator Testing

To test the different trajectory regulator configurations as described in Section 6 the simulation instance is run for four iterations. In the first iteration, the recovery sequence is applied in open-loop form. The second iteration, the recovery sequence is applied through the LQR. In the third iteration, the recovery sequence is applied in open-loop form with control transfer to the normal flight control once the switching criteria is met. In the last iteration, the recovery sequence is applied through the LQR and with control transfer to normal flight control once the switching criteria is met.

7.1.8 Output Processing

The recorded data from the Monte Carlo batch simulations are processed and through the use of the requirements as described in Table 7.4 it is determined if each simulation

instances resulted in a successful or unsuccessful recovery. These results are presented in the following section.

7.2 Deep Stall Recovery Results

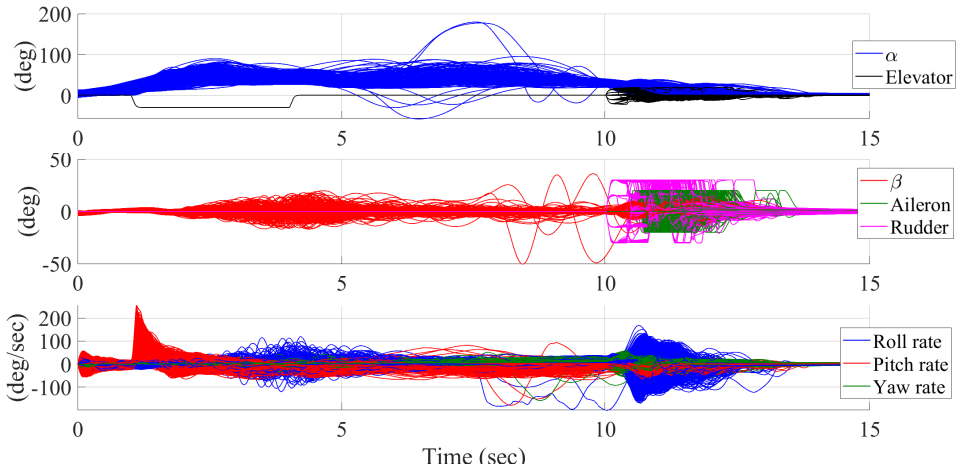

Figure 7.3: Batch deep stall recoveries

From the recorded 2000 deep stall simulation instances, 1739 instances entered a deep stall state. For each of these valid deep stall tests the trajectory planning algorithm was run and determined the optimal recovery sequence and trajectory. The recovery sequence was then performed on the simulation instance using different control approaches; open-loop, open-loop with control transfer, linear quadratic control, and linear quadratic control with control transfer.

Test	**Recoveries**	**Nodes explored**	**Recovery duration**	**Altitude loss**
Open-loop	19.84%	20	3.29 sec	193 ft
Open-loop with switch	97.01%	20	1.26 sec	188 ft
LQR	79.93%	20	2.59 sec	190 ft
LQR with switch	99.94%	20	1.27 sec	188 ft

Table 7.5: Deep Stall recovery results

From the table above it is evident that transferring the control to the normal flight control once the aircraft enters the linear flight region improves the recovery rate from 19.84% to up to 97.01%. The LQR also improves on the results of the open-loop test by increasing the recovery rate to 79.93%. The combination of the linear quadratic control with the control transfer to the normal flight control results in 99.94% recovery rate and therefore, is the best approach for applying the deep stall recovery sequence which was calculated by the trajectory planning algorithm.

On average the successful recoveries performed by the different control approaches all yielded an altitude loss of about $189ft$ with the best altitude loss of $99ft$ and the worst altitude loss of $349ft$ which is well within the $1500ft$ admissible altitude loss as specified in Table 7.4.

For the control approach using the LQR and the control transfer, an average of 20 nodes were explored to find the recovery sequence. In the following section the most commonly used recovery sequences generated by the trajectory planning algorithm are analysed and thereby, determined if a general recovery sequence can be identified and used as the standard recovery sequence coupled with the control approach of the LQR and control transfer to normal flight control.

7.2.1 Deep Stall Recovery Sequence Analysis

For deep stall the trajectory planning algorithm had the following action space to choose recovery control inputs from:

$$\begin{aligned} \delta_A(k) &\in \{0\} \\ \delta_E(k) &\in \{-30, -20, -10, 0, +8, +15, +20\} \\ \delta_R(k) &\in \{-30, -15, 0, +15, +30\} \end{aligned}$$

Therefore for each time step the algorithm has the choice of seven different elevator control actions and five different rudder control actions resulting in 35 different control input combinations. In the previous section it was observed that the average recovery duration is about $1.28s$ which is just more than three control time steps. One control time step is set to $0.4s$ for the deep stall trajectory planner and therefore the first three input control actions in a recovery sequence is of interest. The different recovery sequences were therefore identified according to the first three input control actions. The occurrences of each recovery sequence within the 1739 simulation instances was recorded. In Table 7.6 the top five most common recovery sequences are presented.

	Top five sequences				
Occurrence:	9.66%	9.60%	6.09%	4.66%	4.08%
Time step	**Elevator Actions**				
1	15.00	15.00	15.00	15.00	15.00
2	20.00	20.00	15.00	20.00	20.00
3	15.00	20.00	1.21	20.00	15.00
	Rudder Actions				
1	-30.00	-30.00	30.00	-30.00	30.00
2	0.01	0.01	15.00	0.01	0.01
3	30.00	30.00	-15.00	15.00	0.01

Table 7.6: Top five elevator and rudder control sequences for deep stall recoveries

These top five deep stall recovery control sequences represent just over 30% of all the recovery sequences. Therefore one could assume that each recovery sequence is fairly unique and that there is no general recovery sequence for deep stall. For the elevator actions they are all positive deflections and all start off with a 15 degree deflection followed by mostly a 20 degree deflection and finally with a either a reduction in the elevator deflection or keeping it constant from the second time step. As for the rudder deflection the recovery for deep stall starts with either maximum positive or maximum negative rudder deflection

and this is followed in the second time step by a reduction in the deflection mostly to trim rudder deflection of 0.01°. In the third time step the rudder is deflected in the opposite direction to which it was deflected in the first time step and with a magnitude of 30° or 15°. From this analysis it can be concluded that there is a general pattern to deep stall recovery. In the following section it is tested how effective it is to only use the most common recovery sequence in recovering the aircraft from deep stall.

7.2.2 General Deep Stall Recovery

The Monte Carlo simulations were repeated, but this time using the general recovery sequence that was identified in the previous section, instead of performing the trajectory planning online. These Monte Carlo simulations were performed to determine whether the standard recovery sequence that was calculated offline could achieve a similar success rate as the recovery sequences that are calculated online. Figure 7.4 shows the time series of the most commonly found recovery sequence from the previous section.

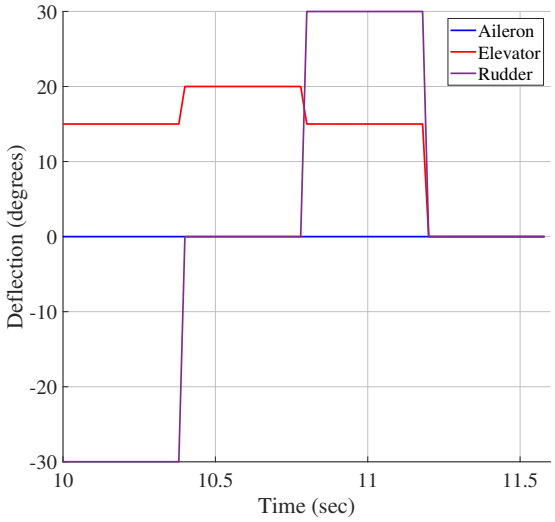

Figure 7.4: General deep stall recovery sequence.

For each simulation instance the appropriate LQR gains are calculated as these are directly dependent on the states of the aircraft most notably airspeed. 2000 simulation instance were run and the following results were recorded.

Test	Recoveries	Nodes explored	Recovery duration	Altitude loss
Open-loop	20.50%	NA	3.33 sec	168 ft
Open-loop with switch	82.80%	NA	1.19 sec	197 ft
LQR	37.59%	NA	2.18 sec	171 ft
LQR with switch	91.91%	NA	1.15 sec	199 ft

Table 7.7: Deep Stall recovery results using the most common recovery sequence.

From the 2000 Monte Carlo instances 1739 of them entered a deep stall state. The general deep stall recovery sequence improved the open-loop results to a recovery rate of 30.53% but decreased the open-loop with control transfer results to 93.96% and decreased the LQR results to 59.98%. Using the control approach of LQR and control transfer yielded a

recovery rate of 99.6% and the time required to calculate the LQR gains averaged at $1.02s$. The altitude loss increased from $188ft$ to $195ft$ which is still well within the $1500ft$ limit. Recovery duration also increased from $1.28s$ to $1.48s$.

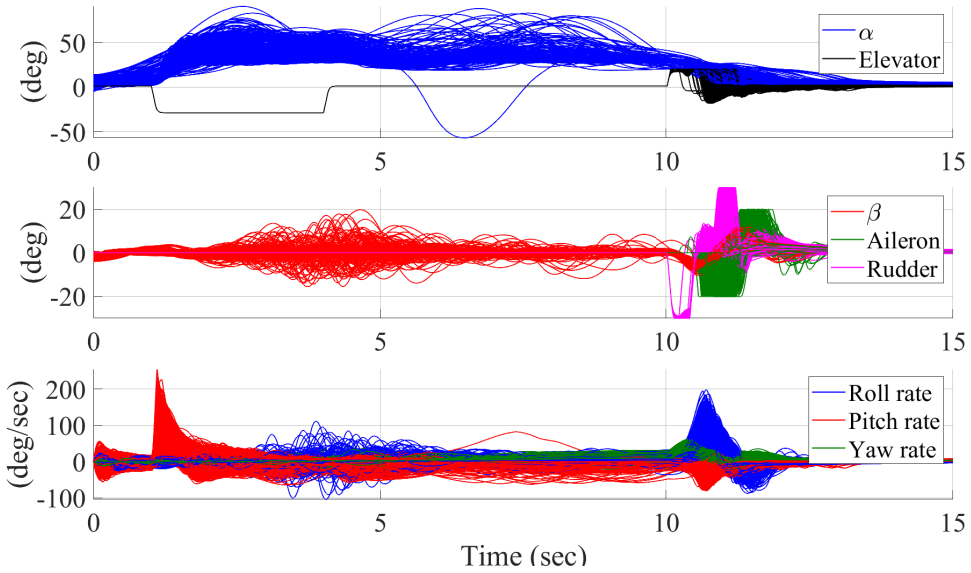

Figure 7.5: Deep stall recovery trajectories using the general recovery sequence.

Overall these results are very satisfying as they confirm the proposed deep stall recovery method as explained by Engelbrecht [9]. In his thesis he explains that by applying a rudder action to generate either a positive or negative sideslip deflection and then by applying positive elevator action to generate a negative pitching moment should be a valid deep stall recovery sequence.

This concludes the deep stall recovery results. By combining LQR control with the switching function to transfer control authority to the normal flight control once the aircraft enters the linear flight region proved to be the most effective control approach. Through further analysis a general deep stall recovery strategy has been identified and was tested using the Monte Carlo method. The general deep stall recovery strategy proved to be very effective and validates the proposed deep stall recovery strategy proposed by Engelbrecht in his thesis.

7.3 Spin Recovery Results

From the recorded 2000 spin simulation instances only 1444 instances entered a self-sustained spin. The high angular rates experienced during a spin cause the spin to be very unstable. This results in most aircraft recovering naturally from a spin state. But for the instances when the aircraft entered a stable spin the trajectory planning algorithm was used to determine the optimal recovery sequence and trajectory. As described in the previous section the recovery sequence using four different control approaches namely, open-loop, open-loop with control transfer to normal flight control, LQR, and LQR with control transfer to normal flight control, are applied.

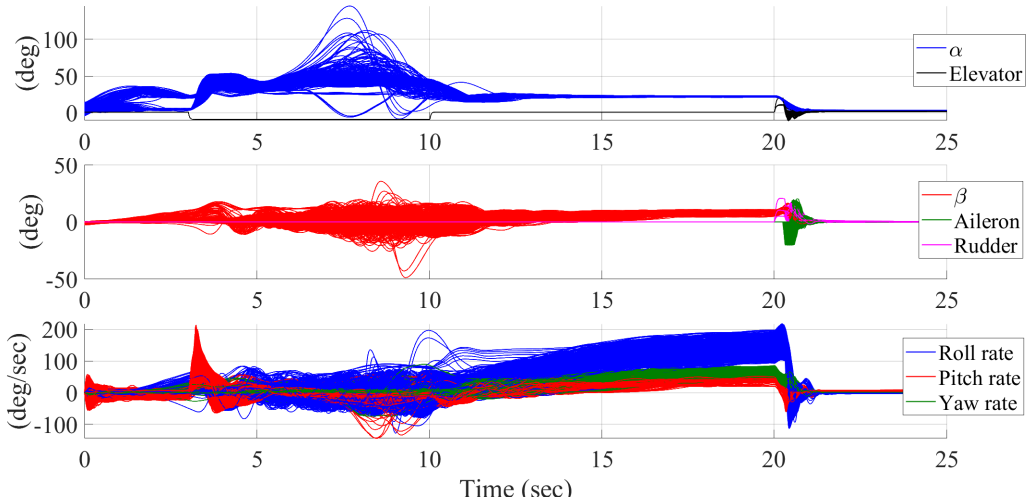

(a) Right spin recoveries

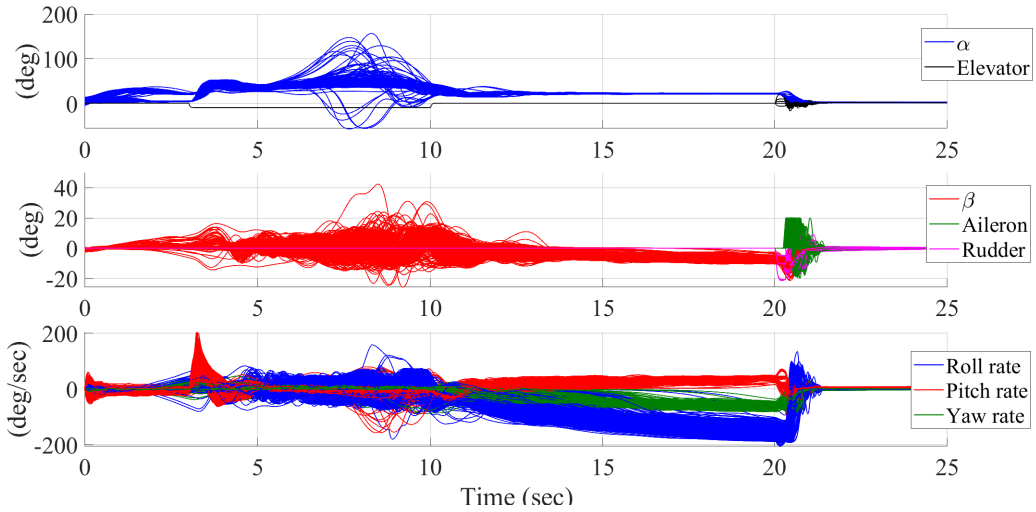

(b) Left spin recoveries

From the results in Table 7.8 it can be noted that the open-loop recovery control approach is already effective with 91.34% successful recovery rate. By switching over to normal flight control as the aircraft enters the normal flight envelope a recovery rate of 99.17% is observed which is a 7.83% improvement in the recovery rate. With just LQR control a recovery rate of 91.27% is observed and by combining LQR with control transfer to normal flight control a successful recovery rate of 99.31% is noted.

Test	**Recoveries**	**Nodes searched**	**Recovery duration**	**Altitude loss**
Open-loop	91.34%	28	1.67 sec	392 ft
Open-loop with switch	99.17%	28	0.68 sec	390 ft
LQR	91.27%	28	1.07 sec	403 ft
LQR with switch	99.31%	28	0.65 sec	390 ft

Table 7.8: Spin recovery results

An average of 28 nodes were explored to find a valid spin recovery sequence. The recovery duration is longest for the open-loop approach which has an average recovery duration of

1.67s. LQR control reduces the recovery duration average to 1.07s and by using transferring control to normal flight control once the aircraft enters normal flight envelope, the spin recovery duration is reduced to 0.65s. All spin recovery control approaches have an average altitude loss of about 393ft which is double that of the 188ft which was used to recover the aircraft from deep stall. In a spin the aircraft tightly spirals downwards and presents a smaller surface area to the oncoming airflow. In a deeps stall the whole wing area as well as the fuselage are presented towards the oncoming airflow causing more drag and thereby slowing the aircraft down. The lowest altitude loss for a spin recovery recorded was 241ft and the largest altitude loss for a spin recovery was 544ft which is within the 1500ft limit. In the next section the spin recovery sequences which were identified by the trajectory planning algorithm are analysed and it will be determined if a general recovery sequence can be identified.

7.3.1 Spin Recovery Sequence Analysis

For spin, the trajectory planning algorithms had the following action space to choose recovery control inputs from:

$$\begin{aligned} \delta_A(k) &\in \{0\} \\ \delta_E(k) &\in \{-30, -20, -10, -5, 0, +5, +10, +20\} \\ \delta_R(k) &\in \{-30, -20, -10, -5, 0, +5, +10, +20, +30\} \end{aligned}$$

The trajectory planning algorithms have eight different elevator control actions and nine different rudder control actions resulting in 72 different possible control input combinations. For spin, the trajectory planner used a time step size of 0.3s. With an average spin recovery duration time of 0.65s when using the control approach of LQR and control transfer, it was determined, with rounding up, that the first three control actions within the recovery sequence are of significance.

In the following two tables the five most commonly used recovery sequences were identified according to the first three control actions for left spins and right spins. It is important to distinguish between the two different spin directions as the control actions should be different for each. 2000 Monte Carlo simulation instances were run and 1444 of these instances developed into a stable spin of which 596 of them were left spins and 838 of them were right spins.

	Top five recovery sequences				
Occurrence:	29.87%	29.02%	11.91%	5.20%	5.03%
Time step (k)	**Rudder Actions**				
1	-10.0	-10.0	-5.0	-10.0	-5.0
2	-10.0	-5.0	-5.0	-5.0	-10.0
3	0.01	0.01	0.01	0.01	0.01
	Elevator Actions				
1	10.00	10.00	10.00	20.00	10.00
2	1.16	1.16	1.16	-5.00	1.16
3	1.16	1.16	1.16	1.16	1.16

Table 7.9: Top five elevator and rudder control sequences for left spin recoveries

For left spins, the top five recoveries sequences account for 58.89% of the recoveries. For the first time step, most of the rudder actions are set to $\delta_R = -10.00°$ and the elevators are deflected to $\delta_E = 10.00°$. In the second time step, there is some variation but most recovery sequences use a negative rudder deflection of up to $-5.00°$ and reduce the elevator deflection to trim setting. Finally, for the third time step, all recovery sequences set the rudder deflection and the elevator deflection to trim setting.

	Top five recovery sequences				
Occurrence:	50.23%	23.74%	15.15%	2.30%	2.14%
Time step (k)	**Rudder Actions**				
1	10.00	10.00	5.00	10.00	10.00
2	5.00	10.00	5.00	5.00	5.00
3	0.01	0.01	0.01	0.01	0.01
	Elevator Actions				
1	10.00	10.00	10.00	20.00	10.00
2	1.16	1.16	1.16	-5	-5
3	1.16	1.16	1.16	1.16	1.16

Table 7.10: Top five elevator and rudder control sequences for right spin recoveries

For right spins, the top five recoveries sequences account for 93.56% of the recoveries. For the first time step, most rudder actions are set to $\delta_R = 10.00°$ to generate a negative yawing moment and the elevator is deflected to $\delta_E = 10.00°$ which is identical to the left spin recoveries. For the second time step, most recovery sequences use a rudder deflection of $\delta_R = 5.00°$ and reduce the elevator deflection to its trim setting. Finally, for the third time step, all recovery sequences reduce the rudder deflection and the elevator deflection to their trim setting.

For both left spin and right spin the following recovery strategies were noted: For both left spins and right spins a positive elevator deflection of $\delta_E = 10.00°$ is applied to generate a negative pitching moment to reduce the high AoA experienced during a spin. For left spins a negative rudder deflection is applied to generate a positive yawing moment to reduce the high negative yaw and roll rates. For right spins a positive rudder deflection is applied to generate a negative yawing moment to reduce the high positive yaw and roll rates. This is in line with the spin recovery strategy as described by Federal Aviation Authority[1]. In the next section general left spin and right spin recovery sequences will be tested using the Monte Carlo method.

7.3.2 General Spin Recovery

For each simulation instance it is first determined if the aircraft has entered a left or a right spin and then the appropriate recovery sequence is applied. For each recovery the LQR gains were calculated as these are directly dependent on the states of the aircraft, most notably airspeed and angular rate. From the findings of the previous section the following general left and right spin recovery sequences were identified,

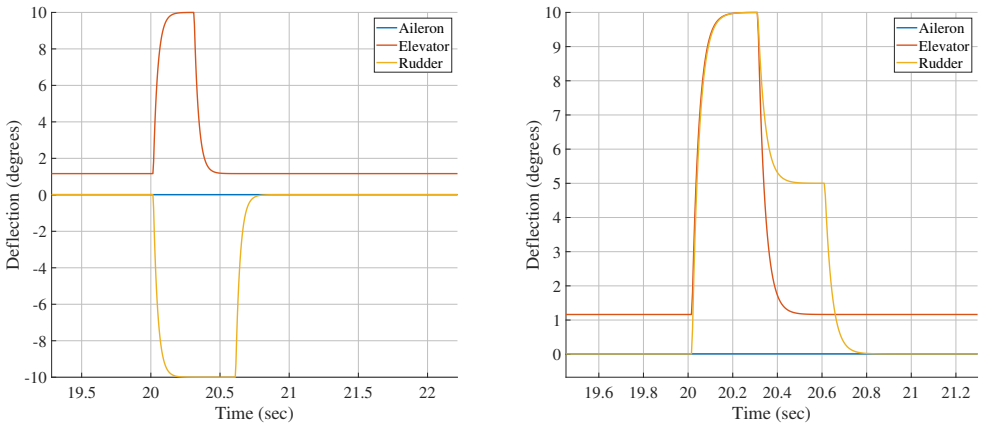

(a) Left spin (b) Right spin

Figure 7.7: Spin recovery control sequences.

2000 simulation instance were run and the following results were recorded. The recovery trajectories of the simulation batch are shown in Figures 7.8 and 7.9. From the 2000 Monte Carlo instances, 608 of them entered a stable left spin state, and 840 of them entered a stable right spin state.

Test	**Recoveries**	**Nodes explored**	**Recovery duration**	**Altitude loss**
Open-loop	93.14%	NA	1.68 sec	394 ft
Open-loop with switch	100.00%	NA	0.68 sec	392 ft
LQR	93.14%	NA	1.49 sec	405 ft
LQR with switch	100.00%	NA	0.66 sec	393 ft

Table 7.11: Spin recovery results using the general left and right spin recovery sequences.

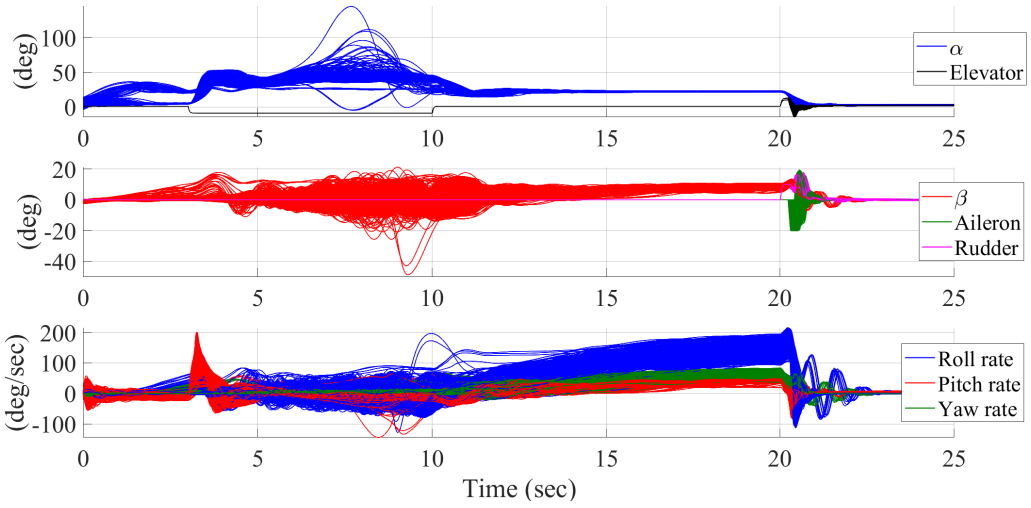

Figure 7.8: Right spin recovery trajectories using the general recovery sequence.

By applying the general spin recovery sequences the open-loop recovery rate increased from 91.34% to 93.14%, but by combining open-loop with the control transfer to normal flight

control the recovery rate was improved from 99.17% to 100.00%. The control approach of just LQR control had a increased recovery rate of 93.14% up from 91.27% when just using the general spin recovery sequence. The combined control approach of LQR with the control transfer to normal flight control resulted in a recovery rate of 100.00%. The recovery duration also improved on average from $0.68s$ down to $0.66s$ and the average altitude lost increased from $341ft$ to $393ft$ which is still well within the $1500ft$ acceptable limit.

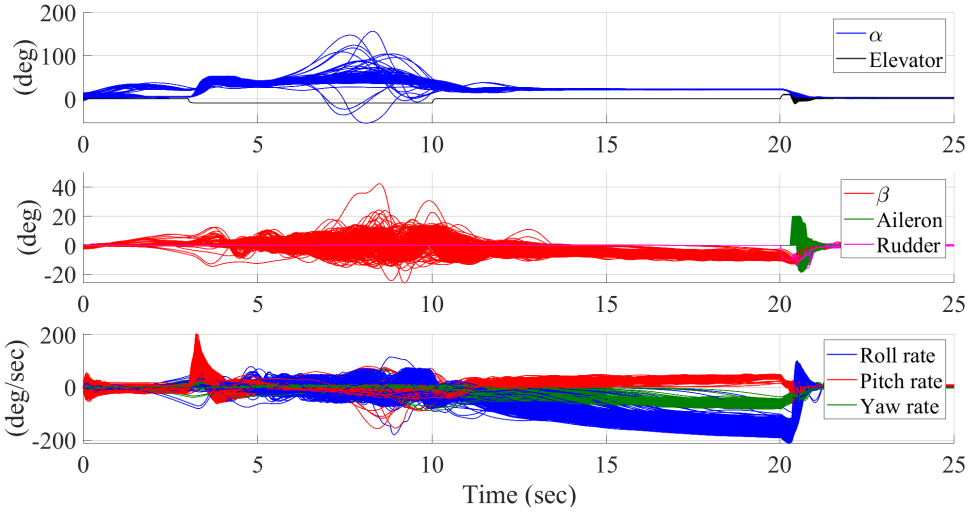

Figure 7.9: Left spin recovery trajectories using the general recovery sequence.

These results confirm that the method of setting ailerons to neutral, applying opposite rudder to spin rotation until rotation stops, and applying a positive elevator deflection to reduce the AoA as described by the Federal Aviation Authorities flight handbook [1] is a valid spin recovery strategy. The use of LQR control to regulate the recovery manoeuvre and transferring control of the aircraft to the normal flight controller once the aircraft enters the normal flight envelope proved to be most effective. Analysis of the recovery sequences identified by the trajectory planning algorithm resulted in a general spin recovery strategy which matches the advised spin recovery procedures as prescribed by the Federal Aviation Authorities.

7.4 Conclusion

This concludes the verification and testing chapter. The Monte Carlo method was introduced and its application explained as well as which states were varied and to what degree. The brief description of the modelled external disturbance is given and it was explained as to why the recovery control system was given a different aircraft model instance to that which was being currently simulated. A table of the state requirements for a successful recovery was given and a brief discussion on the required quantity of Monte Carlo simulations was stated. Deep stall and spin simulation instances were shown and discussed and it was explained why different configurations of the recovery control system was tested. The deep stall recovery results were presented and analysed. A general deep stall recovery sequence was identified and tested and the results were also presented and analysed. This was followed by the spin recovery results which were presented and analysed. For spin recovery a general left spin and a general right spin recovery strategies were identified and also tested. The results of the tests were presented and discussed.

Chapter 8

Conclusion

8.1 Summary of Work

The thesis presented a deep stall and spin recovery system which is based on optimal trajectory planning algorithms. A nonlinear aircraft model was modified to exhibit the dynamics of deep stall and spin and was verified in simulation.Deep stall recovery and spin recovery were both formulated as optimal control problems. The deep stall recovery problem was solved using a modified $A*$ algorithm operating on a three-degrees-of-freedom (3DOF) wide-envelope model if the aircraft dynamics. The spin recovery problem was solved using both a modified $A*$ and an RRT algorithm operating on a six-degrees-of-freedom (6DOF) wide-envelope model of the aircraft dynamics. The deep stall recovery and spin recovery trajectory planners were both verified in simulation.

To improve the robustness of the recovery system to model uncertainty and external disturbances, a closed-loop trajectory regulator was added to control the aircraft to follow the planned recovery trajectory. Linear quadratic control was implemented as the trajectory regulator for both deep stall and spin recoveries. A switching function was also added to transfer control of the aircraft back to the normal flight control system once the aircraft has been returned to its normal flight envelope by the recovery system. The final deep stall and spin recovery system consists of the trajectory planner, the trajectory regulator, and the switching function. Monte Carlo simulations were performed to test the ability of the stall and spin recovery system to recover the aircraft from random upset conditions, and to verify the robustness of the system to model uncertainty and external disturbances.

Simulation results show that the deep stall and spin recovery systems have satisfactory performance across the whole domain of initial aircraft states and aircraft model parameters. Both the $A*$ and RRT search algorithms performed well as a good balance between speed and accuracy was found. This allowed the search algorithms to navigate the very large state-space of an aircraft efficiently and resulted in timely deep stall and spin recovery trajectories and input sequences. The trajectory planner consistently generated successful recovery trajectories and input control sequences.

The LQR trajectory regulator performed as expected and ensured that in the presence of disturbances the deep stall and spin recoveries followed the planned recovery state trajectories closely. The LQR is dependent on the linearised state-space model of the aircraft and it was found that the method used to calculated the state-space model was not as accurate due to the use of the 3DoF model in the calculation. It is proposed that the 6DoF model be used with a different method of generating the state-space model of the aircraft for the LQR.

The control switching function which transferred control from the recovery system to the existing flight control once the aircraft has returned to the normal flight envelope worked as expected. It was noted that once the aircraft has been returned to its normal flight envelope, the normal flight control laws (that were designed for the normal flight envelope) will be able to control the aircraft again, and can then take over and perform rest of the recovery. This encouraged the idea of using linear control for inside the normal flight envelope and non-linear control for outside the normal flight envelope. The control switching function allowed control of the aircraft to be transferred from the deep stall and spin recovery system to the existing flight control system.

The Monte Carlo method which was used to test the deep stall and spin recovery systems over the extensive state-space of the GTM performed very well. The Monte Carlo method enabled the testing of the boundary cases extensively which would have been very difficult to do using actual tests with a radio controlled aircraft or an actual aircraft due to the risks involved. The modelling of a range of external disturbances generated a good representation of the actual flight disturbances. Testing in simulation also made it effortless to change the physical characteristics of the aircraft, such as mass, allowing for a large range of different flight states of the aircraft to be tested.

The analysis of the recovery input control sequences that were generated by the trajectory planning algorithms resulted in the identification of general deep stall and spin recovery strategies which match the advised deep stall and spin recovery procedures as prescribed by the Federal Aviation Authorities. This is a satisfactory result as it confirms that the proposed deep stall and spin recovery trajectory planner works as required.

8.2 Recommendations for Future Work

The following recommendations were identified and would bring this research one step closer to actual implementation into actual aircraft.

- Implement the trajectory planning and regulator algorithms on different aerodynamic models such as SUPRA and ADMIRE. This will test the general applicability of the algorithms as well as bring to light shortcomings.
- Implement the deep stall and spin recovery sequences in hardware and perform hardware in the loop validation test. This will test the recovery systems capability to work in real time which is necessary for implementation into an actual aircraft.
- Refine the deep stall and spin recovery sequences by using smaller elevator and rudder discretisation. This will increase the calculation time but may result in the identification of other deep stall and spin recovery strategies such as pitch rocking.
- Implement a more sophisticated normal flight controller to perform flight control in the normal flight envelope. As the recovery control system is designed to be a separate control system from the normal flight control of the aircraft it is important to ensure that the transition of control authority is seamless once the deep stall or spin recovery has been performed and the aircraft has returned to the normal flight envelope.

Bibliography

[1] Federal Aviation Administration. *Airplane Flying Handbook FAA-H-8083-3A*. U.S. Department of Transportation, Federal Aviation Administration, 2004.

[2] Airbus, ATR, Boeing, Bombardier, Embraer and ICAO. *AUPRTA Rev 3.0*. Tech. rep. ICAO, 2018. URL: https://www.icao.int/safety/loci/auprta/index.html.

[3] Roberto Bunge and Ilan Kroo. "Automatic Spin Recovery with Minimal Altitude Loss". In: *2018 AIAA Guidance, Navigation, and Control Conference*. American Institute of Aeronautics and Astronautics, 2018.

[4] J.R. Chambers and S.B. Grafton. *Aerodynamic Characteristics of Airplanes at High Angles of Attack*. Tech. rep. NASA TM-74097. NASA, 1977.

[5] Luis Crespo et al. "Analysis of Control Strategies for Aircraft Flight Upset Recovery". In: (2012), pp. 1–31. DOI: 10.2514/6.2012-5026.

[6] Kevin Cunningham et al. "Practical Application of a Subscale Transport Aircraft for Flight Research in Control Upset and Failure Conditions". In: *Guidance, Navigation, and Control and Co-located Conferences*. American Institute of Aeronautics and Astronautics, Aug. 2008.

[7] Department Defence. *MIL-F-8785C*. Department of Defence, Nov. 1980. URL: http://everyspec.com/MIL-SPECS/MIL-SPECS-MIL-F/MIL-F-8785C_5295/.

[8] J A A Engelbrecht and I K Peddle. *Advance Automation 833 Introductory course to aircraft dynamics*. University of Stellenbosch, Jan. 2017.

[9] Jacobus Adriaan Albertus Engelbrecht. "Automatic flight envelope recovery for large transport aircraft". PhD thesis. Stellenbosch: Stellenbosch University, 2016.

[10] Federal Aviation Administration. *Maintaining Aircraft Control: Upset Prevention and Recovery Training*. Tech. rep. Federal Aviation Administration, 2017.

[11] Lars Forssell and Ulrik Nilsson. *ADMIRE The Aero-Data Model In a Research Environment Version 4.0, Model Description Systems Technology User report*. 2005.

[12] John Foster et al. "Dynamics Modeling and Simulation of Large Transport Airplanes in Upset Conditions". In: *Guidance, Navigation, and Control and Co-located Conferences*. American Institute of Aeronautics and Astronautics, Aug. 2005, p. m.

[13] Gonzalo Garcia, Shawn Keshmiri, and Weizhang Huang. "Recovery of an Aircraft from the Loss of Control Using Open Final Time Dynamic Optimization and Receding Horizon Control". In: *AIAA Guidance, Navigation, and Control Conference 2015* (2015), pp. 160–224.

[14] M. Goman et al. "Aircraft Spin Prevention/Recovery Control System". In: *Third Russian–Chinese Scientific Conference on Aerodynamics and Flight Dynamics of Aircraft* 3rd (1993).

[15] Richard M Hueschen. *Development of the Transport Class Model (TCM) Aircraft Simulation From a Sub-Scale Generic Transport Model (GTM) Simulation*. Tech. rep. NASA, 2011.

[16] Thomas Jordan et al. *Development of a Dynamically Scaled Generic Transport Model Testbed for Flight Research Experiments*. 2005. URL: www.larc.nasa.gov.

[17] A. Khrabrov, M. Sidoryuk, and M. Goman. "Aerodynamic model development and simulation of airliner spin for upset recovery". In: EDP Sciences, June 2013, pp. 621–636. DOI: 10.1051/eucass/201305621.

[18] Steven M. LaValle. *Planning Algorithms*. Cambridge University Press, 2006.

[19] Dong-Chan Lee and M. G. Nagati. "Momentum Vector Control for Spin Recovery". In: *Journal of Aircraft* 41.6 (Nov. 2004), pp. 1414–1423.

[20] Moshe Medina and Manuel Shahaf. "Post stall characteristics of highly augmented fighter aircraft". In: *ICAS, Congress, 17 th, Stockholm, Sweden*. 1990, pp. 1976–1983.

[21] Austin Matthew Murch. "Aerodynamic modeling of post-stall and spin dynamics of large transport airplanes". PhD thesis. Georgia Institute of Technology, 2007.

[22] Austin Murch and John Foster. "Recent NASA Research on Aerodynamic Modeling of Post-Stall and Spin Dynamics of Large Transport Airplanes". In: *Aerospace Sciences Meetings*. American Institute of Aeronautics and Astronautics, Jan. 2007.

[23] Patrick Murphy and Vladislav Klein. "Transport Aircraft System Identification from Wind Tunnel Data". In: *Guidance, Navigation, and Control and Co-located Conferences*. American Institute of Aeronautics and Astronautics, Aug. 2008.

[24] Aditya A Paranjape et al. "Analytical Assessment of the Spin Susceptibility of the NASA Generic Transport Model". In: DOI: 10.2514/6.2013-5081.

[25] Iain K Peddle. *Acceleration Based Manoeuvre Flight Control System for Unmanned Aerial Vehicles*. Stellenbosch University, 2008.

[26] Pawit Pharpatara. "Trajectory planning for aerial vehicles with constraints. (Planification de trajectoire sous contraintes d'aéronef)". PhD thesis. University of Paris-Saclay, France, 2015. URL: https://tel.archives-ouvertes.fr/tel-01206423.

[27] PK Raghavendra et al. "Aircraft Spin Recovery, with and without Thrust Vectoring, Using Nonlinear Dynamic Inversion". In: *Journal of Aircraft* 42.6 (Nov. 2005), pp. 1492–1503.

[28] Nandan Kumar Sinha and D. M. K. K. Venkateswara Rao. "Aircraft Spin Recovery Using a Sliding-Mode Controller". In: *Journal of Guidance, Control, and Dynamics* 33.5 (Sept. 2010), pp. 1675–1679.

[29] Pei Wang and Zhongke Shi. "Study of deep-stall characteristics and longitudinal special phenomena of T-tail aircraft". In: *2010 IEEE International Conference on Mechatronics and Automation, ICMA 2010*. 2010, pp. 59–64. ISBN: 9781424451418. DOI: 10.1109/ICMA.2010.5588718.

[30] Pei Wang and Zhongke Shi. "Study of deep-stall characteristics and longitudinal special phenomena of T-tail aircraft". In: *2010 IEEE International Conference on Mechatronics and Automation, ICMA 2010* (2010), pp. 59–64.

[31] Anil Yildiz et al. "Finite State Automata Based Approach to Autonomous Stall and Upset Recovery for Agile Aircraft". In: *2018 AIAA Guidance, Navigation, and Control Conference*. American Institute of Aeronautics and Astronautics, 2018.